

**Intermolecular zero-quantum coherence detection
for *in vivo* MR spectroscopy**

Dissertation zur Erlangung
des naturwissenschaftlichen Doktorgrades
der Bayerischen Julius-Maximilians-Universität
Würzburg

vorgelegt von

Dávid Zsolt Balla

aus Oradea

Würzburg, 2009

Eingereicht am: 22. Januar 2009

bei der Fakultät für Physik und Astronomie

1. Gutachter: Prof. Dr. Peter Jakob
2. Gutachter: Prof. Dr. Cornelius Faber
3. Gutachter:

1. Prüfer: Prof. Dr. Peter Jakob
2. Prüfer: Prof. Dr. Cornelius Faber
3. Prüfer: Prof. Dr. Georg Reents

im Promotionskolloquium

Tag des Promotionskolloquiums: 28. August 2009

Doktorurkunde ausgehändigt am:

TABLE OF CONTENTS

INTERMOLECULAR ZERO-QUANTUM COHERENCE DETECTION FOR <i>IN VIVO</i> MR SPECTROSCOPY	1
1. INTRODUCTION	6
2. BASIC PRINCIPLES OF NMR	8
2.1 THE ZEEMAN INTERACTION	9
2.2 INTERACTION WITH AN OSCILLATING RF-FIELD	9
2.3 INTERNAL SPIN INTERACTIONS.....	10
2.3.1 <i>Chemical shift</i>	10
2.3.2 <i>Direct dipolar interaction</i>	11
2.4 SPIN DENSITY OPERATOR	11
2.4.1 <i>Product operator formalism</i>	12
2.4.2 <i>Magnetization</i>	13
2.4.3 <i>The Liouville – von Neumann equation</i>	15
2.5 MAGNETIZATION DYNAMICS	15
3. INTERMOLECULAR MULTIPLE-QUANTUM COHERENCE NMR SPECTROSCOPY	17
3.1 THE QUANTUM PICTURE OF IZQC-SIGNAL FORMATION	18
3.1.1 <i>Spectral patterns</i>	21
3.2 THE DISTANT DIPOLAR FIELD (DDF).....	22
3.3 RESOLUTION ENHANCEMENT	24
3.4 SIGNAL EVOLUTION AND SPECTRAL ANALYSIS	25
4. METHOD DEVELOPMENT FOR <i>IN VIVO</i> IZQC-SPECTROSCOPY	29
4.1 SELECTIVE HOMOGENIZED (SEL-HOMOGENIZED).....	29
4.1.1 <i>Theoretical analysis of SEL-HOMOGENIZED</i>	29
4.1.2 <i>Optimal acquisition window for SEL-HOMOGENIZED</i>	32
4.1.3 <i>Experimental evaluation of SEL-HOMOGENIZED</i>	34
4.1.3.1 Materials and methods.....	34
4.1.3.2 Results	34
4.2 WATER SUPPRESSION (WS)	36

4.2.1 Optimization of WS efficiency at a high-resolution 9.4 T NMR spectrometer.....	36
4.2.2 Water suppression at a 17.6 T small animal NMR microimager	39
4.3 SINGLE VOXEL LOCALIZATION	41
4.3.1 Localization within the HOMOGENIZED sequence (S1)	41
4.3.2 Localization of the magnetization prior to a global HOMOGENIZED (S2).....	43
4.3.3 Localization of detectable signal immediately prior to acquisition (S3).....	44
4.3.4 The limits of localization efficiency of S1 and S2.....	45
4.3.4 Experimental comparison of localization techniques in a phantom.....	46
4.3.4.1 Materials and methods	46
4.3.4.2 Results	46
4.3.5 Avoiding the chemical shift displacement artefact with S1 and S2	48
5. IN VIVO APPLICATIONS OF LOCALIZED IZQC MRS.....	50
5.1 EXPERIMENTAL HARDWARE AND ANIMAL PREPARATION.....	50
5.1.1 Materials for in vivo experiments.....	50
5.1.2 Animal handling.....	51
5.2 VALIDATION OF SINGLE-VOXEL IZQC MRS IN THE RODENT BRAIN.....	51
5.2.1 Acquisition parameters and processing	51
5.2.2 Results	53
5.3 FEASIBILITY OF CONVENTIONAL AND IZQC MRS IN THE RAT SPINAL CORD AT 17.6 T	54
5.3.1 Materials and Methods.....	54
5.3.2 Results	56
5.3.2.1 Conventional MRS	56
5.3.2.2 IZQC spectroscopy	58
5.4 IZQC MRS IN TUMORS IN VIVO	59
5.4.1 Experimental details.....	60
5.4.2 Results	61
6. IZQC-MRS IN PRESENCE OF LOCAL DIPOLE FIELDS.....	63
6.1 MAXIMUM LOCAL DIPOLE FIELDS FOR RESOLUTION ENHANCEMENT.....	63
6.1.1 Theory	63
6.1.2 Numerical simulations.....	65
6.1.2.1 Simulation algorithm	65

6.1.2.2 Simulation parameters	66
6.1.2.3 Analysis of the spectra.....	67
6.1.2.4 Validity assessment	70
6.1.2.5 Tolerance of digitization error in simulations.....	72
6.1.2.6 Results: The impact of B_{dip} on linewidths and peak intensities	74
6.1.2 Experiments	77
6.1.3 Simulated vs. experimental spectra.....	78
6.1.4 Discussion.....	80
6.2 RESOLUTION ENHANCEMENT IN PRESENCE OF IRON-OXIDE MICROPARTICLES	82
6.2.1 Acquisition parameters	82
6.2.2 Processing.....	82
6.2.3 Results.....	83
6.2.4 Discussion.....	84
6.3 CONCLUSION	84
7. SUMMARY.....	85
8. ZUSAMMENFASSUNG.....	87
9. REFERENCES	89
APPENDIX A	97
APPENDIX B.....	99
APPENDIX C	101
APPENDIX D	103
CURRICULUM VITAE	106
PERSONAL INFORMATION	106
EDUCATION	106
PUBLICATION RECORD.....	107
SCIENTIFIC ARTICLES	107
CONFERENCE ABSTRACTS	107
ACKNOWLEDGEMENT	109

1. Introduction

Detection of nuclear magnetic resonance (NMR) offers a unique possibility to study non-invasively living biological tissue, determine the structure of proteins, or to investigate materials in the solid state. Since the first observation of the phenomenon in 1945 by Purcell in paraffin (1) and by Bloch in liquid water (2) the way leading to nowadays NMR applications in medical diagnostics, analytical chemistry, or solid state physics, was paved with milestone inventions like Fourier-transform NMR (3) and magnetic resonance imaging (MRI) (4,5).

Most *in vivo* NMR applications are based on visualizing soft tissue structure and function (MRI), as well as on quantification and monitoring the dynamics of metabolites in living biological tissue (magnetic resonance spectroscopy or MRS). Proton MRI is based on the tissue specific water signal. Although a younger technique than MRS, MRI with its variable contrast mechanisms is already an invaluable diagnostic tool in radiology. *In vivo* proton MRS is used to detect resonances of protons in molecules dissolved in tissue water. MRS is less often used in clinical practice than MRI, because signal to noise ratio (SNR) in MR spectra scales with the concentration of single metabolites, while SNR in MR images scales with the integral over a spectral region including the water resonance. Moreover, MRS requires an extremely homogeneous magnetic field to provide high quality spectra. Adjustment of the parameters and calibration of the hardware for successful MR spectroscopic measurements in particular under *in vivo* conditions is technically demanding, and in most of the cases more time consuming than the setup of an MRI experiment. For these reasons, main applications of *in vivo* MRS are research studies on the characterization of pathologies or non invasive monitoring of drug induced effects on the metabolism in animal models.

The fundamental limiting factor in MRS is the relatively low sensitivity. The development of strong magnets up to 9.4 T for human and 21.1 T for animal applications tends to increase the sensitivity of MRS by enhancing the energy difference between discrete spin states (6,7). As a consequence, the detection limit in the human brain was pushed below metabolite concentrations of 1 millimolar (8,9). Expansion of the frequency range also results in better spectral resolution. However, higher static fields lead to high susceptibility for structural changes in the probe. Living organisms contain complex tissue structure. On borders between different regions strong field gradients (inhomogeneities) can arise, which are caused by the change in magnetic susceptibility between tissues. Inhomogeneities increase with field strength and lead to spectral line broadening, which can cancel out the resolution gain (10). Therefore, MRS applications take full advantage of strong and expensive magnets only with the help of resolution enhancement techniques, which minimize the inhomogeneities or their effect on resonance line shapes.

Minimization of inhomogeneities can be achieved with additional hardware, which compensates for the field gradients in the sample. A shim system uses several external shim coils creating orthogonal fields in form of spherical harmonics with variable amplitude (11). A linear combination of first and second order spherical harmonics can already compensate for the inhomogeneities caused by complex sample geometries. However, the maximum power of available shim systems is not designed for high-end magnets. Internal gradients on air-tissue and muscle-bone boundaries can currently be hardly corrected with commercially available hardware.

Another way to minimize the influence of inhomogeneities is to select the signal origin to be a relatively homogenous volume within the probe by avoiding signal from outside this region, which includes sources of inhomogeneities. By localising the signal to a region without strong structural variation, shimming efficiency and resolution can be regained (12). Localization combined with automatic shimming algorithms (13-15) simplifies and accelerates *in vivo* spectroscopic imaging and single-voxel MRS (11,16-18).

Yet, in cases where field inhomogeneities cannot be reduced by localization or compensated by shimming, alternative methods are required, which suppress the effect of such perturbations. These can include the introduction of a second spectral dimension to increase resonance line dispersion (19-21), magnetic susceptibility matching of sample and probe compartments (22), or magic angle spinning techniques (23,24).

A different, less technical approach of suppressing inhomogeneity effects is based on the detection of multiple quantum coherences (MQC). MQCs evolving in time with the relative frequency differences of their components have minimal spectral dispersion. A method using intramolecular MQCs of J-coupled spins (25) was recently applied *in vivo* to obtain resolution-enhanced spectra from the rat brain (26). Intermolecular multiple-quantum coherences (iMQC) were long considered negligible in liquid state NMR, because of their cancellation by spatial averaging and their low intensity. Since 1979 it is known that iMQCs can be transformed into detectable signal and since 1996 that iMQC spectroscopy provides resonances without inhomogeneous broadening not just for J-coupled spins (27,28). However, the physical mechanism of signal formation for intramolecular MQC- and iMQC-based techniques is fundamentally different.

Successful application of iMQC-spectroscopy was demonstrated in the presence of magnetic field gradients across sample tubes (27,29), in a drifting 25 T magnet (30), and *in vivo* in cold blooded (31) and warm blooded (32) animals. However, advantages of iMQC-detection are not limited to the resolution enhancement for MRS. iMQC-imaging offers a new and versatile contrast mechanism (33). By changing a sequence parameter called correlation gradient, the contrast in iMQC-images can be adjusted to be sensitive for structural changes of different sizes (34). Furthermore, given the high sensitivity of iMQCs to susceptibility changes (35), functional MRI signal based on the blood oxygenation dependent (BOLD) change is increased significantly compared to conventional techniques based on single quantum coherence detection (36).

The goal of this thesis was the optimization of intermolecular zero-quantum coherence (iZQC) spectroscopy for *in vivo* applications. The dissertation intends to give the theoretical background of this special technique by presenting first the strictly necessary elements of general NMR theory in Chapter 2, followed by a more detailed treatment of the unique features of iZQC spectroscopy in Chapter 3. The methodological optimization of the technique, as first part of the original work, is described in Chapter 4. This project targeted development and *in vitro* validation of a pulse sequence that substantially improved the quality of iZQC spectra. Analytical calculation as well as empirical parameter optimization was applied in the search for best water suppression and single voxel localization combined in one iZQC sequence. In Chapter 5, *in vivo* results acquired with the optimized sequence are presented. After the validation phase, the method was tested in competition with conventional MRS for application under severe experimental conditions. Chapter 6 presents an investigation on the physical limits of resolution enhancement in iMQC spectroscopy. It includes the description of extensive computer simulations of modified Bloch-equations, and comparison of the results with experimental spectra. It also intends to give a clarified view on the real potential regarding future applications of iZQC spectroscopy. Results presented in this dissertation were published in five scientific articles (32,37-40).

2. Basic principles of NMR

The nuclear magnetic resonance phenomenon depends on two fundamental properties of the atomic nucleus: the nuclear magnetism and the nuclear spin. Nuclear magnetism refers to the interaction of the nuclei with external magnetic fields and is characterized by the magnetic moment $\vec{\mu}$. Spin denotes the intrinsic angular momentum of a nucleus. It is characterized by the spin angular momentum operator \vec{I} , which in contrast to the macroscopic angular momentum is not a result of rotation. $\vec{\mu}$ and \vec{I} are connected by the relation

$$\vec{\mu} = \gamma \vec{I} = \gamma \hbar (I_x \hat{x} + I_y \hat{y} + I_z \hat{z}). \quad [2.1]$$

The scaling constant γ is called the gyromagnetic ratio, and is specified in $\text{rad s}^{-1}\text{T}^{-1}$. \hat{x} , \hat{y} and \hat{z} are unit vectors and

$$I_x = \frac{1}{2} \begin{pmatrix} 0 & 1 \\ 1 & 0 \end{pmatrix}, I_y = \frac{1}{2} \begin{pmatrix} 0 & -i \\ i & 0 \end{pmatrix} \text{ and } I_z = \frac{1}{2} \begin{pmatrix} 1 & 0 \\ 0 & -1 \end{pmatrix} \quad [2.2]$$

are the spin operators along Cartesian coordinate axes divided by \hbar . These operators have the cyclic commutation relationship

$$[I_x, I_y] = iI_z. \quad [2.3]$$

The absolute value of the nuclear spin is the Eigenwert of the operator $\sqrt{\vec{I}^2}$,

$$\sqrt{\langle \vec{I}^2 \rangle} = \hbar \sqrt{I(I+1)}, \quad [2.4]$$

where I is the spin quantum number ($I = \frac{1}{2}$ for protons). If \hat{z} defines the axis of the external magnetic field, the expectation value of the z -component of \vec{I} is

$$\langle I_z \rangle = \hbar m, \quad [2.5]$$

where m , the magnetic quantum number, can have $2I + 1$ values between $-I$ and I separated by $\Delta m = 1$. The quantum state of a spin is fully defined by the spin and magnetic quantum numbers. To describe the dynamics of nuclei the spin Hamiltonian is introduced. This consists basically of a term for electric and another one for magnetic interactions. For nuclei with $I = \frac{1}{2}$ the electric term vanishes, making possible to treat such spins as small spherical magnetic dipoles. In the present work ^1H nuclei were investigated, which have this property. Therefore, theoretical descriptions here are limited to this model.

Nuclear magnetic resonance can occur if the spin interacts with two external magnetic fields, a strong static field (the Zeeman interaction) and a much weaker radio-frequency (RF) field.

¹ The sign of the outcome could be also negative. In this dissertation the positive sign convention after van de Ven (41) will be consequently used. In the section about Product Operator Formalism the physical significance of this mathematical convention will be briefly described.

2.1 The Zeeman interaction

The interaction between a magnetic dipole $\vec{\mu}$ with an external static magnetic field \vec{B}_0 is called the Zeeman interaction and has the energy $-\vec{\mu} \cdot \vec{B}_0$ so that the Hamiltonian is given as

$$H = -\gamma \vec{I} \vec{B}_0. \quad [2.6]$$

If the magnetic induction along \hat{z} is B_0 , inserting Eq. [2.1] into Eq. [2.6] gives

$$H = \hbar \omega_0 I_z, \quad [2.7]$$

where

$$\omega_0 = -\gamma B_0 \quad [2.8]$$

is the Larmor frequency. For example, protons ($\gamma = 2.675 \times 10^8 \text{ rad s}^{-1} \text{T}^{-1}$) in a $B_0 = 17.6 \text{ T}$ magnetic field have a frequency of $\omega_0 / 2\pi \approx 750 \text{ MHz}$. On the one hand, as a consequence of Eq. [2.7] the energy levels of the nucleus are split in two (Zeeman splitting)

$$E_m = \omega_0 \langle I_z \rangle = \omega_0 \hbar m = \pm \frac{\hbar \omega_0}{2}. \quad [2.9]$$

On the other hand, because of the torque $\vec{\mu} \times \vec{B}_0$ experienced by the nuclear spin, the expectation values of $\vec{\mu}$ are time dependent. Thus, the physical effect of the Zeeman interaction can be imagined as the precession of small dipoles with frequency ω_0 around axes parallel or anti-parallel to \hat{z} .

2.2 Interaction with an oscillating RF-field

The nuclear magnetic resonance phenomenon occurs if an electromagnetic wave with the angular frequency ω_0 is applied, and a photon with the energy $\hbar \omega_0$ transfers one spin between the two Zeeman-states through stimulated absorption or emission. This can be achieved by an RF-coil that generates an oscillating field \vec{B}_1 perpendicular to \vec{B}_0 with frequency ω_1 , introducing the Hamiltonian term

$$H_{\text{RF}}(t) = -\frac{1}{2} \gamma \hbar B_1 \left[I_x \cos(\omega_1 t + \varphi) + I_y \sin(\omega_1 t + \varphi) \right] \quad [2.10]$$

where t is the time, and φ is the initial phase. The much weaker RF-field can have an effect on the spins precessing in the much stronger static field if it oscillates with the same frequency as the spins precess, or in other words, if RF-field and spins are in resonance. The small effect of a resonant RF-field accumulates in time and can modify almost arbitrarily the state of a spin system as it will be discussed below.

2.3 Internal spin interactions

Responsible for NMR are the above mentioned external interactions alone. However, the nuclei experience magnetic and electric fields depending on their nuclear and electronic environment. Thus, internal spin interactions play an important role in governing the dynamics of a spin system. The magnetic shielding effect by the atomic or molecular electron clouds, which interact with the nuclear spin angular momentum, and the direct dipolar interaction between nuclei play central roles in the present work. They are presented in more detail in the following.

2.3.1 Chemical shift

The Zeeman interaction is modified by the local electronic environment of a nucleus. The principal influence of the surrounding electrons is the magnetic shielding expressed by the tensor $\underline{\sigma}$. To include this shielding effect, the spin Hamiltonian has to be rewritten as

$$H = -\gamma \vec{I} \cdot \underline{\sigma} \cdot \vec{B}_0. \quad [2.11]$$

If the chemical shielding is weak, $\|\underline{\sigma}\| \ll 1$, the secular approximation applies and

$$H = \hbar \omega_0 (1 - \sigma_{zz}(\vartheta, \phi)) I_z, \quad [2.12]$$

with

$$\sigma_{zz}(\vartheta, \phi) = \sigma_{11} \sin^2 \vartheta \cos^2 \phi + \sigma_{22} \sin^2 \vartheta \sin^2 \phi + \sigma_{33} \cos^2 \vartheta \quad [2.13]$$

where σ_{11} , σ_{22} and σ_{33} are the principal values of $\underline{\sigma}$. The polar angle ϑ and the azimuthal angle ϕ describe the orientation of the magnetic field \vec{B}_0 in the principal axis system of the chemical shielding tensor. Thus, the Larmor precession frequency is displaced by the chemical shift, σ_{zz} , that is characteristic for different atomic or molecular groups. In an isotropic liquid, the motion averaged chemical shift Hamiltonian is equal to

$$H = \hbar \omega_0 (1 - \sigma_{iso}) I_z, \quad [2.14]$$

with

$$\sigma_{iso} = N^{-1} \iint \sigma_{zz}(\vartheta, \phi) d\vartheta d\phi, \quad [2.15]$$

where N is the normalization constant. It is a general convention to express σ in parts per million (ppm):

$$\sigma = \frac{\omega_0 - \omega}{\omega} \times 10^6, \quad [2.16]$$

where ω is the shifted Larmor frequency.

2.3.2 Direct dipolar interaction

The dipole field generated by a nucleus is

$$\mathbf{B}_{\text{dip}} = \frac{\mu_0}{4\pi} \frac{(3\cos^2\theta - 1)}{|\vec{r}|^3} \vec{\mu} \cdot \hat{z}. \quad [2.17]$$

Here, μ_0 is the vacuum permeability, and θ is the angle between the position vector \vec{r} and \hat{z} .

Spins \vec{I} with indices i or j ($i \neq j$) and spins \vec{S} with indices k or l ($k \neq l$) mutually interact through their dipole fields. In case that the spins are of the same species the dipole-dipole coupling is homonuclear ($\vec{I}_i\vec{I}_j$ or $\vec{S}_k\vec{S}_l$), if the spins are of different species it is heteronuclear ($\vec{I}_i\vec{S}_k$). The Hamiltonian of the dipolar interaction is

$$\begin{aligned} H_{\text{dip}} = \frac{\mu_0 \hbar^2}{4\pi} \left\{ \frac{\gamma_I^2}{r_{ij}^3} \left[\vec{I}_i \vec{I}_j - 3 \frac{(\vec{I}_i \vec{r}_{ij})(\vec{I}_j \vec{r}_{ij})}{r_{ij}^2} \right] + \frac{\gamma_S^2}{r_{kl}^3} \left[\vec{S}_k \vec{S}_l - 3 \frac{(\vec{S}_k \vec{r}_{kl})(\vec{S}_l \vec{r}_{kl})}{r_{kl}^2} \right] \right. \\ \left. + \frac{\gamma_I \gamma_S}{r_{ik}^3} \left[\vec{I}_i \vec{S}_k - 3 \frac{(\vec{I}_i \vec{r}_{ik})(\vec{S}_k \vec{r}_{ik})}{r_{ik}^2} \right] \right\}. \quad [2.18] \end{aligned}$$

In this case \vec{r} is the internuclear vector with absolute value r . In high magnetic fields Larmor precession of the magnetic moments averages out contributions from components perpendicular to \vec{B}_0 and the non-secular part of H_{dip} may be discarded:

$$H_{\text{dip}} = \frac{\mu_0 \hbar^2}{4\pi} (3\cos^2\theta - 1) \left[\frac{\gamma_I^2}{r_{ij}^3} (\vec{I}_i \vec{I}_j - 3I_{iz}I_{jz}) + \frac{\gamma_S^2}{r_{kl}^3} (\vec{S}_k \vec{S}_l - 3S_{kz}S_{lz}) + \frac{\gamma_I \gamma_S}{r_{ik}^3} (\vec{I}_i \vec{S}_k - 3I_{iz}S_{kz}) \right]. \quad [2.19]$$

In solids, internuclear vectors have fixed orientations and H_{dip} is high if averaged over the sample. In liquids, the macroscopic contribution of short range interactions (or couplings) is cancelled out by diffusion, because internuclear vectors take every possible orientation in space over the time scale relevant in an NMR experiment. Long-range dipolar couplings are usually neglected in liquid state NMR due to the r^{-3} dependency of H_{dip} . However, the number of such couplings grows with r^2 , and neglecting their contribution is not always justified.

2.4 Spin density operator

Samples used in NMR experiments contain about 10^{22} spins. A system containing a very large number of magnetically equivalent spins or groups of spins coupled with each other, forming magnetically equivalent but still independent entities, is called an ensemble. Spin ensembles are best described by the spin density operator defined as

$$\rho_{\text{full}} = \sum_{\psi} p_{\psi} |\psi\rangle\langle\psi|, \quad [2.20]$$

representing the ensemble average of all superposition states with the probability distribution $p_{\psi} \propto e^{-E_{\psi}/k_B T}$ (Boltzmann's distribution) and wave functions $|\psi\rangle$. For magnetic resonance applications it is usually sufficient to calculate expectation values of a restricted set of operators, which act exclusively on nuclear or electronic spin variables. The remaining degrees of freedom are referred to as the 'lattice'. The reduced density matrix is defined as

$$\rho = \text{Tr}_{\text{lattice}} \{ \rho_{\text{full}} \}, \quad [2.21]$$

where $\text{Tr}_{\text{lattice}}$ denotes a partial trace over the lattice variables. The matrix representation for an ensemble of non-interacting spin- $1/2$ is

$$\rho = \begin{pmatrix} \rho_{\alpha\alpha} & \rho_{\alpha\beta} \\ \rho_{\beta\alpha} & \rho_{\beta\beta} \end{pmatrix}, \quad [2.22]$$

with wave functions describing the superposition states

$$|\psi\rangle = c_{\alpha} |\alpha\rangle + c_{\beta} |\beta\rangle = \begin{pmatrix} c_{\alpha} \\ c_{\beta} \end{pmatrix}, \quad [2.23]$$

where $|c_{\alpha,\beta}|^2$ is the probability of the spin being in state $|\alpha\rangle$ or $|\beta\rangle$, respectively. Diagonal elements in the reduced density matrix are called populations of states $|\alpha\rangle$ and $|\beta\rangle$, whereas off-diagonal elements are coherences between these states. The expectation value of an observable Q for such a system is the trace

$$\langle Q \rangle = \text{Tr} \{ \rho Q \}, \quad [2.24]$$

and therefore

$$\rho = \begin{pmatrix} \frac{1}{2} + \langle I_z \rangle & \langle I_x - iI_y \rangle \\ \langle I_x + iI_y \rangle & \frac{1}{2} - \langle I_z \rangle \end{pmatrix}. \quad [2.25]$$

In other words all states of the ensemble for independent spin- $1/2$ nuclei may be described by specifying the components of the vector $\langle I_x \rangle \hat{x} + \langle I_y \rangle \hat{y} + \langle I_z \rangle \hat{z}$.

2.4.1 Product operator formalism

As demonstrated by Eq. [2.25], the reduced spin density matrix for an uncoupled spin- $1/2$ system can be expressed as the linear combination of I_x , I_y , I_z and the identity matrix. However, systems with three or more energy levels can no longer be described in the basis of these four operators. If two spins are coupled through the dipolar interaction, they form a system with four energy levels, because of the four possible conformations of their Zeeman-

states: $\uparrow\uparrow$, $\uparrow\downarrow$, $\downarrow\uparrow$ and $\downarrow\downarrow$. Figure 2.1 depicts such a system with the single- and multiple-quantum transitions between different states. Operator bases of 16 elements, like those presented in Table 2.1 and 2.2, are needed for the full mathematical representation of the quantum mechanics in this case. Such operator bases include two-spin operators, which can represent multiple quantum transitions up to the second order. Every process in this system can be described by a passive, an active and a target operator, all of which belong to the 16-element base. The conversion between operators is conventionally called base rotation, because applying four times the same operator one gets back to the initial term. RF-pulses act through one-spin operators along the rotation axis. For example a 90° pulse with phase x acting on the polarization of the spins I in thermal equilibrium, I_z , is described by the commutation $[I_z, I_x]$ and results in iI_y .² Longitudinal two-spin operators, present in the dipolar Hamiltonian (Eq. [2.19]), can be transformed by a non-selective RF-pulse, non-selective meaning that it affects all spin species in the system, to multiple-quantum coherences ($([2I_z S_z, I_x], S_x) = -2I_y S_y$). The master-equation for transformation in these 16-dimensional spaces is:

$$C_q \xrightarrow{C_p(\theta)} \begin{cases} C_q, & \text{if } [C_p, C_q] = 0 \\ C_q \cos \theta + i[C_p, C_q] \sin \theta, & \text{if } [C_p, C_q] \neq 0 \end{cases} \quad [2.26]$$

where C_q and C_p represent basis operators from Tables 2.1 and 2.2. Equation [2.26] describes the rotation of C_q around the axis of C_p by an angle of θ .

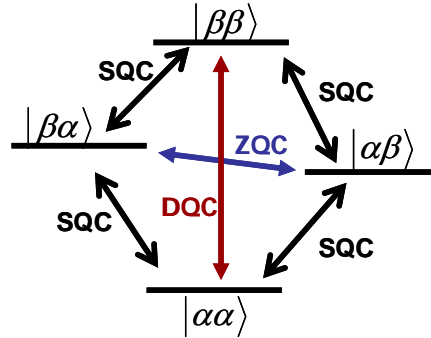


Figure 2.1: Energy level diagram of a coupled two-spin system. Single-quantum coherences (SQC), zero-quantum coherences (ZQC) and double-quantum coherences (DQC) are indicated by arrows.

2.4.2 Magnetization

Equation [2.24] can be applied for the calculation of the polarization of a spin system in the thermal equilibrium. The expectation value of a single spin polarization can be written as

$$\langle I_z \rangle = \text{Tr}\{\rho I_z\} = \frac{\sum_m \hbar m e^{-\frac{E_m}{k_B T}}}{\sum_m e^{-\frac{E_m}{k_B T}}}, \quad [2.27]$$

² Direction of the base rotation defines the sign of the outcome. As already mentioned earlier in this chapter, we use the convention propagated in Ref. (41). If used consequently, both, positive and negative sign conventions have the same predictive power.

Table 2.1 Basis operators for a coupled two-spin- $\frac{1}{2}$ system. Here, spins I and S can be of the same species.

<i>one-spin operators</i>	<i>name</i>
I_z, S_z	polarization of spins I and S
I_x, S_x	in-phase x-coherence of spins I and S
I_y, S_y	in-phase y-coherence of spins I and S
<i>two-spin operators</i> ^a	<i>name</i>
$2I_xS_z, 2I_zS_x$	x-coherence of spin I in antiphase with respect to spin S (and vice versa)
$2I_yS_z, 2I_zS_y$	y-coherence of spin I in antiphase with respect to spin S (and vice versa)
$2I_xS_x, 2I_yS_y, 2I_xS_y, 2I_yS_x$	two-spin zero- and double-quantum coherences of spin I and S
$2I_zS_z$	longitudinal two-spin order of spin I and S

^a The factors 2 in front of the two-spin operators are arbitrarily chosen to simplify the commutation algebra analogous to Eq. [2.3].

Table 2.2 One-spin and two-spin basis operators for a system of coupled spin- $\frac{1}{2}$ pairs. Note that the non-diagonal coherences are written in terms of raising and lowering operators, $I_+ = I_x + iI_y$ and $I_- = I_x - iI_y$ (idem for S_+ and S_-). Since I_+ and I_- are linear combinations of I_x and I_y , these coherences are, in turn, combinations of those shown in Table 2.1. Here, spins I and S can be of the same species.

<i>one-spin operator states</i>	<i>name</i>
I_z, S_z	polarization of spins I and S
I_+, S_+	in-phase positive single-quantum coherence (+SQC) of spins I and S
I_-, S_-	in-phase negative single-quantum coherence (-SQC) of spins I and S
<i>two-spin operators</i>	<i>name</i>
I_+S_z, I_zS_+	+SQC of spin I in antiphase with respect to spin S (and vice versa)
I_-S_z, I_zS_-	-SQC of spin I in antiphase with respect to spin S (and vice versa)
I_+S_+	in-phase positive double-quantum coherences (+DQC) of spin I and S
I_-S_-	in-phase negative double-quantum coherences (-DQC) of spin I and S
I_+S_+, I_-S_-	in-phase zero-quantum coherence (ZQC) of spins I and S
I_zS_z	longitudinal two-spin order of spin I and S

where k_B is the Boltzmann constant and T the temperature. After cropping the Taylor expansion of the exponential functions before the quadratic term (high temperature approximation), Eq. [2.26] becomes

$$\langle I_z \rangle = \frac{\gamma \hbar^2 I(I+1)}{3k_B T} B_0. \quad [2.28]$$

The polarization of a spin ensemble is called magnetization (M) and is defined as

$$\langle M_z \rangle = \sum_i \frac{\mu_i}{V} = c\gamma \langle I_z \rangle, \quad [2.29]$$

where V is the sample volume and c the spin density. The final form of the magnetization at thermal equilibrium in the high temperature approximation is

$$M_0 = c \frac{\gamma^2 \hbar^2}{4k_B T} B_0. \quad [2.30]$$

2.4.3 The Liouville – von Neumann equation

The evolution of the reduced spin density matrix with time may be deduced from the Schrödinger equation and is called the Liouville – von Neumann equation (41):

$$i \frac{\partial \rho}{\partial t} = [H, \rho], \quad [2.31]$$

For the case of a time independent Hamiltonian operator, the solution is

$$\rho(t) = U(t) \rho(0) U^{-1}(t) = e^{-iHt} \rho(0) e^{iHt}, \quad [2.32]$$

where U is a linear propagator.

2.5 Magnetization dynamics

The linearly polarized oscillating RF-field is the sum of two counter-rotating circularly polarized components of amplitude B_1 . Making a coordinate transformation to the frame where one \vec{B}_1 component is stationary (rotating frame), has the advantage that the spin Hamiltonian (without internal interaction terms) will be time-independent and Eq. [2.32] applies. The second component rotates in this frame with double frequency and can be ignored, provided that $B_1 \ll B_0$. In isotropic samples with non-interacting spins, Eq. [2.32] allows for the description of NMR signal evolution as simple rotations of the magnetization vector $\vec{M}(t)$ in the Cartesian coordinate system, starting with the initial value of

$$\vec{M}(0) = \begin{pmatrix} 0 \\ 0 \\ M_0 \end{pmatrix}, \quad [2.33]$$

called thermal equilibrium magnetization. The equation of motion for the magnetization vector is

$$\frac{d\vec{M}}{dt} = \gamma \vec{M} \times \vec{B}_0. \quad [2.34]$$

Incorporating spin relaxation and molecular diffusion terms into Eq. [2.33] results in the Bloch-Torrey equations:

$$\frac{d\vec{M}}{dt} = \gamma \vec{M} \times \vec{B}_0 - \underline{R} [\vec{M} - \vec{M}(0)] + D \nabla^2 \vec{M}, \quad [2.35]$$

with

$$\underline{R} = \begin{pmatrix} 1/T_2 & 0 & 0 \\ 0 & 1/T_2 & 0 \\ 0 & 0 & 1/T_1 \end{pmatrix}. \quad [2.36]$$

Here, D represents the diffusion constant, T_1 the spin-lattice and T_2 the spin-spin relaxation times. In real samples, however, in particular for *in vivo* NMR experiments, the magnetization becomes a function of position and diffusion has to be described by a tensor.

3. Intermolecular multiple-quantum coherence NMR spectroscopy

In this chapter, the theory of iMQC-signal formation and the characteristics of iMQC-spectra will be discussed. iMQC methods derive from the prototype pulse sequence for the independent detection of different orders of iMQC, which was dubbed CRAZED (*COSY revamped with asymmetric z-gradient echo detection*) (42,43). Resolution enhancement in 2D iMQC spectra was first demonstrated for a CRAZED-like experiment, which selects intermolecular zero-quantum coherences (iZQC) (Fig. 3.1) and was termed HOMOGENIZED (*homogeneity enhancement by intermolecular zero-quantum detection*) (27). The pulse sequence developed in this thesis derives from HOMOGENIZED, and therefore, the theoretical basics will be described focusing on the original sequence.

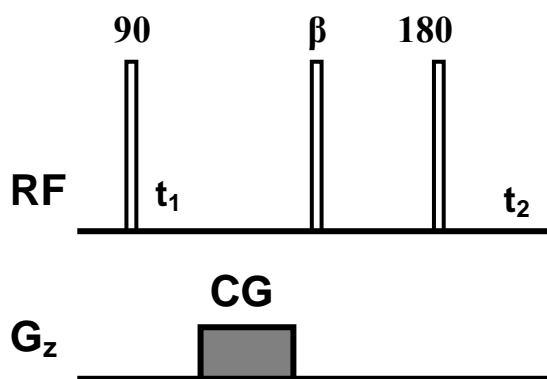


Figure 3.1: HOMOGENIZED pulse sequence (27). Symbols: empty bars – non-selective RF-pulses, CG – correlation gradient. RF-pulse angles are indicated. RF-pulse phases are kept constant and, therefore, not indicated. The sequence can be improved by phase cycling the first pulse (e.g. (x , $-x$)).

The theoretical description of iMQC experiments mostly follows either a quantum-mechanical or a classical approach, which apply the product operator formalism or solve modified Bloch equations, respectively. Both treatments result in identical quantitative predictions (44-46). Analytical solutions for the spin dynamics were derived in both frameworks, attempting to describe experiments more and more accurately (27,29,37,42,43,47-84). However, a general analytical solution for iMQC-signal evolution including the effects of diffusion, relaxation, arbitrary sample structure and arbitrary gradient modulation is still not available.

Here we employ the quantum-mechanical framework to obtain a precise picture of signal formation during the HOMOGENIZED experiment on a nuclear level. The classical framework will serve for describing resolution enhancement in iZQC-spectra, and Bloch-equations will be used to analyse the signal evolution in more detail, because this approach allows for the convenient introduction of relaxation and diffusion effects in the calculations.

3.1 The quantum picture of *i*ZQC-signal formation

iMQCs originate from long-range dipolar couplings. The dipolar Hamiltonian of a spin ensemble can be derived from Eq. [2.19] and is the double sum over all interacting spins.

$$H_{\text{dip}}^{\text{full}} = \sum_{i=0}^N \sum_{j=0}^N D_{ij} (\vec{I}_i \vec{I}_j - 3I_{iz} I_{jz}) + \sum_{k=0}^M \sum_{l=0}^M D_{kl} (\vec{S}_k \vec{S}_l - 3S_{kz} S_{lz}) + \sum_{i=0}^N \sum_{k=0}^M D_{ik} (\vec{I}_i \vec{S}_k - 3I_{iz} S_{kz}), \quad [3.1]$$

with

$$D_{ij} \equiv \frac{\mu_0}{4\pi} \frac{\gamma_I^2 \hbar^2}{4r_{ij}^3} (3\cos^2 \theta_{ij} - 1),$$

$$D_{kl} \equiv \frac{\mu_0}{4\pi} \frac{\gamma_S^2 \hbar^2}{4r_{kl}^3} (3\cos^2 \theta_{kl} - 1) \text{ and}$$

$$D_{ik} \equiv \frac{\mu_0}{4\pi} \frac{\gamma_I \gamma_S \hbar^2}{4r_{ik}^3} (3\cos^2 \theta_{ik} - 1). \quad [3.2]$$

Here, N and M are the number of I and S spins, respectively. The constant D_{ik} is the dipolar coupling constant, specifying the magnitude of dipolar couplings. For adjacent spins, D_{ik} can be on the order of hundreds of Hz, still their time average is zero because of diffusion. Thus, inside a sphere determined by the diffusion distance of molecules during an NMR experiment, $r_{\text{diff}} = \sqrt{2Dt}$ (where D is the diffusion constant), all individual interactions can be ignored. Outside this sphere dipolar couplings can be treated as constant in time. Eqs. [3.1] and [3.2] suggest that long-range couplings are relatively weak ($\sim r^{-3}$), and are averaged out by magnetic isotropy (angular dependence). However, the sum of all dipolar interactions at a given spin site only falls off with r^{-1} , because the number of couplings grows with r^2 . Therefore, long-range dipolar interactions have to be explicitly considered if magnetic isotropy is broken. This happens whenever the sample is not spherical and homogeneous or when gradient pulses are applied during the pulse sequence.

For long-range dipolar couplings to be accounted for in the quantum mechanical treatment of iMQC sequences, the Taylor-series expansion of the spin density matrix has to be considered at least up to the quadratic term, which in thermal equilibrium takes the form

$$\rho = 2^{-N-M} \left[1 - \varepsilon \sum_{i,k}^{N,M} (I_{zi} + S_{zk}) + \frac{\varepsilon^2}{2} \sum_{i,j,k,l}^{N,M} (I_{zi} I_{zj} + S_{zk} S_{zl} + I_{zi} S_{zk}) \right], \quad [3.3]$$

where $\varepsilon = \hbar\omega_0/kT$ is the ratio of Zeeman-splitting and thermal energy. The last term of Eq. [3.3] contains homo- and heteronuclear longitudinal two-spin operators, which can be transformed by a single RF-pulse into zero- and double-quantum operators, thus

$$\rho = 2^{-N-M} \left[1 - \varepsilon \sum_{i,k}^{N,M} (I_{yi} + S_{yk}) + \frac{\varepsilon^2}{2} \sum_{i,j,k,l}^{N,M} (I_{yi} I_{yj} + S_{yk} S_{yl} + I_{yi} S_{yk}) \right]. \quad [3.4]$$

In the HOMOGENIZED sequence presented in Fig. 3.1, this is done by the first 90° -pulse. During the following t_1 evolution period the system evolves under the effect of the chemical

shift. For the sake of clarity, we will continue the analysis only for the second order homonuclear I-spin term $I_{yi}I_{yj}$, so that

$$\rho_{\text{homo}}(t_1) = 2^{-N-1} \varepsilon^2 \sum_{i,j}^N \left[I_{yi} \cos(\Delta\omega t_1) + I_{xi} \sin(\Delta\omega t_1) \right] \times \left[I_{yj} \cos(\Delta\omega t_1) + I_{xj} \sin(\Delta\omega t_1) \right], \quad [3.5]$$

where $\Delta\omega$ is the chemical shift of the I spins. The coherence selection gradient (CG) with strength G and duration T , modulates the evolution frequency along the direction \hat{s} at positions s_i and s_j , and therefore

$$\rho_{\text{homo}}(t_1) = 2^{-N-1} \varepsilon^2 \sum_{i,j}^N \left[I_{yi} \cos(\Delta\omega t_1 + k_m s_i) + I_{xi} \sin(\Delta\omega t_1 + k_m s_i) \right] \times \left[I_{yj} \cos(\Delta\omega t_1 + k_m s_j) + I_{xj} \sin(\Delta\omega t_1 + k_m s_j) \right], \quad [3.6]$$

where $k_m = \gamma GT$. The subsequent β -pulse transforms the reduced density matrix into

$$\begin{aligned} \rho_{\text{homo}}(t_2 = 0) &= 2^{-N-1} \varepsilon^2 \\ &\times \sum_{i,j}^N \left[I_{yi} \cos(\Delta\omega t_1 + k_m s_i) \cos\beta - I_{zi} \cos(\Delta\omega t_1 + k_m s_i) \sin\beta + I_{xi} \sin(\Delta\omega t_1 + k_m s_i) \right] \\ &\times \left[I_{yj} \cos(\Delta\omega t_1 + k_m s_j) \cos\beta - I_{zj} \cos(\Delta\omega t_1 + k_m s_j) \sin\beta + I_{xj} \sin(\Delta\omega t_1 + k_m s_j) \right]. \end{aligned} \quad [3.7]$$

Knowing that cosine is a pair function [$\cos(-A) = \cos A$], for $\beta = 45^\circ$ we get

$$\begin{aligned} \rho_{\text{homo}}(t_2 = 0) &= 2^{-N-1} \varepsilon^2 \sum_{i,j}^N \left[-I_{yi}I_{zj} \cos(\Delta\omega t_1 + k_m s_i) \cos(\Delta\omega t_1 + k_m s_j) \right. \\ &\quad - I_{zi}I_{yj} \cos(\Delta\omega t_1 + k_m s_i) \cos(\Delta\omega t_1 + k_m s_j) \\ &\quad - \sqrt{2}I_{zi}I_{xj} \cos(\Delta\omega t_1 + k_m s_i) \sin(\Delta\omega t_1 + k_m s_j) \\ &\quad \left. - \sqrt{2}I_{xi}I_{zj} \cos(\Delta\omega t_1 + k_m s_i) \sin(\Delta\omega t_1 + k_m s_j) \right] \\ &\quad + \text{terms not converted into observables by the dipolar couplings.} \end{aligned} \quad [3.8]$$

Applying the relations $\cos A \cos B = \frac{1}{2}[\cos(A+B) + \cos(A-B)]$, $\cos(-A) = \cos A$ and $\sin A \cos B = \frac{1}{2}[\sin(A+B) + \sin(A-B)]$ we can transform the coefficients into

$$\begin{aligned} \cos(\Delta\omega t_1 + k_m s_i) \cos(\Delta\omega t_1 + k_m s_j) &= \frac{\cos[2\Delta\omega t_1 + k_m(s_i + s_j)]}{2} + \frac{\cos[k_m(s_i - s_j)]}{2} \\ \cos(\Delta\omega t_1 + k_m s_j) \cos(\Delta\omega t_1 + k_m s_i) &= \frac{\cos[2\Delta\omega t_1 + k_m(s_i + s_j)]}{2} + \frac{\cos[k_m(s_i - s_j)]}{2} \\ \cos(\Delta\omega t_1 + k_m s_i) \sin(\Delta\omega t_1 + k_m s_j) &= \frac{\sin[2\Delta\omega t_1 + k_m(s_i + s_j)]}{2} + \frac{\sin[k_m(s_j - s_i)]}{2} \\ \cos(\Delta\omega t_1 + k_m s_j) \sin(\Delta\omega t_1 + k_m s_i) &= \frac{\sin[2\Delta\omega t_1 + k_m(s_i + s_j)]}{2} + \frac{\sin[k_m(s_i - s_j)]}{2}. \end{aligned}$$

Terms which depend on the absolute position of the spins in the sample will average to zero. This affects all linear terms in Eq. [3.4], which are modulated by the CG with the function $\sin(k_m s_{ij})$. Spatial averaging cancels out most of the quadratic terms, too. The only survivors are those depending on a difference in position. However, knowing that sine is an odd function, and that for every spin pair 'ij', there is another interaction 'ji' in the sample, all terms modulated by a sine will be cancelled. Therefore, the term which remains is the one proportional to $\cos[k_m(s_i - s_j)]$. Evolution during t_2 under the action of the dipolar and chemical shift Hamiltonian creates the iZQC-signal and the observable density matrix writes

$$\rho_{\text{hom o, OBS}}(t_2) = -3 \cdot 2^{-N-2} \varepsilon^2 e^{-i\Delta\omega t_2 I_z} \left\{ \sum_{i,j}^N (I_{xi} + I_{xj}) \cos[k_m(s_i - s_j)] \sin(D_{ij} t_2) \right\} e^{i\Delta\omega t_2 I_z}. \quad [3.9]$$

The product $D_{ij} t_2$ is very small, which allows for the approximation $\sin(D_{ij} t_2) \approx D_{ij} t_2$, so that the iZQC-signal amplitude for a spin at position $s_i = 0$ is

$$S = \left| 3 \cdot 2^{-N-2} \varepsilon^2 \sum_j^N D_{ij} \cos(k_m s_j) \right|, \quad [3.10]$$

and in a large sample the following proportionality applies (42)

$$S \propto \int_{V > V_{\text{cutoff}}} \frac{3 \cos^2 \theta - 1}{r^3} \cos(k_m s) r^2 \sin \theta dr d\theta d\phi, \quad [3.11]$$

where r , θ and Φ are the spherical coordinates and V_{cutoff} is the volume inside which diffusion efficiently averages out dipolar couplings, as discussed earlier.

Figure 3.2 depicts the signal contribution as a function of r by showing the solution of Eq. [3.11] for $k_m = 100 \text{ mm}^{-1}$. The largest contribution is obtained from nearby spins, roughly between r_{cutoff} and $5/k_m$. Since k_m is a function of sequence parameters (G and T), the spatial reach of the iZQC-signal can be varied on a scale limited at the lower end by diffusion ($\sim 10 \mu\text{m}$ for water), and at the upper end by insufficient suppression of unwanted signal contributions due to weak gradients.

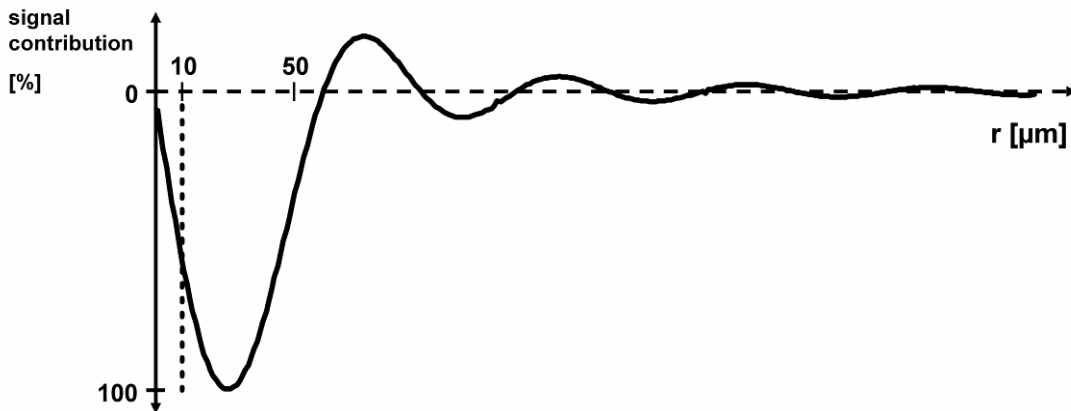


Figure 3.2: iZQC-signal contribution as a function of distance at an arbitrary position in the sample ($k_m = 100 \text{ mm}^{-1}$). The minimum was set to 100%. The vertical delimiter indicates the approximate maximum distance for which diffusion averages out dipolar interactions.

3.1.1 Spectral patterns

For the discussion of HOMOGENIZED spectral patterns, a quantitative quantum-mechanical analysis is not necessary. Simple base rotations of two-spin product operators, with the most complicated weighting or normalization coefficients neglected, are an elegant way of predicting signal components and spectral structures. Usually it is enough to calculate the coherence transfer pathway of those coherences, which are converted into observable operators at the end of a sequence. Optionally, one can decide to include specific coefficients in the calculation to get a clarified view about its effect on the signal.

The coherence transfer pathway of the homonuclear iZQC in the HOMOGENIZED sequence after the first 90° excitation pulse, including also the effect of the second β -pulse, is:

$$\begin{aligned}
 & I_i^+ I_j^- + I_i^- I_j^+ = 2(I_{xi} I_{xj} + I_{yi} I_{yj}) \\
 & \xrightarrow{\beta\text{-pulse, } \{I_x(\beta)\}} \frac{1}{2}(-I_{yi} I_{zj} \cos \beta \sin \beta - I_{zi} I_{yj} \cos \beta \sin \beta) + \text{unobservable terms} \\
 & \xrightarrow{\text{dipolar couplings, } \{D_{ij} I_{zi} I_{zj}\}} \frac{1}{4}(-I_{xi} \cos \beta \sin \beta - I_{xj} \cos \beta \sin \beta) = -\frac{\sin 2\beta}{8}(I_{xi} + I_{xj}) \\
 & \xrightarrow{\text{chemical shift, } \{I_z\}} \xrightarrow{\text{refocusing pulse, } \{I_x(180^\circ)\}} -\frac{\sin 2\beta}{8}(I_i^- + I_j^-), \quad [3.12]
 \end{aligned}$$

and similarly for $S_k^+ S_l^- + S_k^- S_l^+$. Terms which are not transformed into detectable operators at the end of the sequence are indicated as “unobservable terms”. Equation [3.12] implies that the observable signal intensity will be proportional to $\sin 2\beta$, and maximum intensity is reached if $\beta = 45^\circ$. For the heteronuclear coherence transfer pathway, the two iZQC operators have to be treated separately, since their evolution frequencies during t_1 can be positive or negative. Terms evolving during t_2 with $\Delta\omega_I$ originate from iZQCs evolving during t_1 with $(\Delta\omega_I - \Delta\omega_S)$, called P-type coherences,

$$\begin{aligned}
 & I_i^+ S_k^- (\Delta\omega_I - \Delta\omega_S) = I_{xi} S_{xk} - iI_{xi} S_{yk} + iI_{yi} S_{xk} + I_{yi} S_{yk} \\
 & \xrightarrow{\beta\text{-pulse, } \{I_x(\beta), S_x(\beta)\}} iI_{xi} S_{zk} \sin \beta - iI_{zi} S_{xk} \sin \beta \\
 & \quad - I_{yi} S_{zk} \cos \beta \sin \beta - I_{zi} S_{yk} \cos \beta \sin \beta + \text{unobservable terms} \\
 & \xrightarrow{\text{dipolar couplings, } \{D_{ik} I_{zi} S_{zk}\}} \frac{1}{2}(-iI_{yi} \sin \beta + iS_{yk} \sin \beta - I_{xi} \cos \beta \sin \beta - S_{xk} \cos \beta \sin \beta) \\
 & \quad = \frac{\sin \beta}{2i}(I_{yi} - S_{yk}) - \frac{\sin 2\beta}{4}(I_{xi} + S_{xk}), \quad [3.13]
 \end{aligned}$$

and from iZQCs evolving with $-(\Delta\omega_I - \Delta\omega_S)$, called N-type coherences

$$\begin{aligned}
 & I_i^- S_k^+ (\Delta\omega_S - \Delta\omega_I) = I_{xi} S_{xk} + iI_{xi} S_{yk} - iI_{yi} S_{xk} + I_{yi} S_{yk} \\
 & \xrightarrow{\beta\text{-pulse, } \{I_x(\beta), S_x(\beta)\}} -iI_{xi} S_{zk} \sin \beta + iI_{zi} S_{xk} \sin \beta \\
 & \quad - I_{yi} S_{zk} \cos \beta \sin \beta - I_{zi} S_{yk} \cos \beta \sin \beta + \text{unobservable terms} \\
 & \xrightarrow{\text{dipolar couplings, } \{D_{ik} I_{zi} S_{zk}\}} \frac{1}{2}(iI_{yi} \sin \beta - iS_{yk} \sin \beta - I_{xi} \cos \beta \sin \beta - S_{xk} \cos \beta \sin \beta) \\
 & \quad = \frac{i \sin \beta}{2}(I_{yi} - S_{yk}) - \frac{\sin 2\beta}{4}(I_{xi} + S_{xk}). \quad [3.14]
 \end{aligned}$$

Applying a similar derivation as in Eqs. [3.13] and [3.14], one can calculate the P- and N-type coherences produced by S-spin terms, evolving during t_2 with $\Delta\omega_S$. Effects of the refocusing pulse and of the chemical shift were not included for clarity. They, however, can modify the spectrum, and will be accounted for in the context of sequence optimization in Sec. 4.1.1. In the heteronuclear case, the signal dependence on the β -pulse is a bit more complex than in the homonuclear case. It can be seen, that heteronuclear peaks will not vanish for any β . The ratio of P to N-type peak intensities along $\Delta\omega_I$ or $\Delta\omega_S$ on the second frequency axis depends on $\tan^2(\beta/2)$ (78). Thus, equal peak intensities are obtained if $\beta = 90^\circ$. For $\beta = 45^\circ$ the ratio is about 5.8.

Figure 3.3 presents the sketch of a HOMOGENIZED spectrum for a two-spin system, as it has been calculated using Eqs. [3.12-14]. Since the evolution frequency of homonuclear iZQCs in the t_1 period is zero and during t_2 observable one-spin operators evolve with the chemical shift of the transverse component, Eq. [3.12] predicts one peak at $(0, \Delta\omega_I)$. Another peak at $(0, \Delta\omega_S)$ will be formed by homonuclear S-spin coherences. Heteronuclear P-type coherences generate peaks at $(\Delta\omega_I - \Delta\omega_S, \Delta\omega_I)$ and $(\Delta\omega_S - \Delta\omega_I, \Delta\omega_S)$, while N-type coherences appear at $(\Delta\omega_S - \Delta\omega_I, \Delta\omega_I)$ and $(\Delta\omega_I - \Delta\omega_S, \Delta\omega_S)$.

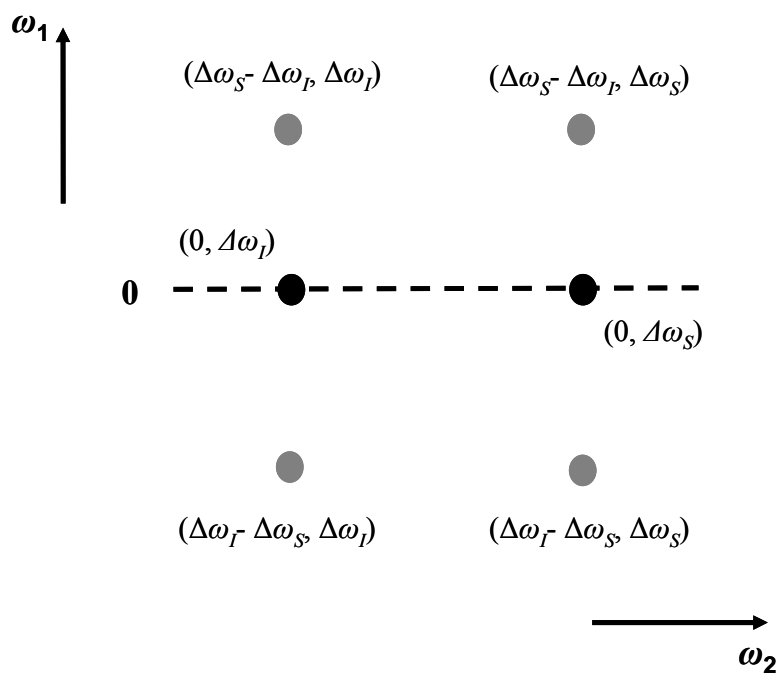


Figure 3.3: The sketch of a HOMOGENIZED spectrum of a two-spin system. Black dots are axial peaks, grey dots are cross-peaks.

3.2 The distant dipolar field (DDF)

Although analysis of product operators readily yields information on peak positions and intensities in the spectrum, here we will follow the classical approach for the treatment of signal evolution, which allows including the effect of relaxation and diffusion more easily. Fragments and figures from a previously published work will be employed (32).

The classical picture uses the mean field approximation that takes into account the small local contribution to \vec{B}_0 of the magnetization created by the distant spins themselves (the distant dipolar field, DDF). Direct manifestations of the DDF are, for example, pulse-dependent line shape modulation, accompanied by a slight frequency shift (about 1 Hz at 9.4 T for water) (85), or multiple spin echoes (MSE). MSE were first detected at very low temperatures in solid ^3He (86), in liquid ^3He (87), and in water at room temperature (47,88-90). In the classical framework of iMQC spectroscopy formation of MSE is the key process. Pulse sequences like HOMOGENIZED select one distinct echo, corresponding to one coherence order. The DDF, which causes MSE formation, has the form

$$\vec{B}_{\text{DDF}}(\vec{r}) = \frac{\mu_0}{4\pi} \int \frac{1-3\cos^2\theta}{2|\vec{r}-\vec{r}'|^3} [3M_z(\vec{r}')\hat{z} - \vec{M}(\vec{r}')] d^3r', \quad [3.15]$$

where \vec{r} and \vec{r}' are position vectors, and θ is the angle between \vec{B}_0 and the interspin vector $|\vec{r}-\vec{r}'|$. Analogous to the dipolar Hamiltonian for a spin ensemble in the quantum mechanical treatment, \vec{B}_{DDF} vanishes in homogeneous and isotropic samples and can therefore be neglected in most liquid state NMR experiments. If isotropy is broken, for example after modulating transverse magnetization by application of magnetic field gradients, the DDF becomes non-zero and can cause formation of MSE. The HOMOGENIZED pulse sequence (Fig. 3.1) uses a correlation gradient to achieve the necessary modulation of the DDF to avoid cancellation. Assume that the wavelength of gradient modulation is much shorter than the diameter of the sample. In this case the 1D modulation with $\cos(k_m s)$ over the sample allows expressing the effective DDF in the rotating frame as a 1D function of the modulation coordinate s (86,91), which writes

$$\vec{B}_{\text{DDF}}(s) = \mu_0 \Delta_s [M_z(s)\hat{z} - \vec{M}(s)/3], \quad [3.16]$$

where $\Delta_s = [3(\hat{s} \cdot \hat{z})^2 - 1]/2$. The DDF is the strongest for $\hat{s} \parallel \hat{z}$ and therefore in the following, if not mentioned otherwise, this case will be discussed. Figure 3.4 illustrates schematically the evolution of the magnetization vector during the HOMOGENIZED pulse sequence at eight representative positions within one modulation period (rows in Fig. 3.4a). The first pulse rotates the equilibrium magnetization into the transverse plane (left column in Fig. 3.4a). After free precession in the evolution period t_1 , the CG winds up transverse magnetization into a helix (centre column in Fig. 3.4a) with a 1D spatial phase and half-pitch $d_c = \pi/k_m$, called the correlation distance. The second RF-pulse rotates part of the magnetization back along the z -axis (right column in Fig. 3.4a), which then gives rise to the DDF as described in Eq. [3.16]. At this time point $t_2 = 0$, no signal is detectable, because the transverse magnetization (M^+) is fully dephased. Each of the vectors in the eight representative positions is exactly cancelled by a second vector (Fig. 3.4b, top). However, for $t_2 > 0$ the DDF starts refocusing M^+ . In the upper four positions in Fig. 3.4a the DDF has opposite sign compared to the lower four positions. Under the DDF, transverse magnetization precesses clockwise in positions one, two, and three, and counter-clockwise in positions five, six, and seven. Eventually an echo is formed (Fig. 3.4b, bottom).

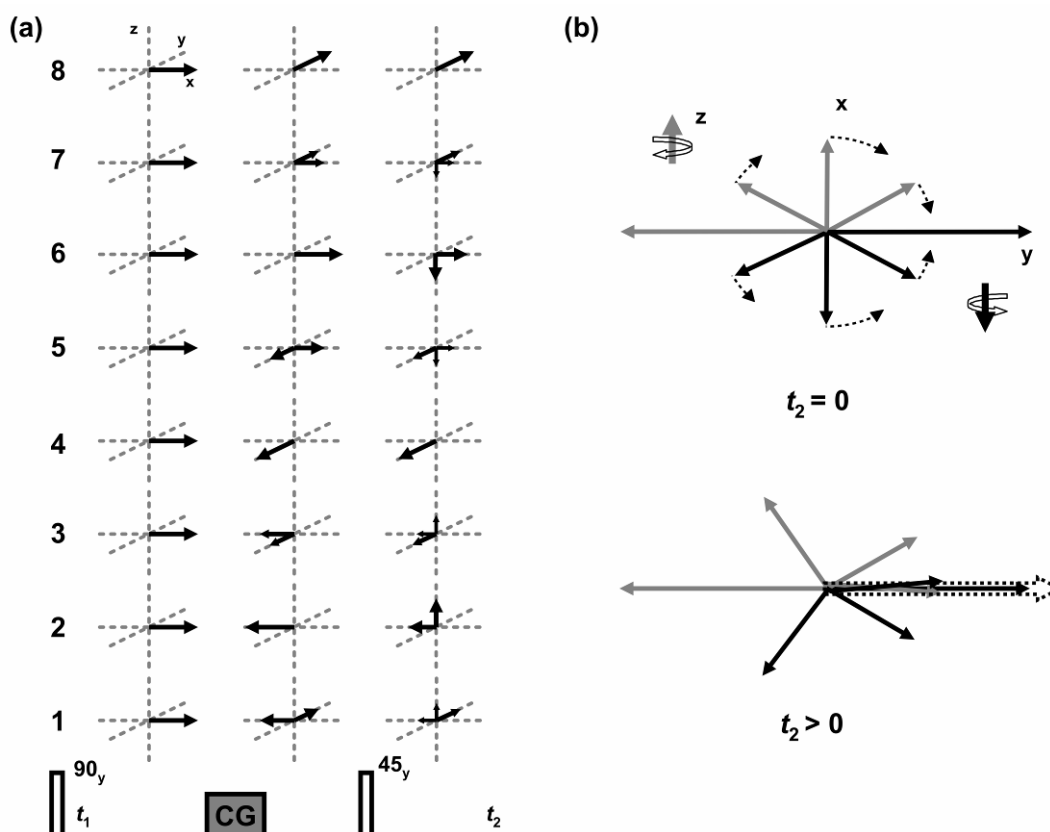


Figure 3.4: Schematic illustration of DDF-signal formation in a HOMOGENIZED sequence. (a) Evolution of the magnetization vector in the rotating frame for eight different positions within one gradient modulation period. First, second, and third column correspond to time points immediately after 90°-pulse, CG, and 45°-pulse, respectively. Magnetization vectors are shown as components M_x , M_y , and M_z . During t_2 , M_z provides the spatially varying DDF. (b) Transverse magnetization at the eight positions, shown in the x - y plane. Transverse magnetization in positions 1-4 and 5-8 is indicated as grey and black arrows, respectively. At $t_2 = 0$ (top) M^+ is fully dephased. Each vector experiences a different DDF and precesses at different angular velocity (dotted arrows). For $t_2 > 0$ part of M^+ is refocused, eventually forming an echo. The vector sum is shown as dotted empty arrow (bottom).

The time scale of this process depends on the maximum frequency of the DDF (ω_d), which is the reciprocal of the dipolar time constant $\tau_d = (\gamma\mu_0 M_0)^{-1}$, also called demagnetizing time. If the second pulse is applied with 90°, the local intensity of the DDF, and also ω_d will be maximal. Since τ_d is on the order of 100 ms at high fields, HOMOGENIZED signal is typically acquired as spin echo after an additional 180° pulse (see Fig. 3.1).

The scheme in Fig. 3.4a also confirms the prediction of the quantum treatment that refocusing under the DDF is a local process and will not be disturbed by field variations on a scale large compared to k_m^{-1} .

3.3 Resolution enhancement

Figure 3.5 schematically illustrates how the local nature of echo formation results in line-narrowing along the indirect dimension in HOMOGENIZED spectra acquired under macroscopic field distortions. An frequency profile of a 500 μm sample was generated with the Matlab built-in function “humps”. The frequency distribution in Fig. 3.5 ($\delta\omega$) leads to an

irregular line shape of the peak in a conventional NMR spectrum from such a voxel (dotted peak in the inset). Now, we approximate the DDF peak line shape. For a gradient modulation of $k_m = 100 \text{ mm}^{-1}$, major contribution to the DDF-signal comes from interactions within a sphere with roughly $50 \text{ }\mu\text{m}$ radius for each individual spin. Therefore, only a $100 \text{ }\mu\text{m}$ section of the frequency distribution function around the actual position r_n is considered ($\delta\vec{\omega}_n$). For the central position in the voxel this section is indicated by dotted vertical lines in Fig 3.5. Over such a $100 \text{ }\mu\text{m}$ stretch field inhomogeneity is much smaller than over the whole voxel ($\int |\delta\vec{\omega}_n| \ll \int |\delta\vec{\omega}|$). The DDF-signal at r_n depends on $\exp(i\tau \int |\delta\vec{\omega}_n|)$. To obtain the line shape in the HOMOGENIZED spectrum, the DDF-signal must be integrated over all r_n . In Fig. 3.5, this was approximated by summing up the Fourier-transforms of these contributions in $0.5 \text{ }\mu\text{m}$ steps. The result is a single line, which is only broadened by inhomogeneities on a $100 \text{ }\mu\text{m}$ scale (solid peak in the inset). Line shapes in iZQC spectra are thus insensitive towards long-range (on a mm scale) distortions of the magnetic field.

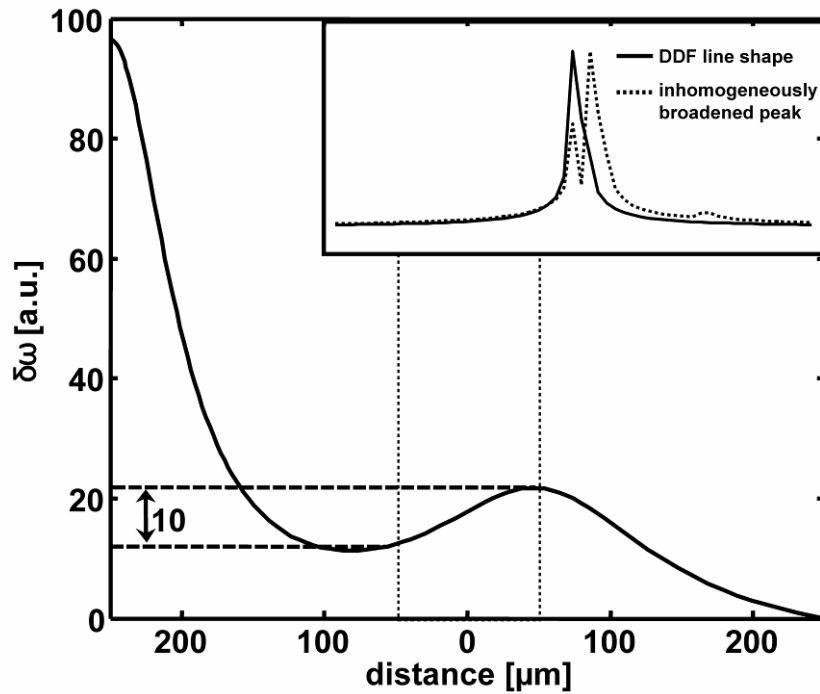


Figure 3.5: Schematic illustration of the principle of resolution enhancement in iZQC spectra. An arbitrary frequency profile is shown along the gradient modulation direction in a 0.5 mm voxel. Vertical dotted lines indicate the region of maximum signal contribution for the magnetization at the origin for $k_m = 100 \text{ mm}^{-1}$. Horizontal lines indicate that the frequency varies only by 10 units in this region. Inset: calculated line shapes for spectra acquired from this voxel with a standard sequence (dotted curve) and with HOMOGENIZED (solid curve). The former was calculated by Fourier transforming a simulated FID of one second duration over the whole voxel, $\sum_r \exp[i\tau\delta\omega(r)]$. The latter was obtained by calculating Fourier transforms over regions of major signal contribution ($100 \text{ }\mu\text{m}$) in $0.5 \text{ }\mu\text{m}$ steps, and subsequently summing up the results.

3.4 Signal evolution and spectral analysis

Before calculating signal evolution, one has to recognize that all spin species in the sample provide a DDF, each influencing all magnetization vectors. However, concentrations of

metabolites *in vivo* are usually small compared to water and the DDF of metabolite spins can therefore be neglected. I will in the following analyse signal evolution for a two-spin system, taking into account the DDF of both species. The treatment can easily be extended to more spin species. For inequivalent spins of the same nuclear species with large chemical shift difference ($\Delta\omega_{cs} \gg \omega_d$), the heteronuclear treatment applies (49). Signal evolution is derived from the modified Bloch equation including the DDF:

$$\begin{aligned} dM^+(s)/dt_2 = & \gamma M^{I+}(s) \left[B_{DDF}^I(s) + \frac{2}{3} B_{DDF}^S(s) + \gamma^{-1} \Delta\omega_I \right] \\ & + \gamma M^{S+}(s) \left[B_{DDF}^S(s) + \frac{2}{3} B_{DDF}^I(s) + \gamma^{-1} \Delta\omega_S \right], \end{aligned} \quad [3.17]$$

where $\gamma_I = \gamma_S = \gamma$. $B_{DDF}^{I,S}(s)$ are the z-components of $\vec{B}_{DDF}^{I,S}(s)$, since Larmor precession averages out the transverse components of $\vec{B}_{DDF}^{I,S}(s)$ to first order. The factors 2/3 in Eq. [3.17] appear only for the DDFs acting on unlike spin magnetization, because, for example

$$\vec{M}^S \times \vec{B}_{DDF}^I = \mu_0 \vec{M}^S \times \left(M_z^I - \vec{M}^I/3 \right) = \frac{\mu_0}{3} \vec{M}^S \times \left[3M_z^I - \begin{pmatrix} M_x^I \\ M_y^I \\ M_z^I \end{pmatrix} \right] = \frac{\mu_0}{3} \vec{M}^S \times \begin{pmatrix} -M_x^I \\ -M_y^I \\ 2M_z^I \end{pmatrix}. \quad [3.18]$$

Thus, the term which describes the effect of $B_{DDF}^I(s)$ on the transverse magnetization of S spins is $\frac{2}{3} M^{S+} M_z^I$. For equivalent spins, the effect of $B_{DDF}^I(s)$ depends on $M^{I+} M_z^I$, because $\vec{M}^I \times \vec{M}^I = 0$. The solution of Eq. [3.17] describes precession under chemical shift, gradients, and the DDF (78) (see Appendix A for full derivation):

$$M^+(t_2) =$$

$$(A) \ i \cos \beta M_0^I e^{i\Delta\omega_I t_2} J_1(-\sin \beta t_2/\tau_{dl}) J_0(-\sin \beta \frac{2}{3} t_2/\tau_{ds})$$

$$(B) \ +i \cos \beta M_0^S e^{i\Delta\omega_S t_2} J_1(-\sin \beta t_2/\tau_{ds}) J_0(-\sin \beta \frac{2}{3} t_2/\tau_{dl})$$

$$(C) \ +i M_0^I e^{i\Delta\omega_I t_2} e^{i(\Delta\omega_I - \Delta\omega_S) t_1} \times \left[\cos \beta J_2(-\sin \beta t_2/\tau_{dl}) - \frac{1 - \cos \beta}{\sin \beta} \frac{\tau_{dl}}{t_2} J_1(-\sin \beta t_2/\tau_{dl}) \right] J_1(-\sin \beta \frac{2}{3} t_2/\tau_{ds})$$

$$(D) \ +i M_0^S e^{i\Delta\omega_S t_2} e^{i(\Delta\omega_I - \Delta\omega_S) t_1} \times \left[\cos \beta J_2(-\sin \beta t_2/\tau_{ds}) - \frac{1 - \cos \beta}{\sin \beta} \frac{\tau_{ds}}{t_2} J_1(-\sin \beta t_2/\tau_{ds}) \right] J_1(-\sin \beta \frac{2}{3} t_2/\tau_{dl})$$

$$(E) \ -i M_0^I e^{i\Delta\omega_I t_2} e^{i(\Delta\omega_S - \Delta\omega_I) t_1} \times \left[\cos \beta J_0(-\sin \beta t_2/\tau_{dl}) - \frac{1 - \cos \beta}{\sin \beta} \frac{\tau_{dl}}{t_2} J_1(-\sin \beta t_2/\tau_{dl}) \right] J_1(-\sin \beta \frac{2}{3} t_2/\tau_{ds})$$

$$(F) \quad -iM_0^S e^{i\Delta\omega_S t_2} e^{i(\Delta\omega_S - \Delta\omega_I) t_1} \times \left[\cos \beta J_0 \left(-\sin \beta t_2 / \tau_{ds} \right) - \frac{1 - \cos \beta}{\sin \beta} \frac{\tau_{ds}}{t_2} J_1 \left(-\sin \beta t_2 / \tau_{ds} \right) \right] J_1 \left(-\sin \beta \frac{2}{3} t_2 / \tau_{dl} \right), \quad [3.19]$$

where $\tau_{dl,S} = (\gamma \mu_0 M_0^{I,S})^{-1}$. The (A) component of Eq. [3.19] relative to the equilibrium magnetization at 750 MHz is plotted in Fig. 3.6 for $\beta = 45^\circ$ and different Larmor-frequencies. The DDF-signal intensity reaches in the best case only 40% of M_0 . Note the unusual shape of the DDF-signal, which follows a Bessel-function and includes a particular build-up period. This slow signal increase can cause serious problems in experiments where SNR is critical. However, as Fig. 3.6 demonstrates, increasing the magnetic field strength brings an increase in both maximum intensity and build-up speed of the DDF-signal.

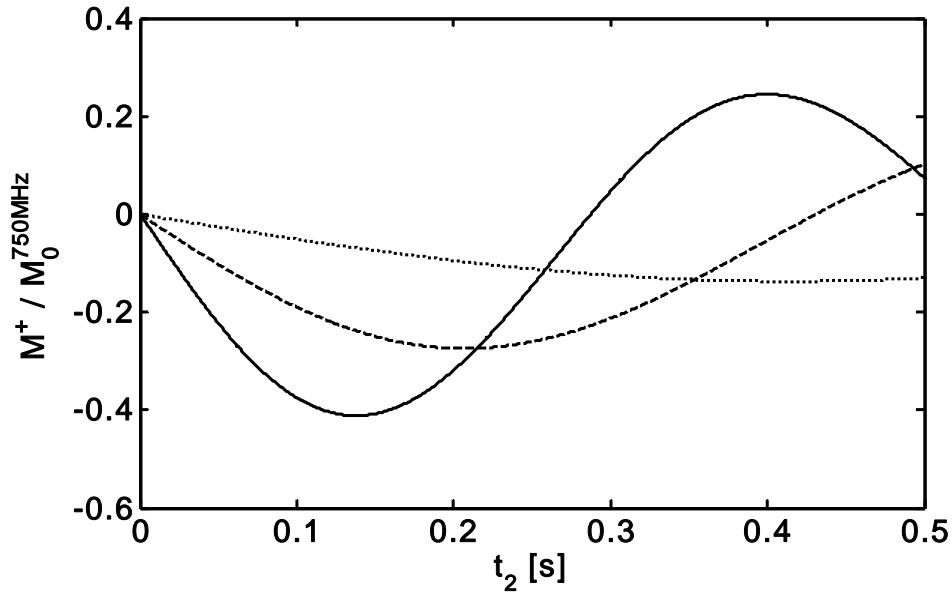


Figure 3.6: Evolution in the detection period of the DDF-signal component producing a homonuclear water peak (proton concentration $c = 110 \text{ M}$) for $\beta = 45^\circ$, $\Delta\omega_I = 0$ and $\omega_0 = 750 \text{ MHz}$ (solid), $\omega_0 = 500 \text{ MHz}$ (dashed) and $\omega_0 = 250 \text{ MHz}$ (dotted) (Eq. [3.19] (A)). Notice the characteristic build-up and that higher field strength not just increases the maximum intensity, but also shortens the build-up time.

A 2D HOMOGENIZED spectrum with six peaks (corresponding to terms A-F in Eq. [3.19]) is obtained after Fourier transformation of the time domain data along the t_1 and t_2 axes. This result is in accordance to the one found with the quantum treatment (Sec. 3.1). Typical HOMOGENIZED spectra for a two component system, acquired in a water–acetone mixture are shown in Fig. 3.7. Along the indirect dimension ω_1 , peaks are separated by their chemical shift difference, $\Delta\omega_{\text{acetone}} - \Delta\omega_{\text{water}}$.

The direct dimension ω_2 corresponds to the conventional 1D spectrum, which is distorted in inhomogeneous fields. The dominating axial peak in the spectrum acquired with $\beta = 45^\circ$ is the homonuclear water peak (A in Fig. 3.7a). The highest cross-peak (F) at $(\Delta\omega_{\text{acetone}} - \Delta\omega_{\text{water}}, \Delta\omega_{\text{acetone}})$ is formed by the methyl protons of acetone under the action of the strong DDF of the water spins. The second highest cross-peak (C) at $(\Delta\omega_{\text{water}} - \Delta\omega_{\text{acetone}}, \Delta\omega_{\text{water}})$ results from transverse water magnetization evolving in the DDF of acetone. The spectrum for $\beta = 90^\circ$ is presented in Fig. 3.7b. In this case the first two terms in Eq. [3.19], which correspond to the product operators in Eq. [3.12], vanish, predicting no peaks at axial positions. However, due to experimental imperfections and to relaxation, which has been neglected so far, residual

axial peaks are observed. Comparing Fig. 3.7b with Fig. 3.7a, the intensity of the axial peaks is strongly reduced for $\beta = 90^\circ$. For each spin species (water and acetone) both cross-peaks have the same intensities, which are lower than maximum intensities for $\beta = 45^\circ$ (peaks C and F in Fig. 3.7a).

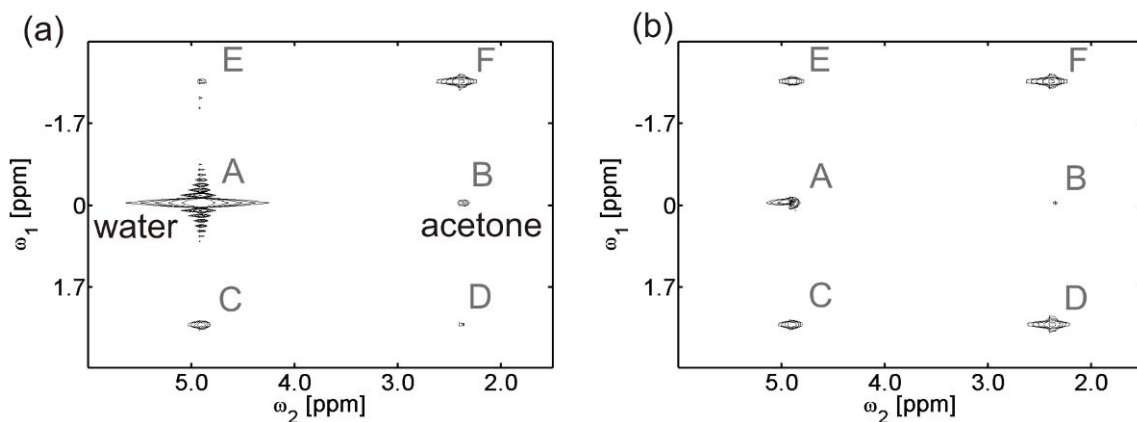


Figure 3.7: Spectral patterns in HOMOGENIZED of binary samples recorded with a water-acetone mixture (1/1 volume ratio) at 17.6 T. Peaks are labelled according to the terms in Eq. [3.19]. $TR/TE = 20.0/0.27$ s, $G = 200$ mT/m, $T = 1$ ms, $NA = 2$, phase of first RF-pulse $ph1 = (x, -x)$, other phases (x) . (a) Spectrum acquired with the original sequence with second RF-pulse $\beta = 45^\circ$. (b) Non-selective second pulse with $\beta = 90^\circ$. Axial peaks are strongly attenuated.

Figure 3.8 shows the evolution of the signal component F for $\beta = 45^\circ$ and 90° . For the $\beta = 45^\circ$ curve the maximum is higher, whereas the signal per unit time ratio is also better, which leaves us with the conclusion that HOMOGENIZED performs best with $\beta = 45^\circ$, as it was suggested in the original paper (27). However, this is only true for non selective β , and without considering relaxation effects.

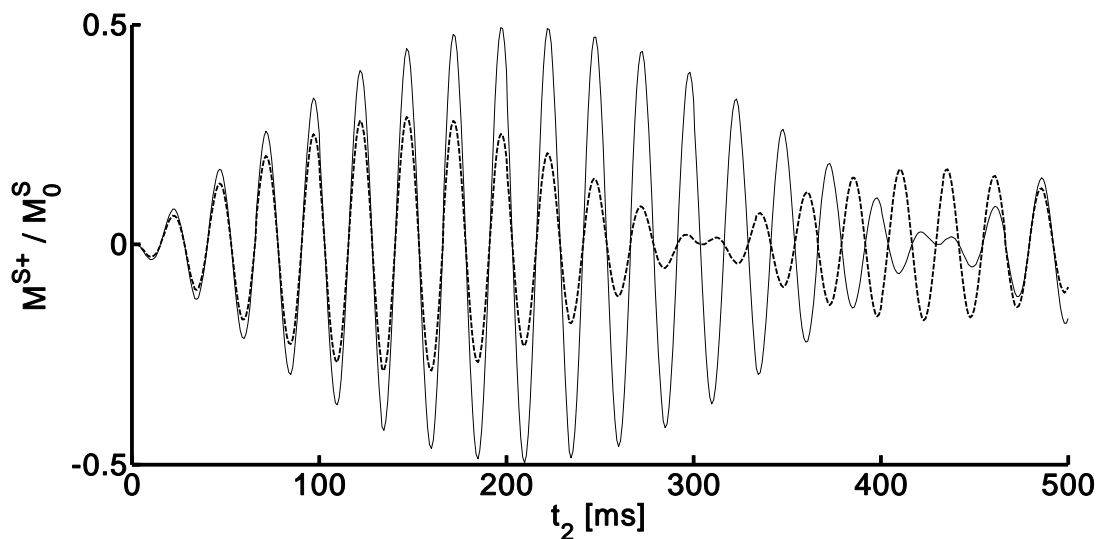


Figure 3.8: Evolution in the detection period of DDF-signal components producing the F cross-peak for $c_S = 0.1$ M S-spin concentration, $c_I = 110$ M, $\omega_0 = 750$ MHz and $\Delta\omega_S = -250$ Hz. Solid and shaded curves are time evolutions with $\beta = 45^\circ$ and $\beta = 90^\circ$, respectively.

4. Method development for *in vivo* iZQC-spectroscopy

HOMOGENIZED in its original form (Fig. 3.1) (27) was successfully applied in the rat brain *in vivo* (92). However, the sequence showed poor practicality caused by low SNR per unit time compared to standard MRS methods, by the water signal dominating metabolite information, and by the non-variable spatial origin of the iZQC-spectra. A throughout analysis and major improvements were necessary to develop a new, robust iZQC-sequence for *in vivo* applications.

4.1 Selective HOMOGENIZED (SEL-HOMOGENIZED)

It was recognized that application of the original sequence with a frequency selective $\beta = 90^\circ$ second pulse (Fig. 4.1) has major benefits. Selective HOMOGENIZED was analyzed and experimentally validated on several phantoms by our (37) and parallel to us by another research group (29), with similar outcome and conclusions. Chen and co-workers dubbed the sequence SEL-HOMOGENIZED.

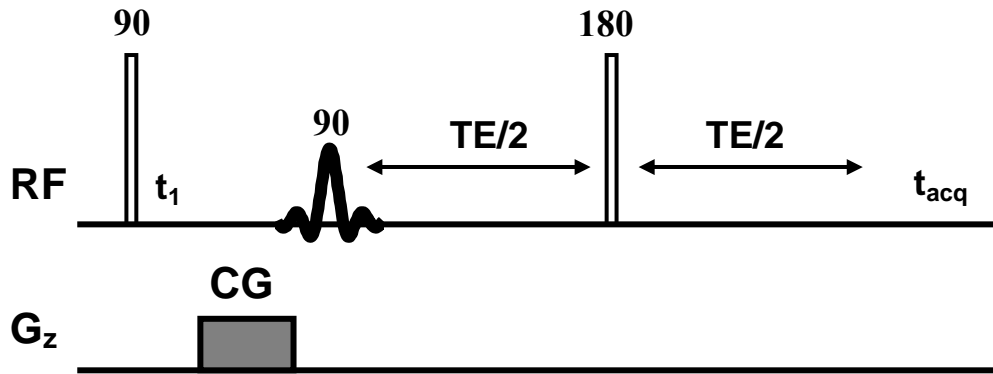


Figure 4.1: The SEL-HOMOGENIZED sequence. The second pulse is frequency selective.

4.1.1 Theoretical analysis of SEL-HOMOGENIZED

Generally, if $\beta = 90^\circ$, the coherence selection pathway of homonuclear iZQC ends exclusively in unobservable terms and Eq. [3.12] can be rewritten as

$$I_i^+ I_j^- + I_i^- I_j^+ \xrightarrow{\{I_x(90^\circ)\}} \text{unobservable terms} \xrightarrow{\text{dipolar couplings, } \{D_{ij} I_{zi} I_{zj}\}} \text{no signal} \quad [4.1]$$

In aqueous solutions this effect leads to suppression of the axial water-peak. For P and N-type heteronuclear iZQC in case of $\beta = 90^\circ$, Eqs. [3.13] and [3.14] change into

$$I^+ S^- (\Delta\omega_I - \Delta\omega_S) \xrightarrow{\{I_x(90^\circ), S_x(90^\circ)\}} iI_x S_z - iI_z S_x + \text{unobservable terms} \\ \xrightarrow{\text{dipolar couplings, } \{D_{ik} I_{zi} S_{zk}\}} \frac{1}{2} (-iI_y + iS_y) = \frac{1}{4} [(I^- - I^+) + (S^+ - S^-)]$$

$$\xrightarrow{\{I_x(180^\circ), S_x(180^\circ)\}} \xrightarrow{\text{chemical shift, } \{I_z(\Delta\omega_I), S_z(\Delta\omega_S)\}} \xrightarrow{\text{quadrature detection}} \frac{I^- - S^-}{2}, \quad [4.2]$$

and

$$\begin{aligned} I^- S^+ (\Delta\omega_S - \Delta\omega_I) &\xrightarrow{\{I_x(90^\circ), S_x(90^\circ)\}} -iI_x S_z + iI_z S_x + \text{unobservable terms} \\ &\xrightarrow{\text{dipolar couplings, } \{D_{Iz} S_z\}} \rightarrow \frac{1}{2} (iI_y - iS_y) = \frac{1}{4} [(I^+ - I^-) + (S^- - S^+)] \\ &\xrightarrow{\{I_x(180^\circ), S_x(180^\circ)\}} \xrightarrow{\text{chemical shift, } \{I_z(\Delta\omega_I), S_z(\Delta\omega_S)\}} \xrightarrow{\text{quadrature detection}} \frac{S^- - I^-}{2}. \end{aligned} \quad [4.3]$$

Here we abandoned the spin-indices *i* and *k* for the general condition that spins *I* and *S* are from different molecules. Furthermore, a new operation was introduced, based on the detection process of an NMR-hardware. Quadrature detection (QD) is not a basic NMR physical principle, but rather a hardware-bound operation. QD is the parallel acquisition of the FID on two separate receive channels. Subsequent mixing of the FIDs with a 90° phase shift results in the complex NMR-signal. This acquisition paradigm is convenient for Fourier-transform (FT) NMR, because the FT of a real (non complex) FID gives a spectrum with central symmetric pattern, but the information in a spectrum obtained through a complex FT is exactly defined, without redundancy and overlapping. Suppose that the coil is aligned along the *x*-axis of the laboratory frame. In this case we observe the *x*-component of the magnetization:

$$M_x \sim \langle \hat{I}_x \rangle = \text{Tr} \{ \hat{\rho} \hat{I}_x \} \sim \rho^- + \rho^+, \quad [4.4]$$

where ρ^- and ρ^+ are (± 1)-quantum coherences (e.g. I^- and I^+). If we change now to the rotating frame (see Sec. 2.5) the signal detected on a single channel is proportional to

$$S(t) \sim \frac{1}{2} i \tilde{\rho}^-(t) e^{-i\phi_{\text{rec}}} - \frac{1}{2} i \tilde{\rho}^+(t) e^{i\phi_{\text{rec}}}, \quad [4.5]$$

where \sim marks rotating frame coherences and Φ_{rec} is the signal phase shift by the receiver. In QD-modus only (-1)-quantum or (+1)-quantum coherences will be detected (93). The 750MHz Bruker spectrometer used for most experiments in this work detects (-1)-quantum coherences, and the combined signal of the two channels is proportional to

$$S(t) \sim i \tilde{\rho}^-(t) e^{-i\phi_{\text{rec}}}. \quad [4.6]$$

Therefore, Eqs. [4.2] and [4.3] end with sums of I^- and S^- coherences. Equation [4.6] also shows that QD brings a factor of two in intensity benefit relative to single channel acquisition, because of averaging the two phase shifted signals (see again the last step in Eqs. [4.2] and [4.3]).

For a $\beta = 90^\circ$ pulse selecting the *I* spin resonance frequency, the intensity of the P-type cross-peak created by the *S* spin magnetization is further doubled in comparison with the result in Eq. [4.3] (peak *F'* in Fig. 4.2). Moreover, the theory predicts no further peaks if diffusion and relaxation effects are neglected:

$$\begin{aligned} I^+ S^- (\Delta\omega_I - \Delta\omega_S) &\xrightarrow{\{I_x(90^\circ)\}} -iI_z S_x - I_z S_y + \text{unobservable terms} \\ &\xrightarrow{\text{dipolar couplings, } \{D_{Ik} I_{zi} S_{zk}\}} \rightarrow \frac{1}{2} (iS_y - S_x) = -\frac{1}{2} S^- \end{aligned}$$

$$\xrightarrow{\{S_x(180^\circ)\}} \xrightarrow{\text{chemical shift, } \{S_z(\Delta\omega_S)\}} \xrightarrow{\text{quadrature detection}} 0, \quad [4.7]$$

and

$$\begin{aligned} I^- S^+ (\Delta\omega_S - \Delta\omega_I) &\xrightarrow{\{I_x(90^\circ)\}} iI_z S_x - I_z S_y + \text{unobservable terms} \\ &\xrightarrow{\text{dipolar couplings, } \{D_{I_z S_z}\}} \rightarrow \frac{1}{2}(-iS_y - S_x) = -\frac{1}{2}S^+ \\ &\xrightarrow{\{S_x(180^\circ)\}} \xrightarrow{\text{chemical shift, } \{S_z(\Delta\omega_S)\}} \xrightarrow{\text{quadrature detection}} -S^-. \end{aligned} \quad [4.8]$$

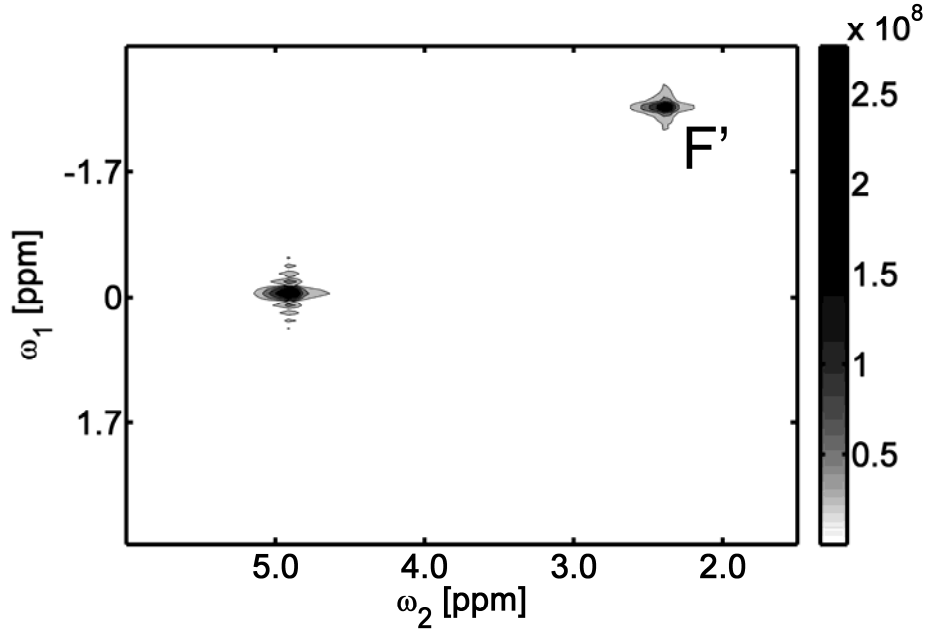


Figure 4.2: Spectrum of the same phantom as used for the acquisition of spectra in Fig. 3.7, registered using the sequence in Fig. 4.1 with a β -pulse selecting the water resonance. $TR/TE = 20.0/0.27$ s, $G = 200$ mT/m, $T = 1$ ms, $NA = 2$, phase of first RF-pulse $ph1 = (x, -x)$, other phases (x) . The peak predicted by the theory (Eqs. [4.8-9]) is labelled. Scale bar in arbitrary intensity units.

Again, for a more detailed treatment it is worth switching from the quantum mechanical framework to the classical analysis. If the second pulse is frequency selective, only the selected spin species contributes to the DDF. For a selective pulse on the I spins with $\beta = 90^\circ$, all S spins remain transverse and maximum DDF from the I spins is produced. The solution of Eq. [3.17] gets greatly simplified, and following the derivation steps presented in Appendix B, the result

$$M^+(t_2) = iM_0^S e^{i\Delta\omega_S t_2} e^{i(\Delta\omega_S - \Delta\omega_I)t_1} J_1\left(-\frac{2}{3}t_2/\tau_{dl}\right) \quad [4.9]$$

is obtained (37). Similarly to the result of the quantum treatment in Eqs. [4.7] and [4.8], only one peak is expected at $(\Delta\omega_S - \Delta\omega_I, \Delta\omega_S)$ in the spectrum. However, the spectrum shown in Fig. 4.2 shows an additional peak at the position $(0, \Delta\omega_I)$. This has multiple reasons: on one hand it is caused by the T_1 -relaxation during t_1 (see Appendix C), on the other hand by experimental imperfections, like an inhomogeneous B_1 -profile of the RF-coil causing pulse imperfections, or a not overall strong enough CG causing imperfect dephasing of SQCs.

Equation [4.9] describes a faster signal build-up and doubled cross-peak intensity compared to Eq. [3.19] with $\beta = 90^\circ$. This is demonstrated in Fig. 4.3, where the function in Eq. [4.9] is plotted along with the (F) term in Eq. [3.19] for $\beta = 90^\circ$ and $\beta = 45^\circ$. At a magnetic field

strength of 17.6 T, the DDF-signal for a selective β reaches a maximum of 58 % of the equilibrium magnetization after 147 ms. Global β cannot produce signal higher than 50 % of M_0 , reached for $\beta = 45^\circ$ after 208 ms.

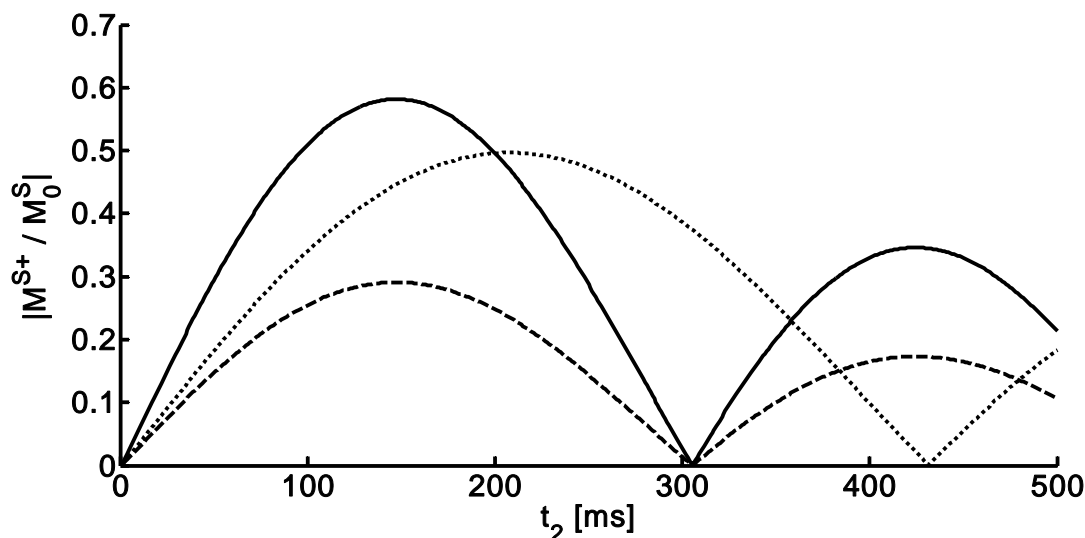


Figure 4.3: Theoretical evolution envelopes of the absolute value DDF-signal for the HOMOGENIZED sequence with different β -pulses: $\beta = 90^\circ$ selecting the I spins (solid curve), $\beta = 90^\circ$ non selective (dashed curve), and $\beta = 45^\circ$ non selective (dotted curve). Concentrations $c_I = 110$ M and $c_S = 0.1$ M, and $\omega_0 = 750$ MHz. Note that the signal reaches maximum intensity and the build-up is the fastest for the selective β .

The advantages of using a selective $\beta = 90^\circ$ pulse can be summarized as follows:

1. Maximum DDF is created resulting in the fastest possible signal build up. Losses caused by transverse relaxation (as it will be discussed later) are minimized.
2. The spectrum is edited by the exclusive action of the DDF of the selected component.
3. Cross-peak intensities are enhanced compared to an experiment with a non-selective β pulse.
4. Axial peaks are strongly suppressed, acting as an intrinsic solvent suppression.

Applications of the selective $\beta = 90^\circ$ pulse were found not just for iZQC-spectroscopy. A sequence called IDEAL (Intermolecular Dipolar-Interaction Enhanced All Lines) and their derivatives detect iDQCs (94,95). And solvent localized spectroscopy (SOLO) can selectively detect spectra in different sample compartments without single voxel localization if the solvents have different chemical shifts (96).

4.1.2 Optimal acquisition window for SEL-HOMOGENIZED

In particular under *in vivo* conditions, relaxation and diffusion effects have to be taken into account for the evaluation of signal evolution in iZQC experiments. After introduction of longitudinal and transverse relaxation terms in Eq. [3.17] a solution can be found (see Appendix C) (29,37,55,62):

$$M^+(t_2) = iM_0^S e^{i\Delta\omega_S t_2} e^{i(\Delta\omega_S - \Delta\omega_I)t_1} e^{-(t_1+t_2)/T_2^S} J_1 \left(-\frac{2}{3} \frac{\Delta_S}{\tau_{df}} e^{-t_1/T_1^I} (1 - e^{-t_2/T_1^I}) T_1^I \right), \quad [4.10]$$

where $T_{1,2}^{I,S}$ are longitudinal and transverse relaxation times of spins I and S, respectively.

Figure 4.4 illustrates the effect of relaxation for estimated *in vivo* time constants on the theoretical brain metabolite signal evolution. Equation [4.10] (solid lines) is compared with the solution neglecting relaxation (dotted line, Eq. [4.9]) and the exponential signal decay in a conventional 1D experiment (dashed lines). The damped SEL-HOMOGENIZED signal reaches a dramatically lower maximum intensity after shorter evolution time. Amplitude and position of the maximum strongly depend on T_2 of the detected spin species. For a shorter T_2 (grey lines) only slightly more than 10 % of M_0 will be detectable with SEL-HOMOGENIZED. Careful choice of the timing for the acquisition window is therefore pivotal for successful iZQC spectroscopy *in vivo*. The transverse metabolite relaxation times *in vivo* in the mouse brain at 17.6 T are reported to be 206 ± 51 ms for N-acetyl-aspartate, 160 ± 14 ms for creatine, 222 ± 56 ms for choline and 191 ± 21 ms for taurine (97). At 11.7 T the T_2 of the first three metabolites in the living rat brain are 285 ± 26 ms, 159 ± 7 ms, 366 ± 73 ms, respectively (98). The differences in the T_2 -values are most likely caused by the field strength and not by the animal model. Therefore, the optimum acquisition window for *in vivo* SEL-HOMOGENIZED experiments in the rodent brain at field strengths above 10 Tesla, can be coarsely estimated with the help of Fig. 4.4 and the above mentioned T_2 -values to the time interval between 50 ms (approximately the end of the initial linear signal build-up) and 250 ms (where the signal intensity begins to fall below the value at 50 ms) after the β pulse.

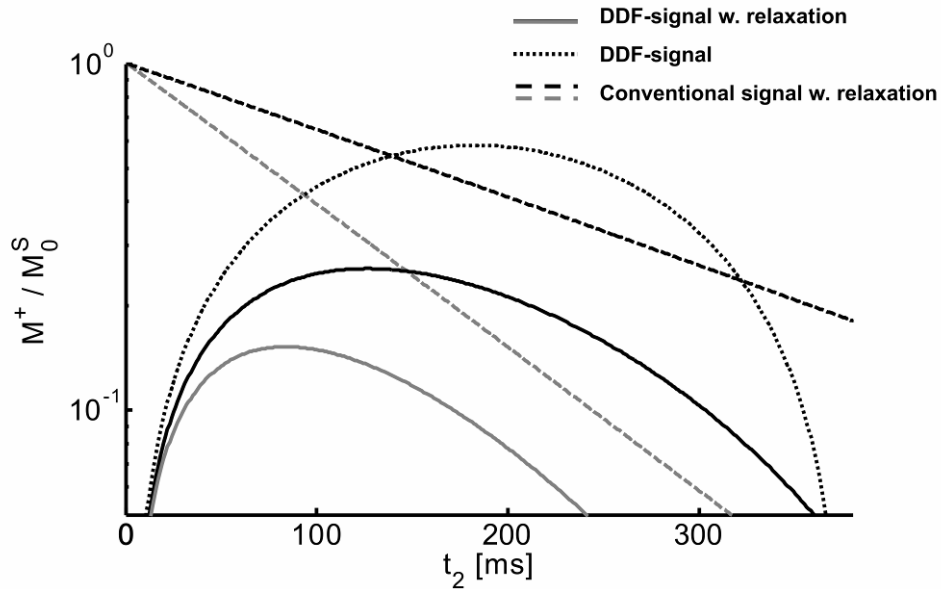


Figure 4.4: Theoretical signal evolution of a singlet brain metabolite resonance ($c_S = 10$ mM) on a logarithmic scale. For comparison, the relaxation decay of transverse magnetization is shown (dashed curves). The DDF-signal without relaxation calculated with Eq. [4.9] is shown as dotted curve. Attenuated DDF-signals (Eq. [4.10]) demonstrate the dramatic effect of relaxation on signal intensity (solid curves). The adequate positioning of the acquisition window in the detection period is therefore crucial. Most efficient signal detection is performed after the steep linear rise. For the calculation, brain tissue water concentration was set to 44.4 M (99), $T_{1\text{water}}$ to 1.8 s, $T_{1\text{metabolite}}$ to 1.6 s (100), and transverse relaxation times to $T_{2\text{water}} = 0.03$ s (98), $T_{2\text{metabolite}} = 0.2$ s and 0.1 s for the black and grey curves, respectively.

The effect of diffusion on the DDF-signal has been approached repeatedly, but is still not fully understood (55,58,61,63,65,66,71-74,101-104). Results of numerical simulations backed by experimental verification performed with a dimethyl-sulfoxide phantom at 400 MHz (66) lead to the conclusion that for low k_m -values (16 mm^{-1}), meaning large gradient modulation periods and reduced diffusive attenuation, Eq.[4.10] provides an acceptable approximation for iZQC-signal evolution. In the case of a stronger diffusive attenuation, for $k_m = 62 \text{ mm}^{-1}$ and fast gradient modulation, iZQC-signal evolution does not follow a Bessel-function, so that after the linear build-up the signal falls with an exponential relaxation decay. Therefore, the effect of diffusion can override the nonlinear spin dynamics caused by the dipolar interactions and, surprisingly, prolong the DDF-signal envelope. However, *in vivo* iZQC experiments can probably not profit from this benefit because diffusion further decreases the maximum achievable DDF-signal intensity and transverse relaxation attenuates the signal to the noise level before any significant difference caused by diffusion could manifest itself (see the discussion about the optimal acquisition window above).

4.1.3 Experimental evaluation of SEL-HOMOGENIZED

4.1.3.1 MATERIALS AND METHODS

To evaluate the signal enhancement and the water suppression efficiency of a SEL-HOMOGENIZED sequence, experiments on a 90% H₂O / 10% D₂O (vol/vol) sample with 1 mM creatine were performed on a Bruker DRX400 spectrometer with a 5 mm broadband X-observe probe-head. Theoretical signal evolutions as described by Eq. [4.10] and the modified Eqs. [3.19] including relaxation effects with the same parameters as used in experiments were calculated. To this end, the longitudinal relaxation time for creatine was measured with an inversion recovery experiment consisting of a 180° - TI - 90° sequence repeated for multiple inversion times (TI), which resulted in a T_1 of 2.56 s for the methyl, and 1.82 s for the ethyl group of creatine. Transverse relaxation times were measured with a series of spin echo experiments (90° - TE/2 - 180° - TE/2), where TE was varied, and a series of CPMG experiments (90° - [δ - 180° - δ]_n) (105,106), where the loop counter n was varied and the delay δ was kept in the range of a few milliseconds. Both experiments were performed with selective excitation for water suppression and resulted in average T_2 -values of 0.95 s for the methyl, and 0.65 s for the ethyl group of creatine, respectively. The relaxation times of water were not measured due to strong radiation damping. Therefore, the values for the signal calculations were set to the arbitrary values $T_1^I = 2 \text{ s}$, $T_2^I = 1 \text{ s}$, for the solvent spins, and to the measured values $T_1^S = 2.56 \text{ s}$, $T_2^S = 0.95 \text{ s}$, for the solute spins. The demagnetizing time τ_d in the calculations was set to 0.1 s for the I spins and to 6000 s for the low concentration S spins. The value of t_1 was 2 ms. For the comparison of relative peak ratios, peak intensities were calculated by integration over ellipsoid areas around the peak maximum. SNR in a magnitude spectrum was calculated with the formula: $\frac{\max(\text{Signal} - \text{Noise})}{\text{std}(\text{Noise} - \text{Noise})}$, where the line on top denotes the mean intensity value.

4.1.3.2 RESULTS

Experimental HOMOGENIZED spectra acquired with non selective $\beta = 45^\circ$ and $\beta = 90^\circ$, as well as selective $\beta = 90^\circ$ are presented in Fig. 4.5. Table 4.1 shows the SNR values of the A

and F peaks relative to the minimum SNRs. Most efficient water suppression, as well as best signal-to-noise ratio was found in the spectrum with a selective pulse (Fig. 4.5c).

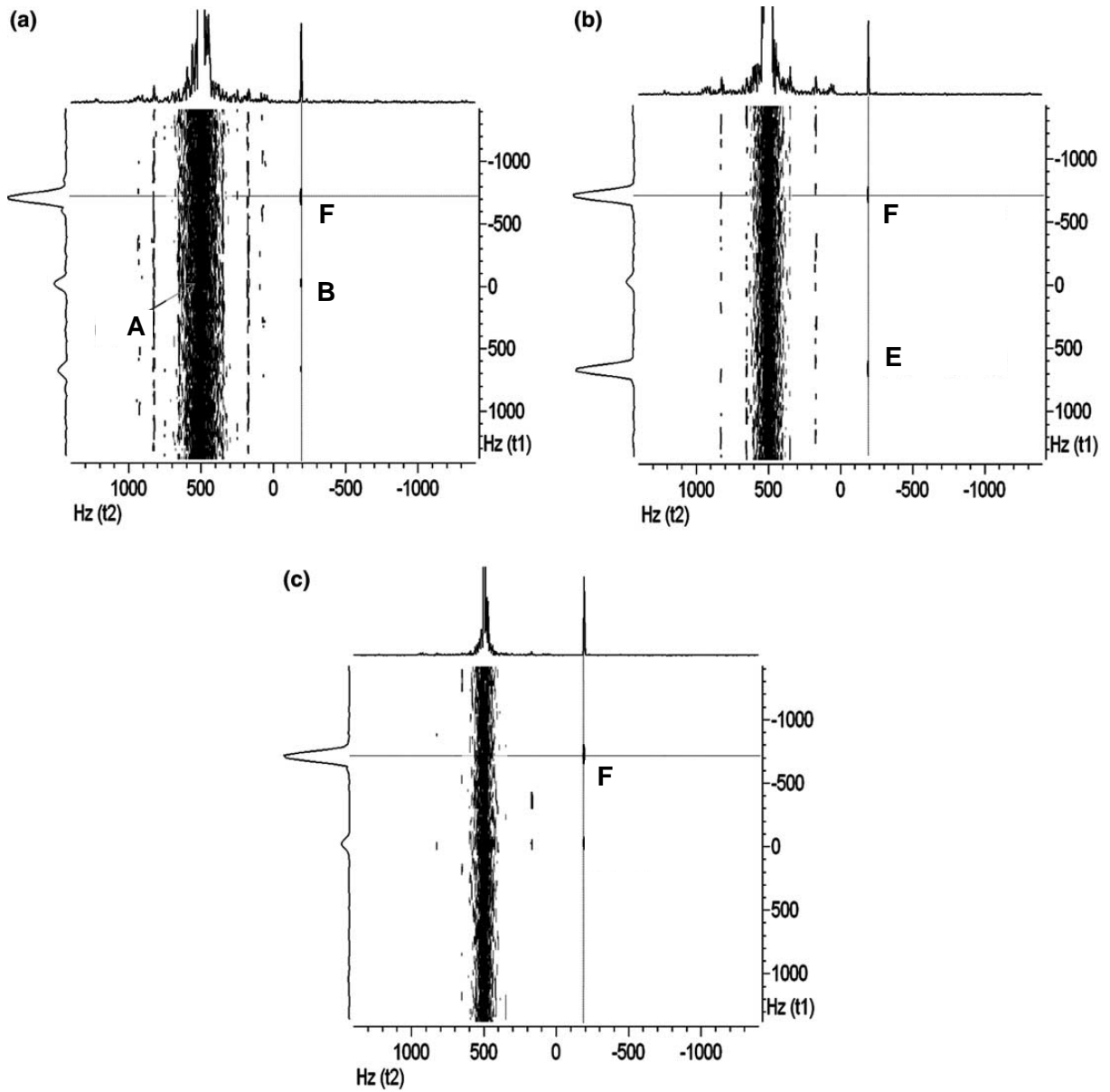


Figure 4.5: HOMOGEnIZED spectra of a 1 mM creatine solution. (a) $\beta = 45^\circ$, (b) $\beta = 90^\circ$, (c) $\beta = 90^\circ$ selective. To avoid radiation damping effects CG was split into two sections, as suggested in (42), and the first part was applied immediately after the first pulse. The effective strength of the sine-shaped CG was 14 G/cm applied for 1 ms. Gauss-shaped selective RF-pulses with a duration of 10 ms were applied, 64 t_1 increments were acquired, the acquisition window after an echo time of $TE = 190$ ms was $t_{acq} = 638$ ms long. $TR = 5$ s and the offset frequency of the receiver was -500 Hz. Raw data were zero-filled in both dimensions by a factor of 2. Quadratic sine bell apodization was used in both dimensions. Spectra are shown in magnitude mode. Rows and columns for the cross-peaks of the methyl group of creatine are indicated.

Table 4.1: Relative SNR of important peaks in spectra presented in Fig. 4.5

	$\beta = 45^\circ$	$\beta = 90^\circ$	SEL-HOMOGEnIZED
A-peak	1.6	2.2	1
F-peak	1	1.5	4.3

The calculated signal evolution curves as described by Eq. [4.10] and the modified Eqs. [3.19] are shown in Fig. 4.6. The relative maximum signal intensity ratio of these curves perfectly describes the experimental observations. Thus, transverse relaxation has dramatic effect on the DDF-signal intensity, which under these conditions is smallest for $\beta = 45^\circ$ both in theory (blue curve in Fig 4.6) and practice (Fig. 4.5a).

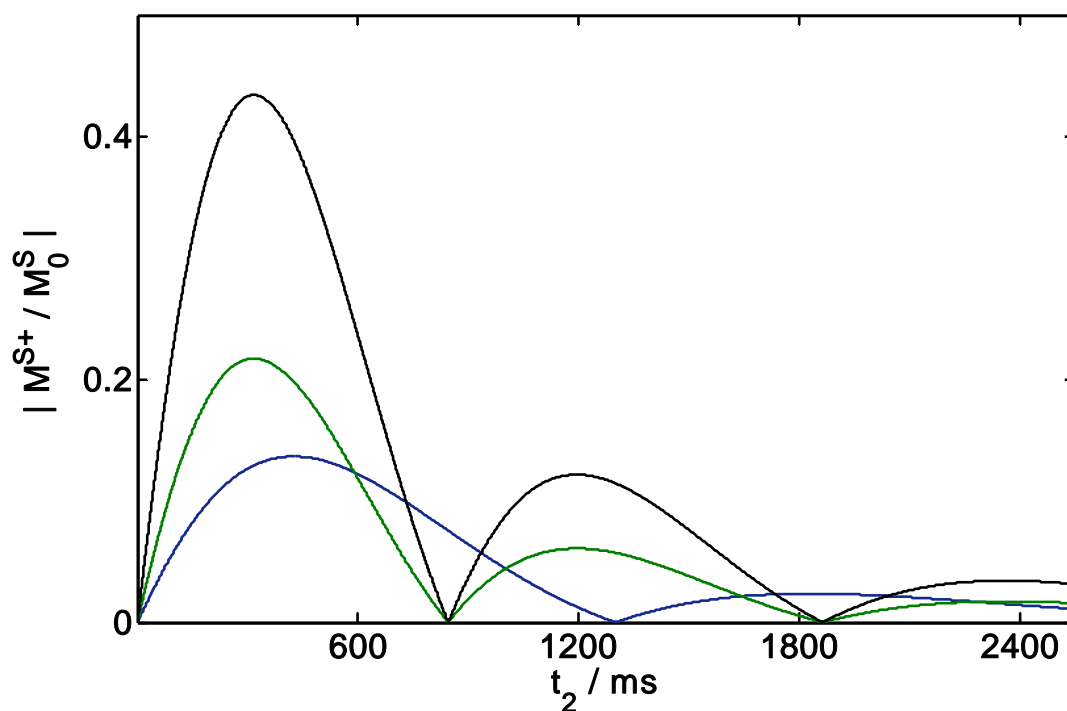


Figure 4.6: Theoretical evolution of the DDF-signal amplitude in the t_2 interval. Blue – (F) term in the modified Eq. [3.19] with $\beta = 45^\circ$, green – (F) term in the modified Eq. [3.19] with $\beta = 90^\circ$, black – Eq. [4.10].

4.2 Water suppression (WS)

4.2.1 Optimization of WS efficiency at a high-resolution 9.4 T NMR spectrometer

The application of a selective pulse with $\beta = 90^\circ$ alone does not eliminate the axial water peak (Fig. 4.2) (37). Additional WS methods can only be applied if they have no influence on the DDF. Presaturation and selective excitation techniques result in the elimination of transverse water magnetization prior to the second pulse. As a consequence, no DDF from water magnetization is created and DDF-signal build-up is impeded. Selective refocusing combined with gradient spoiling (WS module) applied in the detection period suppresses residual water signal efficiently.

However, while for concentrated samples the solvent signal can be suppressed to the noise level by SEL-HOMOGENIZED (Fig. 4.7a), as demonstrated in (29), for millimolar concentrations the solvent suppression is no longer sufficient. Therefore, SEL-HOMOGENIZED as presented earlier in Fig. 4.1 was extended to include additional water

suppression modules (Fig 4.7b). Figure 4.8 shows four spectra where water suppression was achieved using slightly different sequences. The spectra demonstrate that even at these low concentrations high quality spectra can be obtained and that water suppression can be improved compared to the original HOMOGENIZED. The relative intensities of the cross-peak F and the axial peak A are shown in Table 4.2.

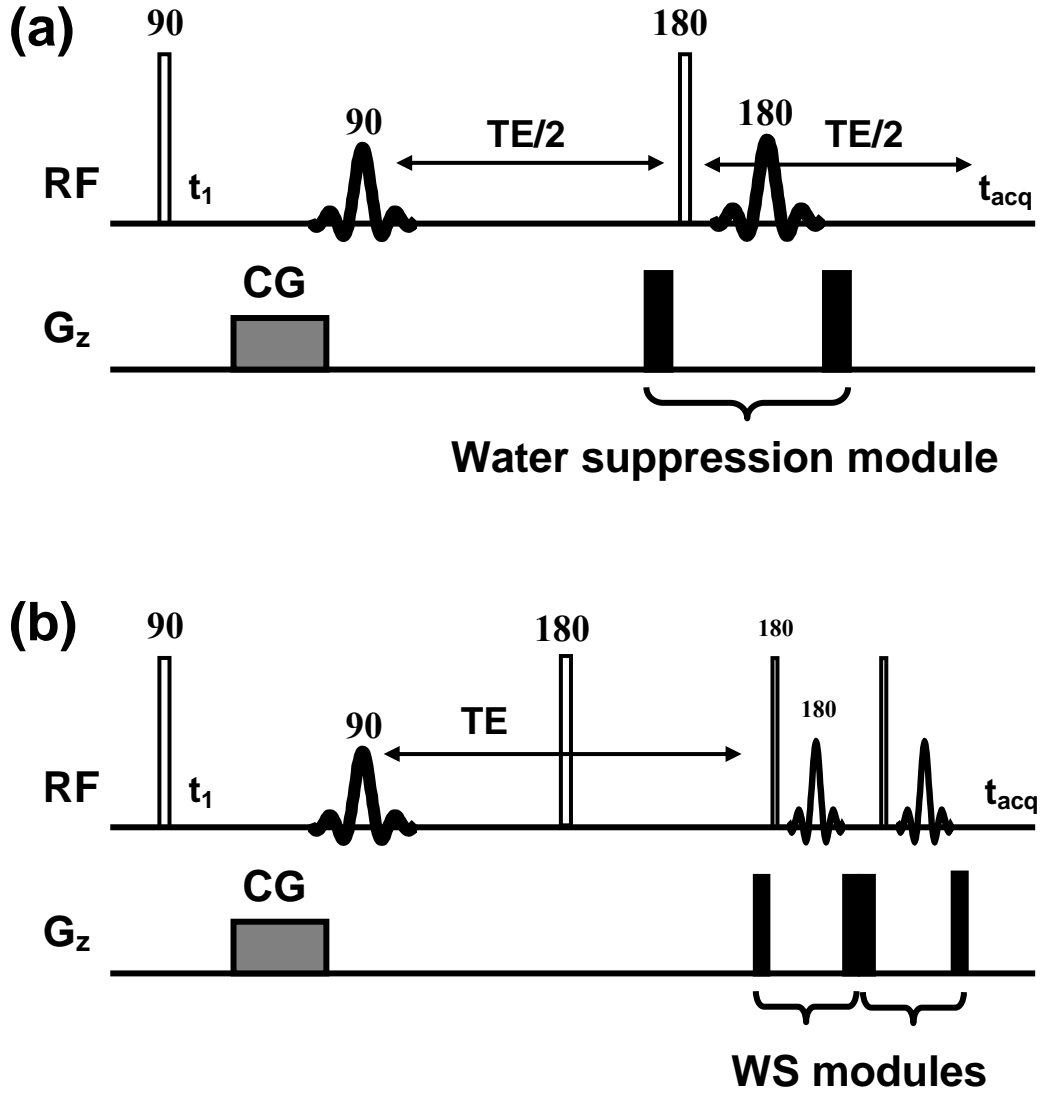


Figure 4.7: HOMOGENIZED pulse sequences with additional water suppression modules based on frequency selective refocusing. (a) SEL-HOMOGENIZED sequence as suggested by Chen et al. (29) with one WS module in the middle of the spin echo period replacing the 180° refocusing pulse. (b) SEL-HOMOGENIZED sequence with two WS modules immediately prior to the acquisition window, achieving the best water suppression efficiency in the study presented here.

Table 4.2: Relative ratios of peak intensities for the F cross-peak over the A axial peak, referenced to the ratio in the original HOMOGENIZED experiment

	Fig. 3.1	Fig. 4.1	Fig. 4.7a	Fig. 4.7b with only one WS module	Fig. 3.1 with two WS modules	Fig. 4.7b
F / A	1	8.1	1.1	2.5	6.5	13.5

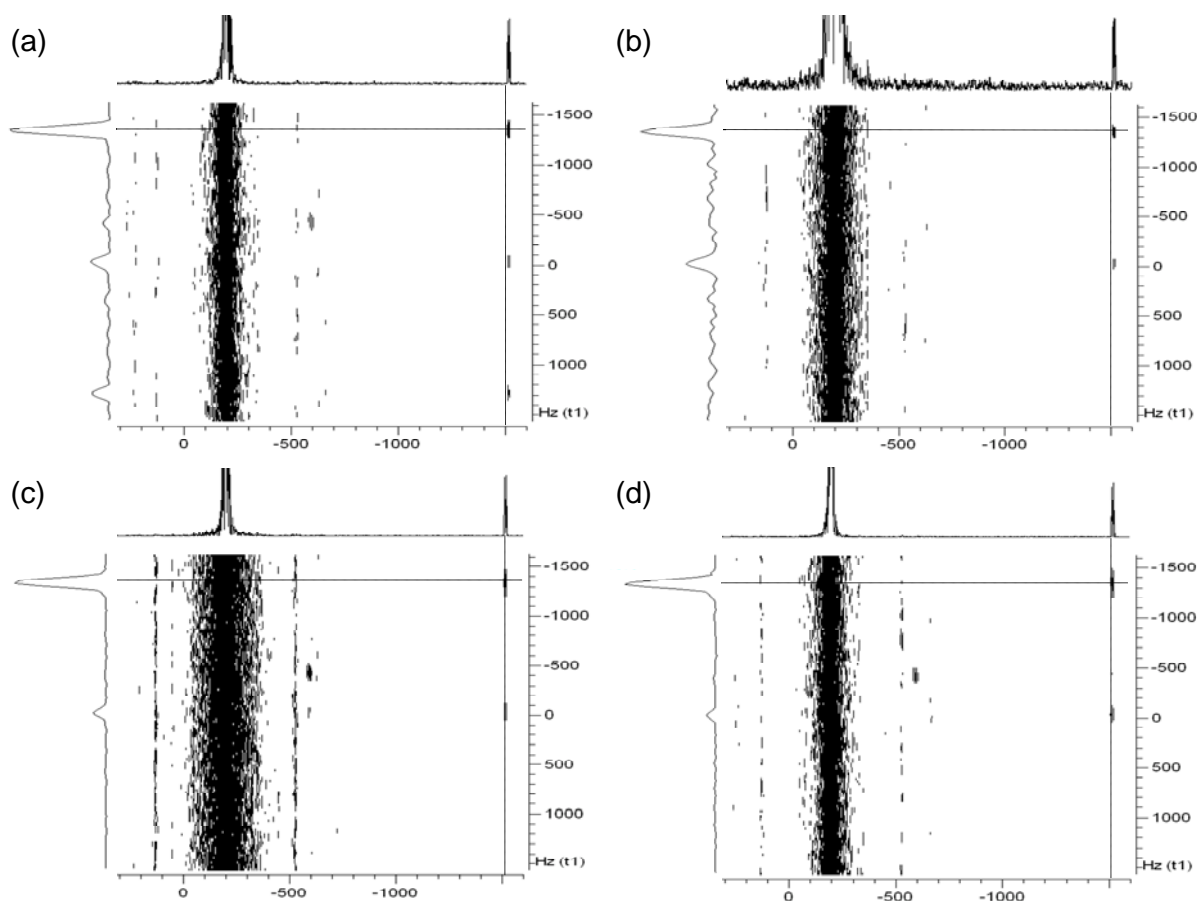


Figure 4.8: *HOMOGENIZED* spectra of a 3 mM alanine $\text{H}_2\text{O}/\text{D}_2\text{O}$ (9:1 v/v) solution with water suppression at 9.4 T. (a) pulse sequence as in Fig. 3.1, but with two additional WS-modules immediately before acquisition, (b) Chen's *SEL-HOMOGENIZED* as in Fig. 4.7a, (c) *SEL-HOMOGENIZED* as in Fig. 4.1, (d) the optimized method for water suppression in Fig. 4.7b. Experimental setup and processing steps were similar to that presented in the caption of Fig. 4.5, except for the acquisition time and for the offset frequency of the receiver, which were $t_{\text{acqu}} = 1275$ ms and 200 Hz, respectively.

Figure 4.8a shows a spectrum acquired with *HOMOGENIZED* ($\beta = 45^\circ$) in combination with two additional water suppression modules. Water suppression is improved by more than factor six compared to original *HOMOGENIZED*. Application of a selective mixing pulse alone (Fig. 4.1) results in a relative suppression of factor eight (Fig. 4.8c). Interestingly, the sequence in Fig. 4.7a (spectrum in Fig. 4.8b) is less efficient in terms of cross-peak intensity. As shown by Branca and Warren (107), this is due to a partial refocusing of the dipolar field interaction by the selective refocusing pulse employed for solvent suppression. Application of the suppression immediately before the acquisition minimizes these effects. Additionally, minor deviations from a pulse angle of 180° in the suppression modules, which is inevitable due to inhomogeneous B_1 -profiles even in high resolution probes, create longitudinal I magnetization that is sufficient to create iZQC-signal. If the concentration of the I spins is several orders of magnitude higher than that of the S spins, these effects can dominate the S signal. The most efficient water suppression was achieved as demonstrated by the spectrum in Fig. 4.8d with two suppression modules prior to the acquisition (Fig. 4.7b).

4.2.2 Water suppression at a 17.6 T small animal NMR microimager

The optimized sequence in Fig. 4.7b was also implemented on a 17.6 T small animal MR imager (37). The ratio between the residual water peak and the F' peak in the SEL-HOMOGENIZED spectrum from a water-acetone mixture (Fig. 4.2) was reduced after the application of two additional WS modules by a factor of 46 relative to the original HOMOGENIZED sequence (Fig. 4.9).

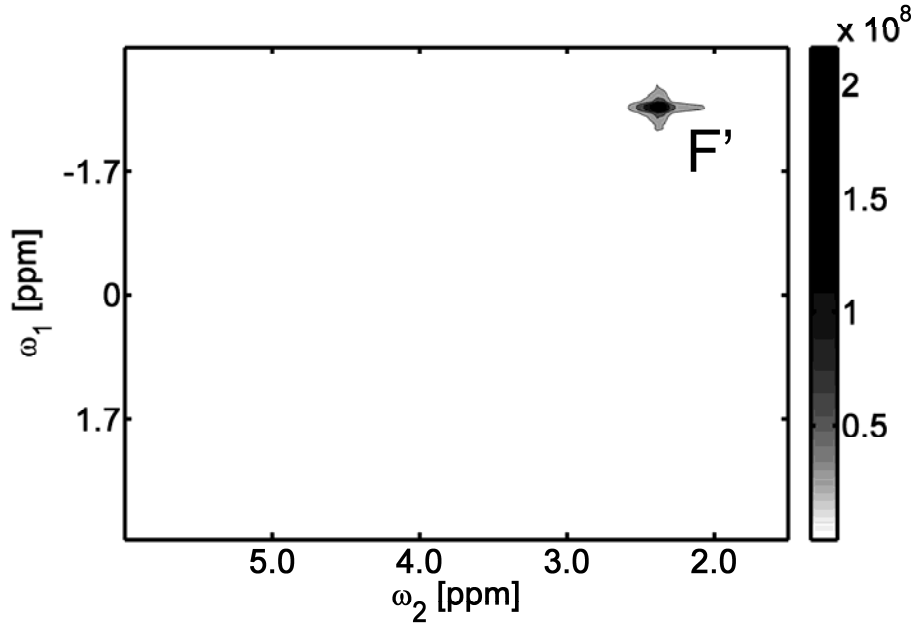


Figure 4.9: Spectrum of the same phantom as used for the acquisition of spectra in Fig. 3.7, with the pulse sequence presented in Fig. 4.7b. $TR/TE = 20.0/0.27$ s, $G = 200$ mT/m, $T = 1$ ms, $NA = 2$, phase of first RF-pulse $ph1 = (x, -x)$, other phases (x) . This result demonstrates the high efficiency of additional WS modules in solutions with components at high concentrations. Scale bar in arbitrary intensity units.

The efficiency of water suppression was verified also at lower solute concentrations. The spectra shown in Fig. 4.10 were acquired in two agar gel phantoms, each containing nine major brain metabolites at their typical *in vivo* concentrations (Table 4.3). In a homogeneous phantom twelve metabolite resonances were observed without water suppression (Fig. 4.10a). Application of two additional WS modules resulted in a suppression of the axial water peak by more than a factor of 140, which is clearly observable by comparing Fig. 4.10a and 4.10b. In the presence of strong magnetic field inhomogeneities, the efficiency of water suppression is lost. A second phantom with identical composition contained many randomly distributed air bubbles inducing strong field inhomogeneities. Resonance lines in the HOMOGENIZED spectrum are severely broadened in the direct dimension. Only seven resonances were observable (Fig. 4.10c). Under such large dispersion of resonance frequencies, application of additional WS modules was not efficient and compromised spectral quality even further (Fig. 4.10d). However, this problem is not specific for the iZQC method. In the proximity of air inclusions the selective refocusing effect of the WS modules broke down, because field variations in those regions were stronger than the effect of spoiler gradients. Thus, there is no difference in requirements for using water suppression modules in conventional MRS or iZQC spectroscopy. A minimum degree of field homogeneity is required in both cases. In real biological samples one can avoid large field variations and improve water suppression efficiency with the help of localization methods.

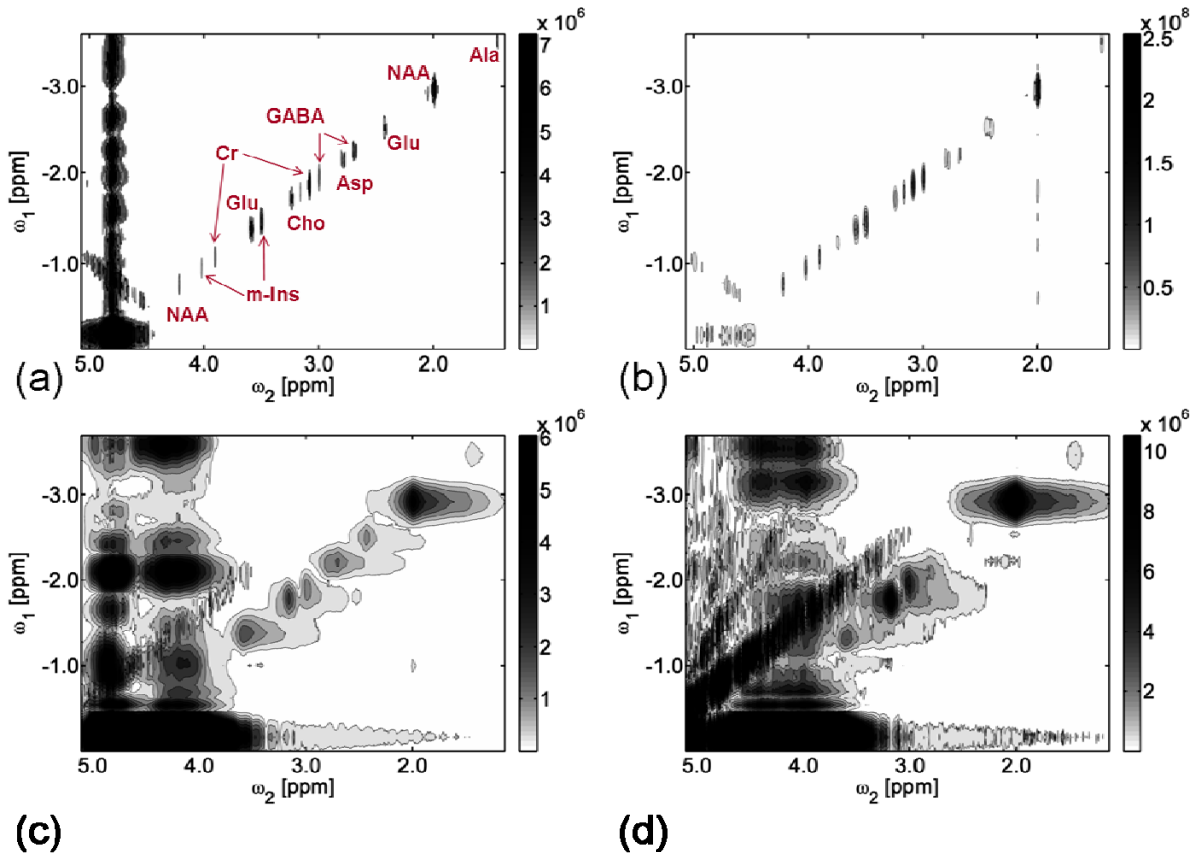


Figure 4.10: Water suppression efficiency of SEL-HOMOGENIZED in samples with low concentration. An agar gel phantom containing major brain metabolites at their typical *in vivo* concentration (108) was used (Table 4.3). (a) Spectrum of a homogeneous phantom acquired with the sequence shown in Fig. 4.1. Metabolite peaks are labelled. $TR/TE = 5.0/0.2$ s, $TD = 64 \times 2048$, $SW = 7 \times 7$ ppm, $G = 200$ mT/m, $T = 1$ ms, $NA = 1$. (b) Spectrum of a homogeneous phantom acquired with the sequence shown in Fig. 4.7b. (c) Spectrum of an inhomogeneous phantom containing randomly distributed air bubbles, acquired with the sequence shown in Fig. 4.1. The residual water peak dominates the spectrum for $\omega_2 > 3.8$ ppm. Only seven out of twelve metabolite peaks identified in the homogeneous phantom are detected. $TR/TE = 5.0/0.21$ s, $TD = 64 \times 2048$, $SW = 10 \times 10$ ppm, $G = 100$ mT/m, $T = 1$ ms, $NA = 1$. (d) Spectrum of the inhomogeneous phantom, acquired with the sequence shown in Fig. 4.7b. Water suppression in the presence of strong field distortions deteriorates spectral quality. Only the methyl peaks of NAA and Ala are clearly distinguishable. Scale bars in arbitrary intensity units.

Table 4.3: The composition of the brain phantoms used in experiments. Metabolites in the given concentration were dissolved in 50 ml water based 0.5 % Agar-gel.

Metabolite	Concentration (mM)
N-acetyl-aspartate (NAA)	10
Choline (Cho)	2.5
Creatine (Cr)	10
Glutamate (Glu)	15
Inositol (m-Ino)	8
Alanine (Ala)	1.4
γ -aminobutyric-acid (GABA)	2
Aspartate (Asp)	1.4
Ethanolamine (EtA)	3.3

4.3 Single voxel localization

Different gradient based localization methods can be combined with HOMOGENIZED. In principle, there are two fundamentally different strategies to localize iMQC-signal. The first possibility is to perform localization before the β -pulse, which implies localization of both M^+ and longitudinal magnetization making up the DDF. The second possibility is localization performed immediately prior to acquisition affecting only detectable magnetization. *In vivo* localization of the DDF-signal of water was initially achieved with the former strategy (109). In that study, a pulse sequence generating multiple spin echoes (through action of the DDF) was combined with localization gradients and pulses. Best results were reported for a PRESS localization (16). However, the authors observed “occasional refocusing of spurious echoes” (109). The slice selective application of pulses that create the DDF leaves parts of the sample experiencing only one or two pulses giving rise to an FID or a spin echo. These can, in principle, be suppressed by use of a phase cycle, but *in vivo*, motion or small physiological fluctuations may lead to artifacts. Therefore, in the approach followed in this thesis the pulses creating the DDF are not applied slice selectively and the localization is not combined with the three pulses in the HOMOGENIZED sequence.

There are three different localization schemes that fulfil this requirement. The associated pulse sequences will be referred to as S1, S2, and S3

4.3.1 Localization within the HOMOGENIZED sequence (S1)

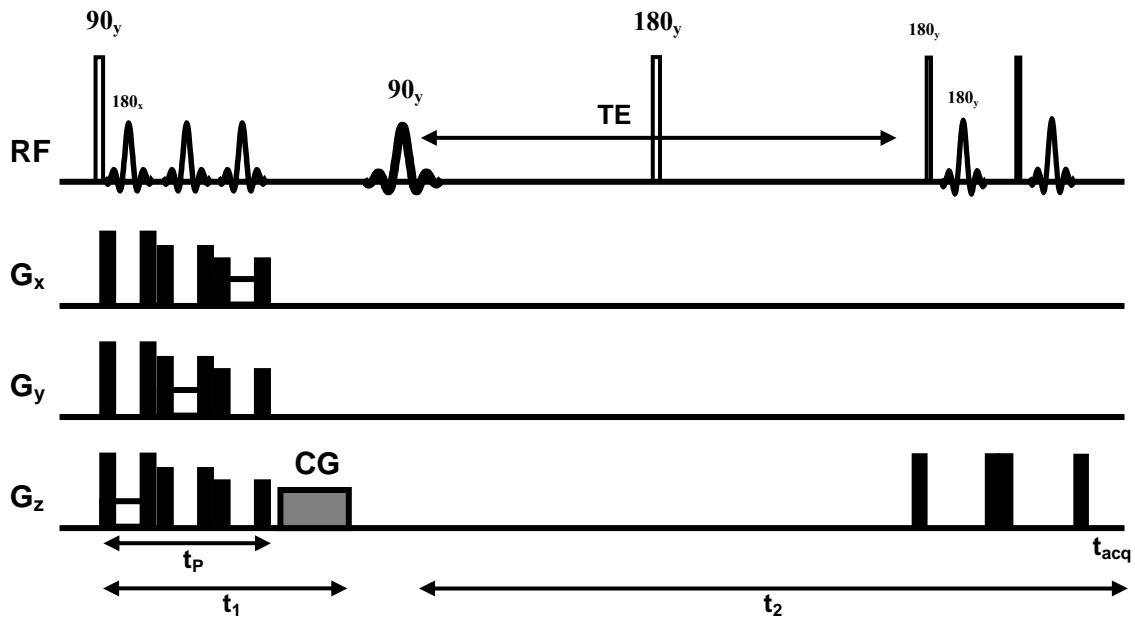


Figure 4.11: S1. Pulse sequence for spatially localized HOMOGENIZED spectroscopy with PRESS-like localization after the excitation pulse and two excitation sculpting WS modules prior to the acquisition. Empty bars are non selective, sinc-shapes selective RF-pulses, respectively. Flip angle and phase of the RF-pulses are indicated. Black squares are spoilers, empty squares are slice selection gradients. t_p is the duration of the PRESS-like module.

Similar to the technique used in the pioneering work (109), localization within the HOMOGENIZED sequence can be implemented by a PRESS-like (16) module after the

global excitation pulse (Fig. 4.11). Three slice-selective refocusing RF-pulses in orthogonal directions are each flanked by spoiler gradient pulses (spoilers). Since the volume selection is performed before the β -pulse, all spoilers have to be considered as correlation gradients. The three slice selection steps partition the sample outside the selected voxel, into regions experiencing two, four, or six unbalanced spoilers and the CG. Equation [4.9] shows that maximum signal is achieved if the modulation of the magnetization in t_1 is along the z-axis and that no signal arises if the modulation is along the magic angle. However, if the spoilers act along the magic angle and the CG along the z-axis, the unwanted signal outside the selected volume will still not be zero since the effective modulation angle is

$$\theta_{\text{out}} = \arctan \frac{\tan(54.74^\circ) \sum_{\text{Spoiler}} G_{\text{Sp}} T_{\text{Sp}}|_z}{GT + \sum_{\text{Spoiler}} G_{\text{Sp}} T_{\text{Sp}}|_z}. \quad [4.11]$$

Here $G_{\text{Sp}} T_{\text{Sp}}|_z$ is the z-component of a spoiler gradient. To minimize the deviation of θ_{out} from the magic angle, $G_{\text{Sp}} T_{\text{Sp}}$ has to be maximized. However, diffusion during slice selection attenuates the signal inside the selected volume. This attenuation increases with $G_{\text{Sp}} T_{\text{Sp}}$ and the duration of the refocusing gradient. Assuming that a significant amount of magnetization inside the selected voxel is not refocused when d_c reaches the mean diffusion distance, the upper limit of G_{Sp} can be determined as a function of T_{Sp} and slice selection time by setting the explicit expressions of d_c and the mean diffusion distance equal. The function we get this way, neglecting the diffusion weighting caused by the slice selection gradient, is

$$G_{\text{Sp}} = \frac{\pi}{\gamma T_{\text{Sp}} \sqrt{2D(T_{\text{Sp}} + T_{\text{loc}})}}, \quad [4.12]$$

where D is the diffusion constant and T_{loc} is the slice selection gradient duration. Equation [4.12] is plotted for $T_{\text{loc}} = 1$ ms in Fig. 4.12. Thus, spoilers of 3 ms duration flanking a 1 ms slice refocusing pulse must not exceed 90 G/cm. However, in order to minimize refocusing outside the voxel by deviation of θ_{out} from the magic angle, G_{Sp} needs to be maximized within this limit.

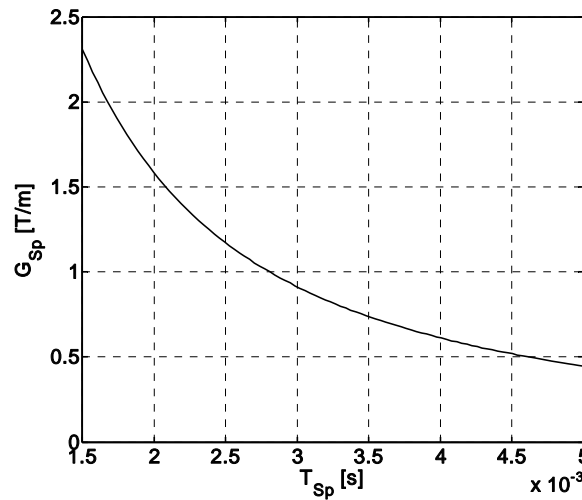


Figure 4.12: Spoiler strength limit for slice selection as function of spoiler duration in the SI sequence. The limit is set by the diffusion and governed by the relation in Equation [4.12]. The diffusion time is counted from the fully dephased state to the fully rephased state, thus, from the end of the first spoiler to the end of the second in the slice selection spin echo sandwich. Slice selection gradient duration was set to 1 ms. The mean diffusion distance is ranging from $3.4 \mu\text{m}$ to $5.3 \mu\text{m}$ for $1.5 \text{ ms} < T_{\text{sp}} < 5 \text{ ms}$.

4.3.2 Localization of the magnetization prior to a global HOMOGENIZED (S2)

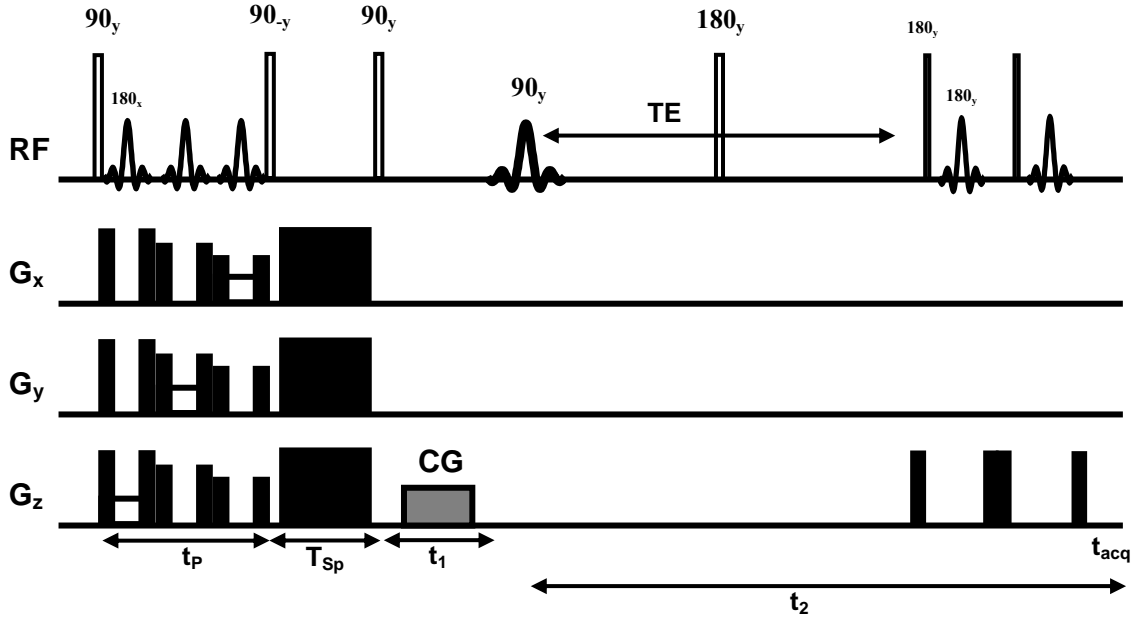


Figure 4.13: S2. Pulse sequence for spatially localized HOMOGENIZED spectroscopy with PRESS-like localization prior to the excitation and WS modules. Symbols as in Fig. 4.11. T_{Sp} is the duration of the strong magic angle spoiler module.

Another possibility to achieve localization is to separate the volume selection from the global HOMOGENIZED experiment. Sequence S2 (Fig. 4.13) uses outer volume suppression to limit longitudinal magnetization to a selected spatial region. After the global 90°_y excitation pulse and the volume selection module, the magnetization in the region of interest is in-phase, transverse and real. Magnetization outside the selected volume is dephased by the effect of the spoiler gradients and free precession. The second 90°_y pulse rotates part of the transverse magnetization back along the z-axis. During T_{Sp} a magic angle spoiler has to be applied with sufficient strength to cause, in combination with diffusion, irrecoverable loss of all transverse magnetization. Subsequently, a global HOMOGENIZED sequence delivers a spectrum from that region where longitudinal magnetization is present. This is mainly from inside the selected voxel, where Eq. [4.9] applies. Outside the voxel, longitudinal magnetization created by the second 90°_y pulse is strongly modulated by the slice selection gradients and spoilers. To calculate the analytical expression for signal evolution in this region, all gradients during t_p and t_1 have to be considered. The derivation steps presented in Appendix D are similar to those for the global SEL-HOMOGENIZED signal calculation (see Appendix B), and at the end we get the contribution to the solute signal coming from outside the selected voxel:

$$\begin{aligned}
 M^+(t_2) = & i \frac{M_0^S}{2} e^{i(\Delta\omega_S - \Delta\omega_I)(t_p + t_1)} e^{i\Delta\omega_S t_2} J_1\left(-\frac{\Delta_s t_2}{3\tau_{dl}}\right) J_0\left(-\frac{\Delta_s t_2}{3\tau_{dl}}\right) \\
 & + i \frac{M_0^S}{2} e^{i(\Delta\omega_I - \Delta\omega_S)(t_p - t_1)} e^{i\Delta\omega_S t_2} J_1\left(-\frac{\Delta_s t_2}{3\tau_{dl}}\right) J_0\left(-\frac{\Delta_s t_2}{3\tau_{dl}}\right).
 \end{aligned} \quad [4.13]$$

Equation [4.13] suggests that the spins outside the selected volume experience a DDF modified by the localization spoilers, which creates two cross-peaks. This effect is rather similar to that created by a HOMOGENIZED sequence with a global β -pulse, than to SEL-HOMOGENIZED. However, signal from the selected volume is observed exclusively at $\omega_1 =$

$\Delta\omega_S - \Delta\omega_I$ (37). Thus, for the analysis of localization efficiency the second term in Eq. [4.13], which results in cross-peaks at $\omega_I = \Delta\omega_I - \Delta\omega_S$ in the 2D spectrum, is omitted, and in the following the signal outside the voxel is considered to be:

$$M^+(t_2) = i \frac{M_0^S}{2} e^{i(\Delta\omega_S - \Delta\omega_I)(t_p + t_1)} e^{i\Delta\omega_S t_2} J_1\left(-\frac{\Delta_s t_2}{3\tau_{dl}}\right) J_0\left(-\frac{\Delta_s t_2}{3\tau_{dl}}\right). \quad [4.14]$$

The effective values of Δ_s and t_p depend on the position in the sample and differ for regions where the magnetization is refocused by two, one, or no 180° pulses and experience two, four, or six spoilers, respectively.

4.3.3 Localization of detectable signal immediately prior to acquisition (S3)

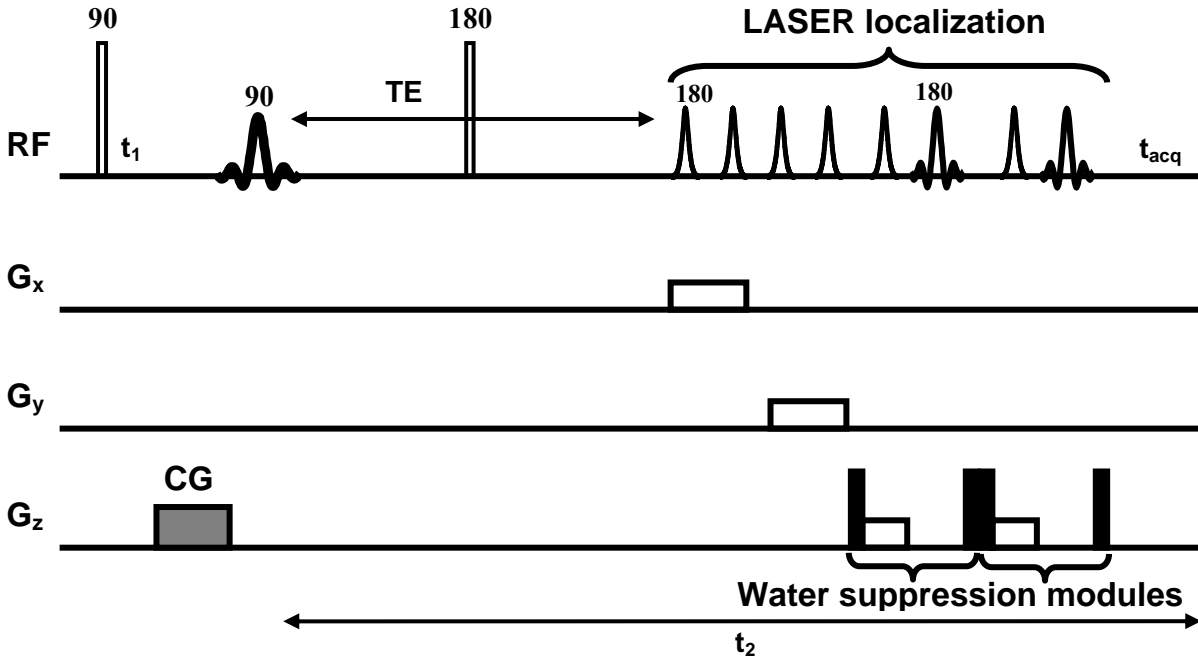


Figure 4.14: S3. Pulse sequence for spatially localized HOMOGENIZED spectroscopy with localization immediately prior to acquisition. Symbols as in Fig. 4.11. Hypersecant profiles indicate adiabatic inversion pulses, which can be used pair-wise together with slice selection gradients for localization (18). Spoilers of the LASER localization module are not shown.

The third possibility to localize signal from a HOMOGENIZED experiment is to refocus the signal after the β -pulse in a spatially selective manner (110). Slice refocusing modules with balanced spoiler gradients after the β -pulse have no effect on the DDF. Thus, signal evolution outside the selected volume does not depend on the direction of the spoiler modulation angle, making total elimination of signal from this region possible. Figure 4.14 shows an implementation of S3, which uses the localization by adiabatic selective refocusing (LASER) (18) sequence with six adiabatic inversion pulses to selectively refocus three orthogonal slices. The sequence in Fig. 4.14 is an improved version of an experiment proposed previously (110). Modifications are:

1. Duration of localization is minimized and performed immediately prior to acquisition to avoid signal loss caused by diffusion and the spoilers. In order to allow the signal to build up, an additional 180° pulse is inserted before localization.

2. Water suppression is achieved with two modified excitation sculpting modules (*III*) using slice selection pulses for global refocusing in the frequency domain.

4.3.4 The limits of localization efficiency of S1 and S2

Localized MR spectroscopy usually detects signal from a small voxel compared to the region where suppression of signal is desired. Therefore, recovery of only a small fraction of signal from outside the selected voxel may lead to significant contaminations in the spectrum. This is, in particular, important for a localized HOMOGENIZED experiment, since dephased magnetization is refocused by the DDF. The fraction of magnetization that is refocused outside the selected volume after localization with S1 is plotted in Fig. 4.15 for different spoiler gradients. Effective modulation angles resulting from the combined action of spoiler and correlation gradients are indicated. $\theta_{\text{out}} = 0^\circ$ corresponds to the selected voxel (dashed line). The curves illustrate that for moderate spoiler gradients, large portions of the signal outside the selected voxel are refocused during a period of a few hundred milliseconds. Even with very strong spoilers, the magnetization reaches several percent of the equilibrium magnetization. In the experiment, relaxation and diffusion will attenuate signal build-up. For evolution times longer than τ_d , there is no analytical solution of the Bloch equations available for a system of two inequivalent spins including the DDF, relaxation, and diffusion (74). Therefore, it can only be assumed that with strong selection gradients, signal suppression outside the selected voxel is more efficient than shown in Fig. 4.15. However, if the voxel is small compared to the rest of the sample, strong signal contributions from unwanted regions have to be expected.

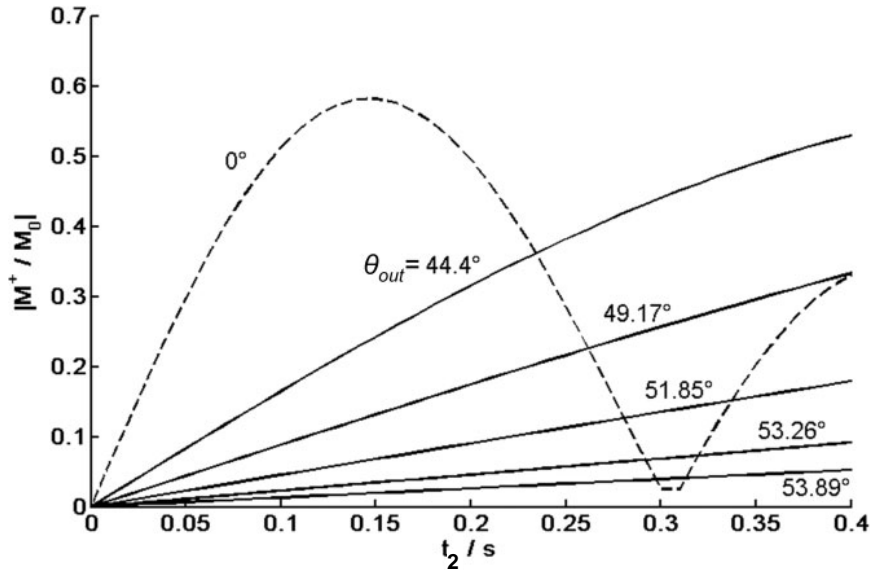


Figure 4.15: Theoretical signal evolution (Eq. [4.9]) of transverse magnetization experiencing all spoiler gradients and no refocusing during t_1 for localization with S1. $G = 20$ G/cm, $T = 1$ ms (CG parameters), together with $T_{sp} = 3$ ms and $G_{sp} = \{39.2, 35, 20, 10, 5, 2.5\}$ G/cm result in the modulation angles indicated. The dashed curve gives the evolution of transverse magnetization inside the selected volume. Further parameters were: $\omega_0 = 750$ MHz, $\Delta\omega_s = -2000$ Hz, $\Delta\omega_l = 500$ Hz, $T = 300$ K, $t_1 = 27$ ms, $t_p = 21$ ms, and localization pulse duration $T_{loc} = 1$ ms. Concentrations were $c_s = 1$ M and $c_l = 110$ M.

Signal build-up in regions dephased by two, four, or six spoilers of 35 G/cm is shown after localization with S1 (Fig. 4.16a) and S2 (Fig. 4.16b). For S1, outside the selected voxel

several percent of the equilibrium magnetization is refocused quickly, especially in the regions refocused by two 180° pulses. For S2, the situation is less dramatic. Only in the doubly refocused regions more than 2 % of the magnetization is recovered. Considering that relaxation and diffusion both attenuate the signal, Fig. 4.16b suggests that S2 allows for better localization than S1.

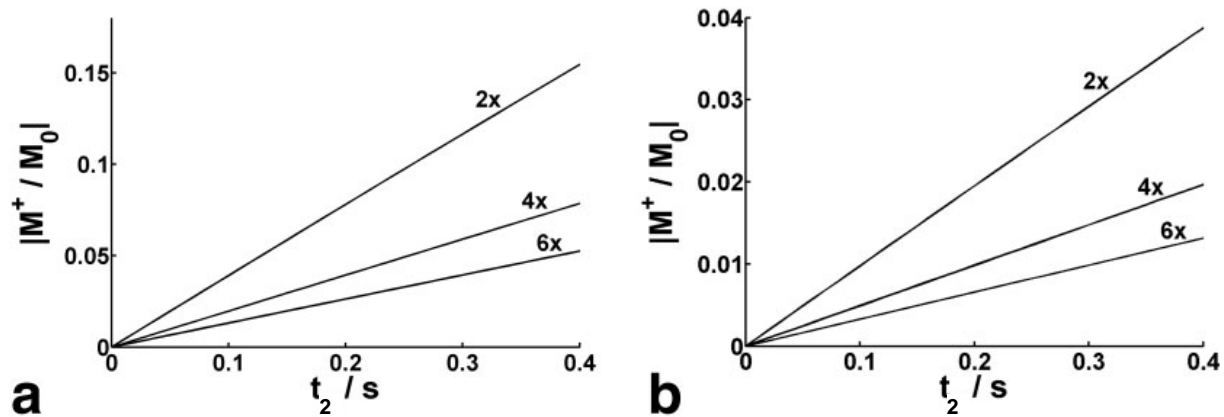


Figure 4.16: Signal build-up in sample partitions experiencing two, four, or six spoiler gradients. (a) After localization with S1 (Eq. [4.9]), $t_1 = 13$ ms, 20 ms, and 27 ms, for two, four, or six spoilers, respectively. (b) After localization with S2 (Eq. [4.14]), $t_1 = 7$ ms, 14 ms and 21 ms, for two, four, or six spoilers, respectively. Multipliers represent the number of experienced spoiler gradients. $G_{sp} = 35$ G/cm.

4.3.4 Experimental comparison of localization techniques in a phantom

4.3.4.1 MATERIALS AND METHODS

In vitro experiments were performed on a Bruker 17.6 T widebore spectrometer to compare the localization efficiency of S1, S2 and S3. The phantom used was a 20 mm outer diameter glass tube filled with 1 M choline (Cho) solution, containing two Eppendorf caps filled with 1 M NAA and 1 M Cho, respectively. Measurements were carried out with a 20 mm inner diameter birdcage coil and a micro-imaging gradient system with 1 T/m maximum gradient strength. Shimming was done with the automatic algorithm FASTMAP (15) on voxels limited by the outer tube walls. For data acquisition and processing Paravision 3.0.2 (Bruker BioSpin GmbH, Rheinstetten, Germany) and MATLAB 7.0.1 (The MathWorks Inc., Natick, MA, USA) were employed.

4.3.4.2 RESULTS

The structure of the phantom and the position of the selected $(6 \text{ mm})^3$ voxel are shown in Fig. 4.17a. The global HOMOGENIZED spectrum obtained from this phantom is presented in Fig. 4.17b. Both choline and NAA were detected. The localization efficiency of the sequences S1, S2 and S3 was compared relative to this global spectrum by calculating the ratio between the Cho and NAA methyl peaks (Table 4.4).

Table 4.4: Choline / NAA methyl peak ratios indicating the localization efficiency of the iZQC-sequences.

Global	S1	S2	S3
2.4	0.83	0.38	0.11

After localizing the signal to a voxel in the NAA compartment with S1 (data not shown) less than 70 % of the Cho signal was suppressed. This confirms the theoretical predictions of Fig. 4.16a that S1 provides only poor localization. After localization with S2 (Fig. 4.17c) only 15 % of the total Cho signal remains. Best localization was achieved with S3 (Fig. 4.17d), which achieved a localization efficiency of 95 %. Inspecting the water peak one observes that this is most efficiently suppressed also in the S3 spectrum. While the analysis of the S2 signal (Appendix D) shows that water magnetization from outside the selected volume is not fully eliminated, localizing the SEL-HOMOGENIZED signal with S3 assures that only water within the voxel can be detected and should be eventually suppressed with additional WS-modules. These results clearly favour S3 for applications *in vivo*.

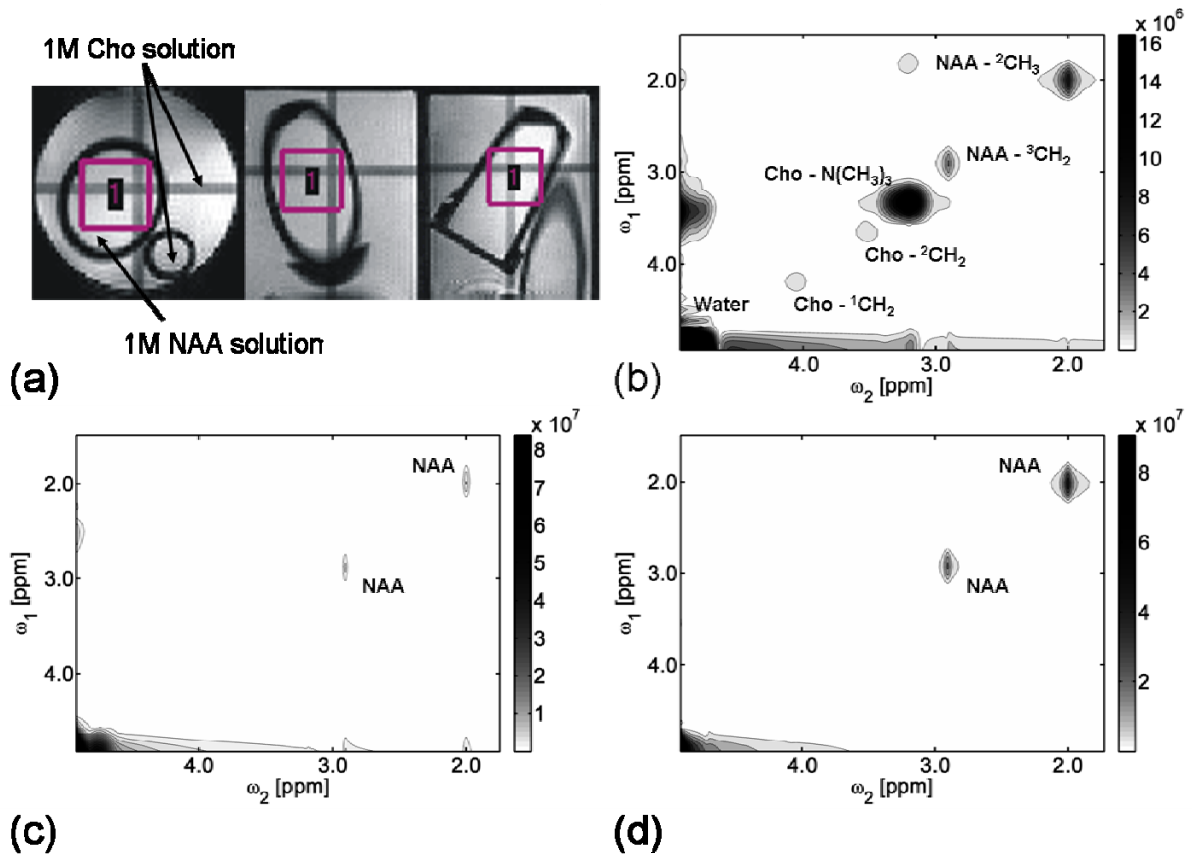


Figure 4.17: HOMOGEnIZED spectra of a compartment phantom. (a) Gradient echo images of three orthogonal slices showing the geometry and structure of the phantom. Orientation of the two other slices can be seen as lines with reduced signal intensity in each image. The position of the selected volume is indicated by the grey box. (b) Global 2D HOMOGEnIZED spectrum with labelled peaks. $TR = 5$ s, $TE = 270$ ms, acquired data points $TD = 64 * 2048$, frequency bandwidth $SW = 8 * 8$ ppm, $CG = 20$ G/cm * 1 ms. (c) 2D HOMOGEnIZED spectrum localized with S2. (d) 2D HOMOGEnIZED spectrum localized with S3. Scale bars in arbitrary intensity units.

4.3.5 Avoiding the chemical shift displacement artefact with S1 and S2

S1 and S2 share one special characteristic worth noting. Localization is achieved by limiting the DDF originating from water spins and transverse magnetization of metabolite spins to a selected voxel. Since water and metabolite spins have different chemical shifts, voxel localization will be slightly different for both. This is illustrated in Fig. 4.18 for resonance A and B.

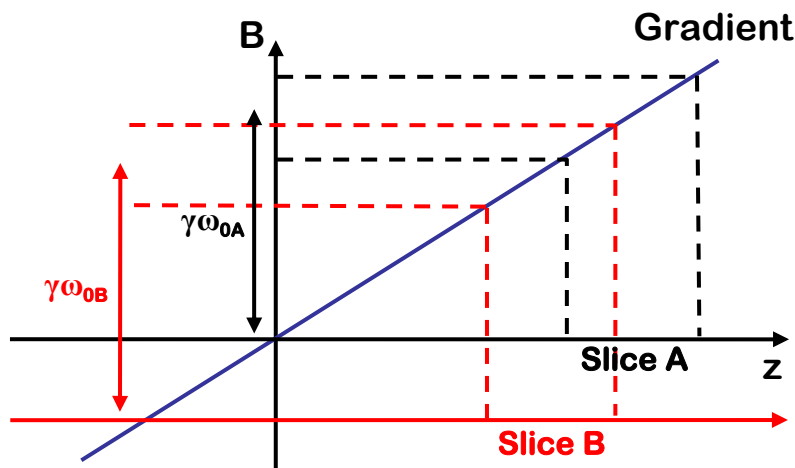


Figure 4.18: *The principle of the chemical shift displacement artefact.*

On the magnetic induction axis (**B**) an RF-pulse excites sections with the same bandwidth, but at different positions for A (black) and B (red). According to the principles of space encoding, a field gradient in z-direction will select different slices for A and B with the same thickness, but shifted with respect to one another along the z-axis. The displacement in the z-direction can be calculated for the slice selection gradient G_z with the equation:

$$\Delta z = \frac{\omega_{0A} - \omega_{0B}}{\gamma G_z}. \quad [4.15]$$

This phenomenon is often called “chemical shift artefact” and may lead to misregistration in conventional localized spectroscopy. In case of S1 and S2 the signal is expected to arise only from the water voxel, because the DDF is limited to that region.

Voxel displacement experiments with S2 were performed with a phantom built of two concentric glass cylinders with 15 mm and 10 mm outer diameters, filled with 1 M Cho and 1 M NAA, respectively. A 15 mm inner diameter birdcage coil was used.

In the iZQC spectra obtained, signal is only created in the overlapping regions of water and metabolite voxels. This is illustrated in Fig. 4.19. The geometry of the phantom and position of the voxels are shown in gradient echo images. Global 1D and HOMOGENIZED spectra are shown in Fig. 4.19a. Peaks of both Cho and NAA were observed.

If the water voxel is localized in the Cho compartment as shown in Fig. 4.19b, only Cho signals are detected in the iZQC spectrum obtained with S2. In contrast, in the PRESS spectrum NAA peaks are also detected, because localization for the NAA signals (white) is shifted by 2.24 mm in the longitudinal and 1.47 mm in the transverse directions with respect to water (black). If the water voxel extends into both compartments as shown in Fig. 4.19c, in both the iZQC and the PRESS spectrum only NAA is observed (shifted by 1.24 mm in all

directions for PRESS), because the choline voxel shifts into the outer tube (white) by 815 μm in all directions compared to the water voxel (black).

Obviously, if the chemical shift displacement is large the overlap between the water and the metabolite voxel gets smaller and iZQC-signal can be dramatically reduced. Therefore, it is still essential to reduce the chemical shift displacement by using large bandwidth refocusing pulses for slice selection, which allow for stronger localization gradients (see again Eq. [4.12]).

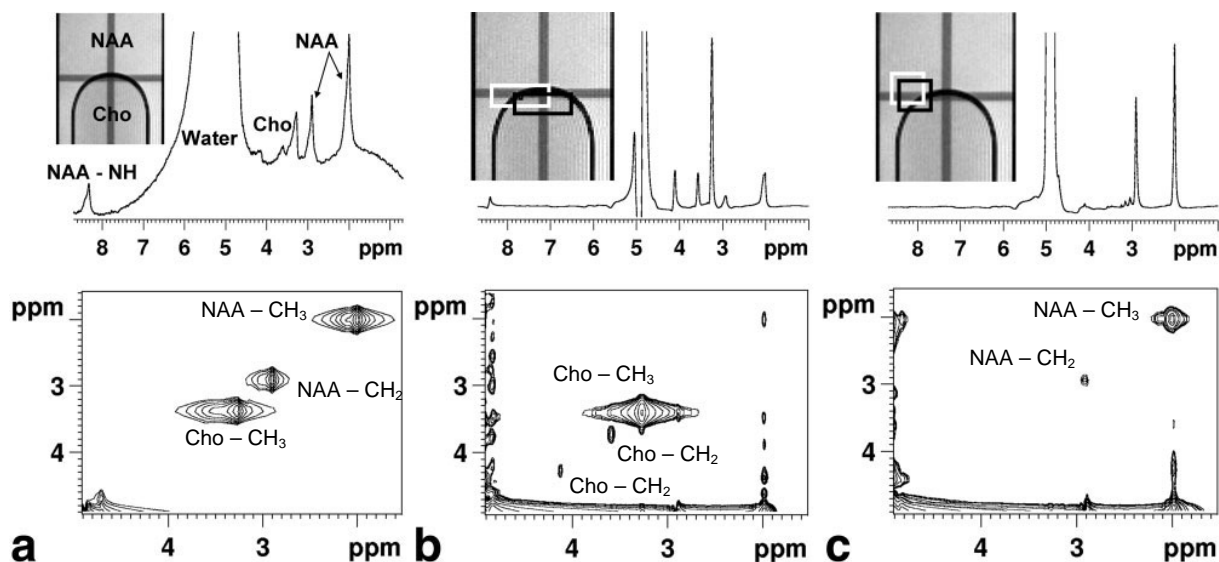


Figure 4.19: PRESS and 2D HOMOGENIZED spectra localized with S2. Gradient echo images show geometry of the phantom and the position of the voxels (water black, NAA / Cho white) (a) Global 1D and HOMOGENIZED spectra (b) PRESS and S2 spectra selecting a $2.0 \times 5.4 \times 5.4 \text{ mm}^3$ water voxel inside the compartment with Cho. The NAA voxel (white) is shifted into the NAA containing compartment. (c) PRESS and S2 spectra selecting a $(3 \text{ mm})^3$ water voxel extending into both compartments. The choline voxel (white) is completely shifted into the NAA containing compartment. Experimental parameters were: PRESS: $TR = 2 \text{ s}$, $TE = 20 \text{ ms}$, $TD = 4096$, $SW = 10 \text{ ppm}$, 16 averages. HOMOGENIZED: $TR = 5 \text{ s}$, $TE = 270 \text{ ms}$, $TD = 64 * 2048$, $SW = 8 * 8 \text{ ppm}$, $CG = 20 \text{ G/cm} * 1 \text{ ms}$.

5. In vivo applications of localized iZQC MRS

The first successful acquisition of HOMOGENIZED spectra *in vivo* was conducted in the rat brain using the original pulse sequence (Fig. 3.1). Although no localization was performed and signal was acquired from the whole head, resonances of the major brain metabolites were detected (92). Compared to conventional global 1D spectra, which displayed solely the water resonance, additional information was obtained. However, significant improvement of spectral quality was expected with the optimized sequence in Fig. 4.14.

Validation of the new method was performed in the rat, and later in the mouse brain. Arguments for the choice of this organ were its relatively large size and smooth internal structure. The usual argument, that metabolic changes in the brain are important indicators of physiological changes in the whole organism, had less relevance in this case. Since the spectral resolution in conventional MR spectra of the brain can be efficiently enhanced by shimming, iZQC MRS was applied in organs where other MRS techniques have limited applicability.

An organ with great information potential, but not easily accessible for conventional MRS, is the spinal cord. MRS in the spinal cord is of particular interest in combination with MRI for the diagnosis of neurodegenerative diseases, and for the monitoring of spontaneous or induced tissue repair after experimental traumatic injuries. Investigations of possible therapies employ MRI for the detection of implanted stem cells, labelled with paramagnetic microparticles. MR spectral quality deteriorates in the presence of iron particles, of the induced morphological deformations and of haemorrhages. Under such circumstances shimming alone cannot compensate for the field perturbations.

Similarly, in tumors, the complex inner structure often denies arbitrary voxel selection for conventional single-voxel MRS, and metabolic information has reduced spatial availability. HOMOGENIZED may overcome this problem. Moreover, in large tumors, acquisition of spectra from larger voxels may also enhance the signal efficiency of iZQC MRS compared to conventional methods.

5.1 Experimental hardware and animal preparation

5.1.1 Materials for *in vivo* experiments

In vivo experiments were performed with a Bruker 17.6 T / 89 mm vertical wide-bore magnet interfaced to an Avance750 spectrometer. The software used for sequence programming and data acquisition was Paravision 3.0.2. For measurements on the rat brain, spinal cord and mouse tumor a Bruker Mini 0.5 gradient system with 57 mm inner diameter (id), 0.2 T/m maximum strength, and 180 μ s rise time was used. In case of the rat brain and spinal cord a transmit-receive surface coil was employed, which was mounted on a half-cylindrical carrier with the long axis along z (112). Tumor spectra were acquired with a birdcage coil with 38 mm id. For experiments on the mouse brain a Bruker Micro 2.5 gradient system with 40 mm id, 1 T/m peak strength and 110 μ s rise time was employed. The RF-coil was a Bruker birdcage volume resonator with a 20 mm id.

5.1.2 Animal handling

Healthy female Fisher 344 rats and male B6 mice were anesthetized by spontaneous inhalation of oxygen with 4 % isoflurane and were kept in this state with 1.2 – 2 % isoflurane. Since animals within the handling system and the probe-head completely filled the volume inside the gradient system, the body temperature was maintained by controlling the gradient cooling unit ($T = 30 \pm 2$ °C and 37 ± 2 °C for rats and mice, respectively). Experiments were triggered on breathing and the electrocardiogram was observed with a monitoring unit (Rapid Biomedical, Rimpfing, Germany).

5.2 Validation of single-voxel iZQC MRS in the rodent brain

The pulse sequence developed for *in vivo* iZQC spectroscopy as a part of this work (Fig. 4.14) was tested in the brain of rats and mice. Parameters were empirically optimized during several animal experiments.

5.2.1 Acquisition parameters and processing

HOMOGENIZED voxels were positioned to include most of the brain volume, but to avoid susceptibility gradients near the skull. Pulse calibration could be efficiently performed with the automatic algorithm included in the Paravision software. Repetition times between 3 and 5 seconds were used to allow almost complete T_1 -relaxation, but to avoid signal loss caused by physiological changes or movement.

In vivo spectra were mostly acquired from a spectral range of 8 to 10 ppm around the water resonance in both dimensions, because most important brain metabolite resonances are less than 4 ppm away from the water peak. The acquisition window was set to include the maximum of the theoretical signal evolution (Sec. 4.1.2) and was optimized for best spectral quality. The excitation pulse was phase cycled in order to increase iZQC selection efficiency.

Raw data was attenuated along ω_2 by an exponential filter function, zero-filled by a factor of two and Fourier-transformed in both dimensions. Polynomial baseline correction was performed. Presented results are in magnitude mode.

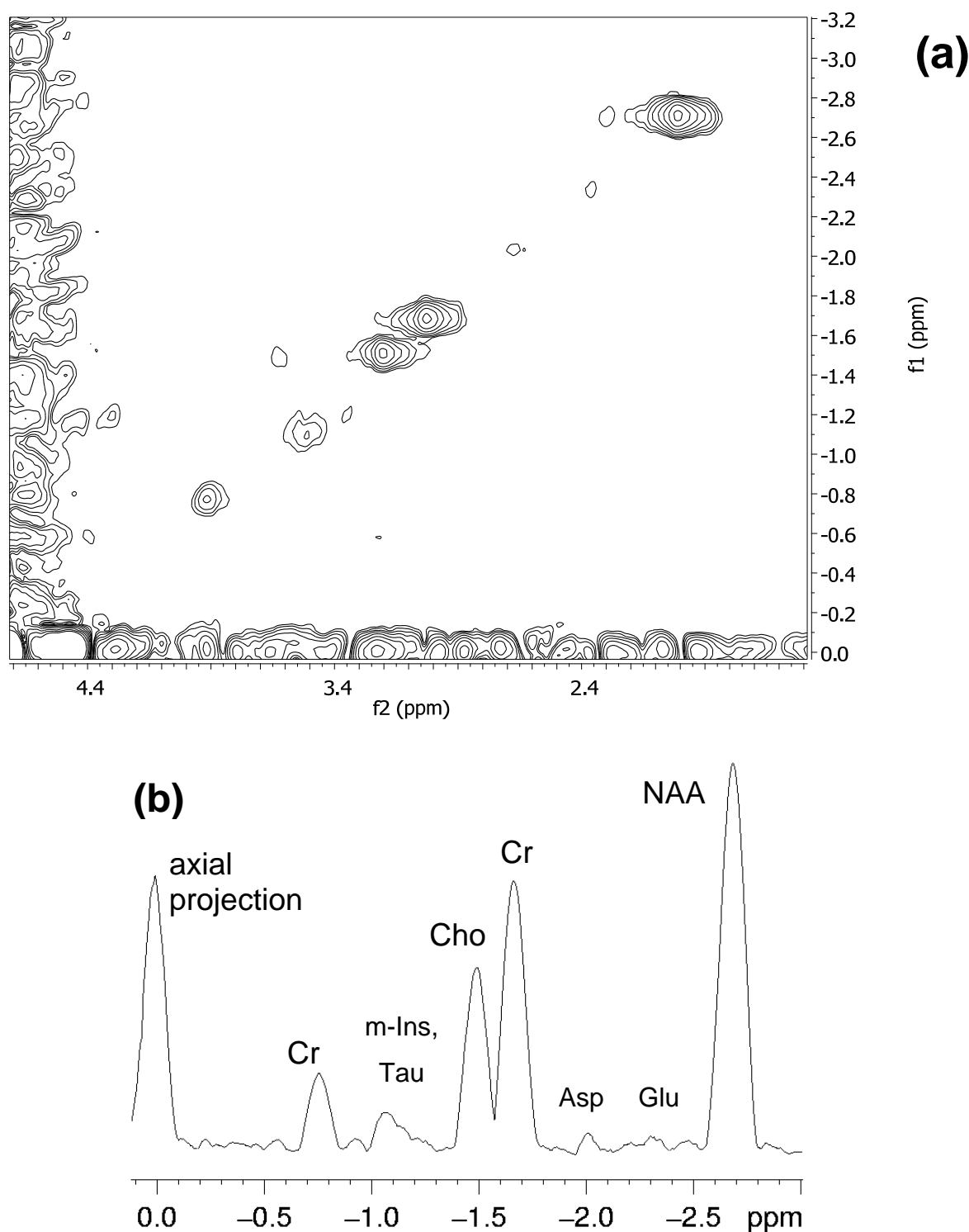


Figure 5.1: (a) *In vivo* HOMOGENIZED spectrum from a $(8\text{ mm})^3$ voxel in the brain of a female Fisher rat acquired with a surface coil using the sequence shown in Fig. 4.14. $TR/TE = 5.0/0.18\text{ s}$, $TD = 128 \times 2048$, $SW = 8 \times 8\text{ ppm}$, $G = 10\text{ G/cm}$, $T = 1\text{ ms}$, $NA = 2$, $ph1 = (x, -x)$, $t_{\text{experiment}} = 25\text{ min}$. (b) ω_1 -projection of the spectral region between $\omega_2 = -3.0\text{ ppm}$ and -0.5 ppm . The four major brain singlet resonances can be identified (labelled). J-coupled resonances produced further cross-peaks with this experimental setup (tentative assignments are indicated).

5.2.2 Results

Using the pulse sequence shown in Fig. 4.14, HOMOGENIZED spectra from the rat brain (Fig. 5.1) and the mouse brain (Fig. 5.2) can be recorded. In both rodents the four major singlet peaks of methyl NAA, methyl and ethyl Cr, and methyl Cho are observed. In the spectrum of the rat additional peaks can be observed and putatively assigned to J-coupled molecular groups. The ω_1 -projection of that spectrum (Fig. 5.1b) shows that high-quality spectra can be obtained with the optimized HOMOGENIZED sequence.

In the range of acquired t_1 -increments, up to 128, resolution improves for more increments. Thus, along ω_1 , digital resolution is a limiting factor for spectral quality, because of the small number of t_1 -increments. Nevertheless, in Fig. 5.1a peaks along the direct dimension (ω_2), where digital resolution is more than factor 10 higher, are broader than peaks along ω_1 . Therefore, it seems that field inhomogeneities have less influence on the linewidth along ω_1 . However, the effect of inhomogeneities on the iZQC spectrum is complex and will be analyzed in more detail in Chapter 6.

Shimming *in vivo* on big voxels, as used here, is not efficient. Therefore, conventional methods, which depend on shimming, must decrease voxel size for spectral quality. Still, the approximate factor ten signal gain and the relatively homogeneous structure of the brain, allows them to acquire high quality spectra from smaller voxels in shorter time than HOMOGENIZED.

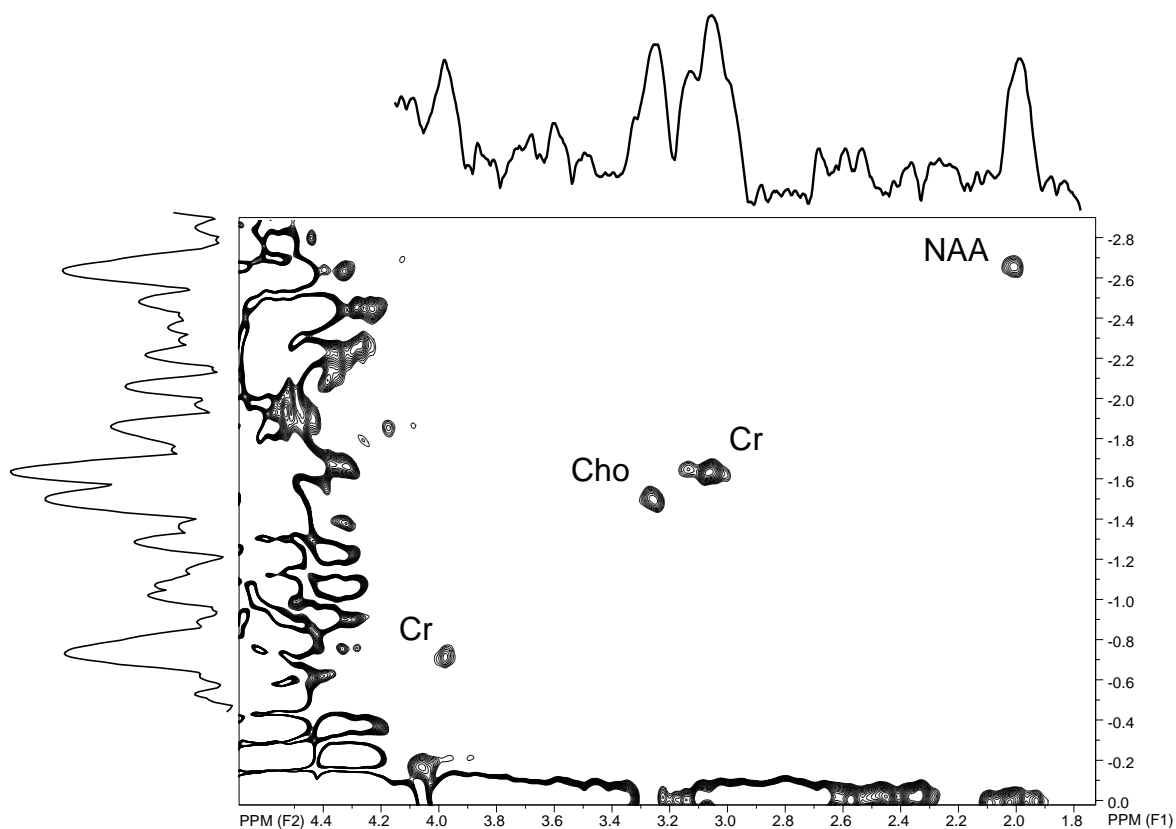


Figure 5.2: Spectrum from a $6 \times 4 \times 12 \text{ mm}^3$ voxel in the mouse brain acquired with a volume coil. The spectral range $\omega_2 = (1.8 \text{ ppm}, 4.2 \text{ ppm})$ and $\omega_1 = (-0.5 \text{ ppm}, -2.9 \text{ ppm})$ are projected on the left and on top of the 2D spectrum, respectively. The four singlet resonances of the major brain metabolites were observed. $TR/TE = 3.0/0.12 \text{ s}$, $TD = 64 \times 1024$, $SW = 9 \times 9 \text{ ppm}$, $G = 10 \text{ G/cm}$, $T = 1 \text{ ms}$, $NA = 2$, $ph1 = (x, -x)$, $t_{\text{experiment}} = 7 \text{ min}$.

5.3 Feasibility of conventional and iZQC MRS in the rat spinal cord

at 17.6 T³

MRS in the spinal cord may provide complementary information to MRI, and help for a better monitoring of physiological changes in long term studies. *In vivo* MR microscopy of healthy and injured rodent spinal cords is well established (113-117) and has recently been implemented for investigations of spinal cord injury (SCI) models in rats at very high magnetic fields (112,118). Non-invasive, long-term monitoring of spontaneous disease evolution after SCI in humans (119), rats (114,118,120,121), and mice (117,122,123) using MRI provides essential information about degenerative and regenerative physiological processes. Induced tissue regeneration after SCI by implantation of neural stem cells was first demonstrated invasively by histopathological methods using immunocytochemical labelling and subsequent fluorescence microscopy examinations (124-126). Recently, non-invasive MRI monitoring of alginate implants in the spinal cord of healthy rats *in vivo* (127) and of stem cells labelled with super-paramagnetic iron-oxide nano-particles in the myelin deficient rat spinal cord *ex vivo* (128) has been reported. In particular, after transplantations, MRS could be a valuable asset and provide information which is not available from MRI. While imaging is used to monitor cell migration or local inflammations, MRS may yield direct insight into local metabolism after transplantation.

In vivo MRS studies of spinal cord pathologies were already performed in human multiple sclerosis cases (129) and on an experimental autoimmune encephalomyelitis rat model (130). The first applications of MRS for the quantification of absolute metabolite concentrations in the cervical section of the healthy human spinal cord were reported recently (131,132). Similar quantification in small animals has not been reported to date, which is presumably due to the small size of their spinal cord. By using implanted RF-coils in a rat model, a significant sensitivity enhancement was achieved and high quality spectra were presented (133,134).

Two questions are addressed here: First, is it experimentally possible to obtain high quality *in vivo* MR spectra from the healthy rat spinal cord at a magnetic field strength of 17.6 T? Second, can iZQC spectra be obtained *in vivo* from the rat spinal cord and do they provide advantages in resolution or sensitivity compared to conventional methods?

5.3.1 Materials and Methods

Experiments were performed on healthy rats weighting between 130 g and 160 g with ages between 14 and 20 weeks. Animals were positioned inside the magnet by adjusting the position of the cradle, using a millimetre scaled mechanical positioning system, until the first lumbar (L1) vertebra of the rat was centred (see image in Fig. 5.3). Data acquisition was triggered on breathing to avoid movement artifacts. Automatic pulse calibration failed. To account for the B₁-profile of the surface coil, excitation profiles were mapped with gradient echo images acquired with a pre-pulse. The strength of the pre-pulse was adjusted to achieve full saturation (90°) over the largest possible region of the spinal cord. Refocusing and

³ This section was adapted from Ref. (38).

inversion pulse strengths were corrected accordingly. While this method of pulse calibration was robust for non-selective pulses, the excitation profile of slice selective pulses was strongly influenced by magnetic field homogeneity. To minimize field variations, a $(3\text{ mm})^3$ voxel, positioned inside the spinal cord and centrally along z-direction, was shimmed using FASTMAP prior to pulse calibration. Only first-order shim corrections were applicable, because second-order coefficients exceeded the available shim gradient power. For larger voxels extending into the surrounding bone, shimming with FASTMAP was not possible. Acquisition parameters for all experiments are listed in Table 5.1. Each voxel was centred as shown for a $(2\text{ mm})^3$ voxel in Fig. 5.3. In iZQC experiments voxels extended into the surrounding bone and thus fully contained the cross section of the spinal cord. Extension in z-direction was limited only by the B_1 -profile of the coil. For PRESS spectroscopy, the variable power and optimized relaxation delays (VAPOR) pre-saturation technique was used for efficient suppression of the water signal (135). The repetition time was 3 s and the spectral width was 8 ppm. For HOMOGENIZED spectroscopy excitation pulse- and receiver frequencies were shifted by 500 Hz and a four-step phase cycle (ph1 = x/-x/y/-y, ph2 = x/x/y/y, phrec = -x/-x/y/y, for the first pulse, second pulse, and receiver, respectively) was used to suppress signal from unwanted coherence orders. Further parameters were: TR = 3 s, CG = 10 G/cm applied for 1 ms, spoiler gradients not exceeding CG, SW = 8 x 8 ppm.

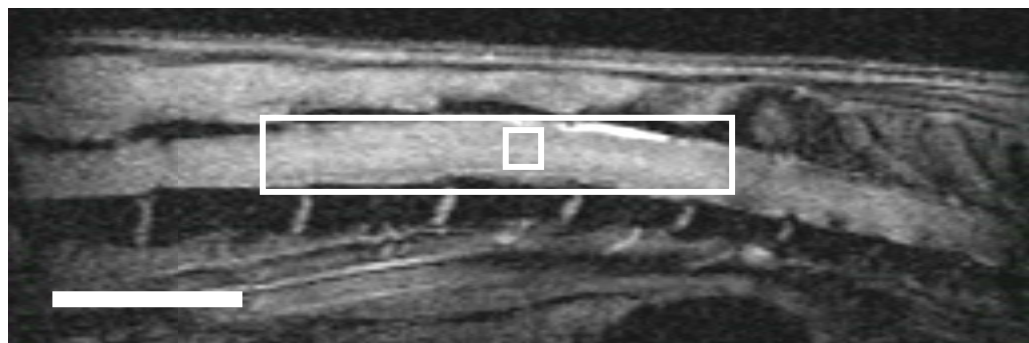


Figure 5.3: *In vivo* sagittal gradient echo image of the rat spinal cord. Scale bar: 1 cm. The small square shows the position of a $(2\text{ mm})^3$ voxel selected in the PRESS experiments. The large square shows the $4 \times 4 \times 25\text{ mm}^3$ voxel for HOMOGENIZED.

Raw data processing and peak fitting were performed with Matlab 7.3.0 and jMRUI 3.0 (136). *In vivo* PRESS free induction decay data were multiplied with an exponential function with line broadening (LB) of 15 Hz, zero-filled by a factor of two and Fourier transformed (FT). Phasing and baseline correction, using an algorithm suitable for low signal to noise data (137), were performed in the frequency domain. Lorentzian-fitting of the singlet peaks at 2.0 ppm (NAA, methyl), 3.0 ppm (Cr, methyl), 3.2 ppm (Cho, methyl) and 3.9 ppm (Cr, ethyl) was performed after an inverse FT in the time domain with the advanced method for accurate, robust, and efficient spectral fitting routine (AMARES) (138). The criteria for acceptance of a fit were: a) FID amplitudes were higher than 20 % of the standard deviation (SD); b) the ethyl-methyl ratio of Cr was between 0.5 and 0.75; c) the residuum contained only noise at sites where peaks were fitted. The SNR was calculated by dividing the maximum metabolite peak intensity of the real part of the spectrum by the SD of the region between 6.0 ppm and 8.0 ppm. To compare spectra acquired with different measurement times, SNR efficiencies were calculated by dividing the obtained SNR value by the square root of the measurement time.

Processing of the *in vivo* HOMOGENIZED time domain data was performed as described above for PRESS with additional application of FT, phase and baseline correction in the indirect dimension (ω_1). To calculate peak ratios, the singlet peaks of NAA, Cr, and Cho were integrated over an ellipsoidal region around the maximum in absolute mode 2D spectra. For

SNR calculation and for the determination of spectral linewidths, ω_1 traces at the maximum intensity of the observed peaks were extracted from phase sensitive spectra. SNR was calculated by dividing the maximum intensity of the highest metabolite peak by the baseline signal from the region between 6.0 ppm and 8.0 ppm. Linewidths of the NAA methyl peaks were measured at half maximum along the indirect dimension.

Table 5.1: Parameters of the *in vivo* experiments

Rat	Experiment type	Voxel size	TE ^a	NA ^b	TD ^c	ACQ ^d
#1	PRESS	(2 mm) ³	60 ms	512	2k ^e	45 min
#1	PRESS	2 x 2 x 4 mm ³	60 ms	128	2k	11 min
#1	PRESS	2 x 2 x 8 mm ³	60 ms	256	2k	22 min
#1	PRESS	(2 mm) ³	20 ms	256	2k	22 min
#1	PRESS	2 x 2 x 8 mm ³	20 ms	128	2k	11 min
#1	HOMOGENIZED	4 x 4 x 25 mm ³	60 ms	8	128 x 1k	95 min
#2	PRESS	(2 mm) ³	30 ms	128	2k	11 min
#2	PRESS	2 x 2 x 4 mm ³	30 ms	128	2k	11 min
#2	PRESS	2 x 2 x 6 mm ³	30 ms	128	2k	11 min
#2	HOMOGENIZED	4.5 x 4.5 x 18 mm ³	100 ms	8	128 x 1k	96 min
#3	PRESS ^f	(2 mm) ³	20 ms	256	512	14 min
#3	HOMOGENIZED	5 x 5 x 20 mm ³	60 ms	8	64 x 1k	48 min
#3	HOMOGENIZED	5 x 5 x 20 mm ³	60 ms	4	128 x 1k	48 min

^a Echo time in milliseconds

^b Number of averages

^c Number of digital points acquired

^d Acquisition time in minutes

^e 1k = 1024

^f The repetition time was TR = 2 s

5.3.2 Results

5.3.2.1 CONVENTIONAL MRS

The first precondition for successful *in vivo* PRESS experiments in the rat spinal cord was to provide a homogeneous magnetic field across the investigated voxel. Therefore, shimming was performed on a (3 mm)³ voxel placed inside the spinal cord, avoiding surrounding bone structures. Second-order shimming was not possible because the field correction coefficients calculated by FASTMAP exceeded the maximum available shim power. However, the field homogeneity achieved with first-order shimming was sufficient to acquire spectra with well-resolved lines. A sufficient SNR for spectral fitting and analysis was typically reached in a measurement time of ten to twelve minutes. Figure 5.4 shows a representative *in vivo* PRESS spectrum from a (2 mm)³ voxel positioned inside the shimmed area (see Fig. 5.3). The four

major brain singlet resonances (NAA methyl, Cr methyl and ethyl, and Cho methyl) were identified and fitted for peak integral calculation. Further peaks from J-coupled protons were detectable around 2.7 ppm and 3.5 ppm.

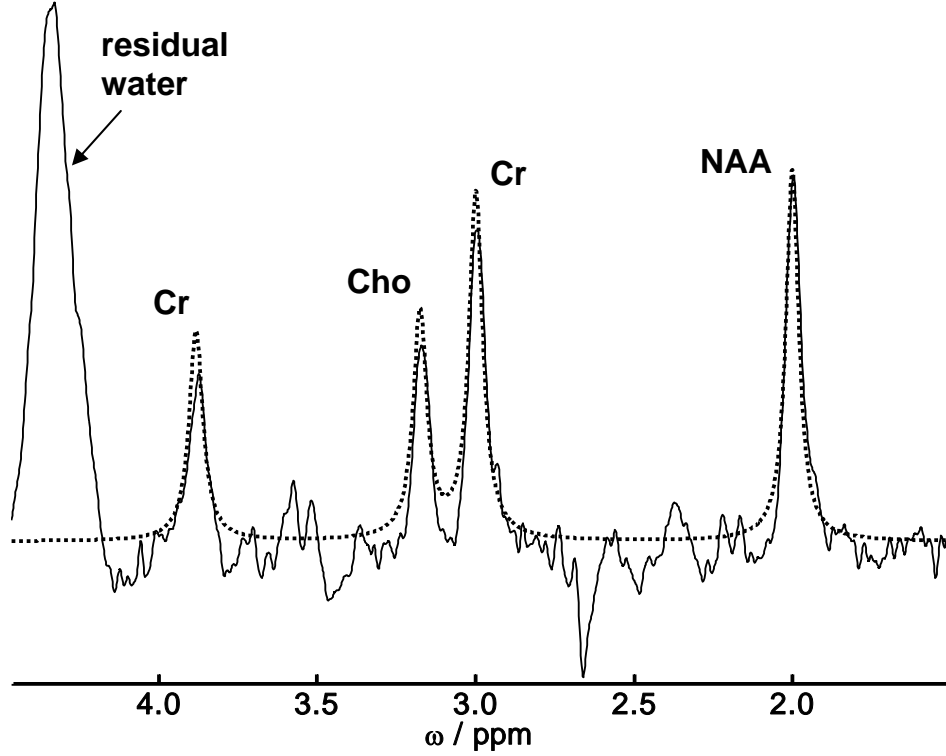


Figure 5.4: In vivo PRESS spectrum of the healthy rat spinal cord (solid line) from a $(2\text{ mm})^3$ voxel as shown in Fig. 5.3. The dotted line shows the fitted spectrum of the four main singlet resonances of spinal cord metabolites, Cr, Cho, NAA. Acquisition parameters were: $TE = 60\text{ ms}$, $NA = 512$, $t_{\text{experiment}} = 45\text{ min}$.

Table 5.2: Experimental parameters, sensitivity and linewidth values for rat #1

Experiment	Voxel ^a	TE	$\text{SNR} / \sqrt{\text{ACQ}}$ ^b	LW_{NAA} ^c
PRESS	8 μl		2.09	37 Hz
	16 μl	60 ms	4.16	40 Hz
	32 μl		5.35	48 Hz
HOMOGENIZED	400 μl	60 ms	1.53	47 Hz

^a Voxel sizes for PRESS differ only in z-dimension

^b SNR efficiency

^c Linewidth of the methyl NAA peak in ω_1

Spectra from voxels elongated by a factor of two or four along the z-direction showed higher SNR efficiency, but also increased linewidths for the NAA resonance (Table 5.2). For the 32 μl voxel, most of which was outside the shimmed region, the gain in SNR efficiency was less than expected from the increase in volume alone. Spectra with different echo times in the same and other animals (Table 5.1) confirmed these observations, which corroborate the idea

that magnetic field homogeneity is crucial for efficient spectroscopy. Taken together, these experiments have shown that localized MRS in the rat spinal cord is feasible at 17.6 T. The required scan times and quality of the obtained spectra suggest that studies quantifying metabolite concentrations may be possible in the future.

5.3.2.2 iZQC SPECTROSCOPY

Due to its inherent lack of susceptibility to variations of the magnetic field, it was possible to acquire iZQC spectra from significantly larger voxels (400 μ l, see Fig. 5.3) than with PRESS. The sequence shown in Fig. 4.14 yielded high quality *in vivo* spectra in all animals, even though the voxel was much larger than the shimmed region in the spinal cord. The four major singlet resonances of brain metabolites could be identified (Fig. 5.5). Line shapes were distorted in the direct dimension, but in the indirect dimension had linewidths comparable to those observed in the PRESS spectra (Table 5.2). Because of the J-modulation and relaxation effects during the long echo time, no signals from J-coupled protons were observed in the iZQC spectra. The calculated peak areas for HOMOGENIZED and PRESS spectra are compared in Table 5.3. The values cannot be compared across different animals, because of differences in the animals ages, season and daytime of the experiment, as well as particular size and position of the voxel. The first two parameters have an effect on the hormonal activity, the third on the specificity of the spectral data. The sole purpose of the presented values is to compare the results obtained with PRESS with those from HOMOGENIZED. While PRESS spectra reflected the expected ratio of 1.5 for Cr methyl to Cr ethyl peaks in all animals, the HOMOGENIZED spectra did not.

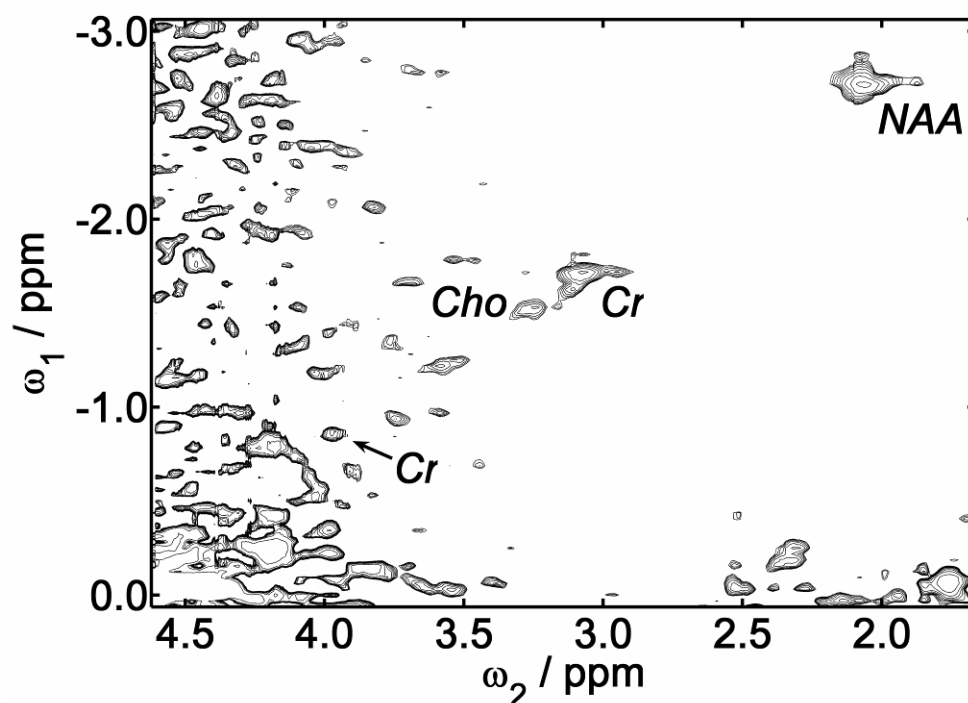


Figure 5.5: *In vivo* HOMOGENIZED spectrum of the healthy rat spinal cord from a 4 x 4 x 25 mm³ voxel as shown in Fig. 5.3. The four main singlet resonances of spinal cord metabolites are labelled.

In particular, peaks closer to the water resonance had smaller peak areas, which was presumably due to more pronounced artifacts in this region. Due to B₁-inhomogeneity towards the edges of the large voxel, water suppression in the iZQC spectra was less efficient

than in PRESS spectra, where the particularly B_1 -insensitive VAPOR presaturation technique was used (135). Along the ω_2 axis in the iZQC spectra, t_1 -noise from residual water signal increased for frequencies close to the water resonance (Fig. 5.5). As a consequence, the Cr ethyl peak could only be identified with prior knowledge of the peak position in the indirect dimension. By contrast, in the PRESS spectrum shown in Fig. 5.4, the residual water signal was only observed in the region for $\omega > 4.2$ ppm. The higher artefact level in the iZQC spectra also resulted in a reduced SNR efficiency (Table 5.2), which was 3 times lower than SNR efficiency of PRESS spectra acquired from the largest voxel. Consequently, long scan times were required with HOMOGENIZED, which led to limited temporal resolution, and rendered the method unsuitable for observing rapid physiological changes.

Table 5.3: Peak integral ratios of the *in vivo* MR spectra in rat spinal cords

Rat	Experiment	Cr – methyl	Cho	Cr – ethyl
#1	PRESS (n = 5) ^a	1.0 ± 0.06	0.53 ± 0.04	0.62 ± 0.04
	HOMOGENIZED	0.83	0.45	0.59
#2	PRESS (n = 3)	1.11 ± 0.22	0.66 ± 0.17	0.74 ± 0.15
	HOMOGENIZED	1.42	0.56	0.66
#3	PRESS	1.45	0.61	0.96
	HOMOGENIZED (n = 2)	1.47 ± 0.02	0.63 ± 0.15	0.72 ± 0.09

^a Different numbers of experiments (n) were performed within one session. Reported ratios were averaged over all experiments. Variations in experimental parameters were assumed to be negligible for averaging.

These results demonstrate that *in vivo* iZQC spectroscopy in the healthy rat spinal cord is possible and provides well-resolved spectra. However, because of the large voxel size, no enhancement in the spectral resolution was observed.

5.4 iZQC MRS in tumors *in vivo* ⁴

The feasibility of acquiring spectra from larger voxels using HOMOGENIZED than it is possible when using conventional methods was investigated in the tumor microenvironment (40). Besides the expected resolution enhancement along the indirect dimension in HOMOGENIZED spectra, the question was addressed, whether, through the potential to operate with bigger voxels, iZQC spectroscopy could acquire spectra with higher SNR than conventional methods in the same experimental time.

⁴ This section contains text and figures adapted from Ref. (40).

5.4.1 Experimental details

The subcutaneous tumor model FaDu, 5–7 mm in diameter, was grown on the thighs of outbred nude mice (Fig. 5.6). FaDu (139) is an established human hypopharyngeal squamous cell carcinoma line, kept in high passage by the American Type Culture Collection (Rockville, MD, USA).

Shimming was done on voxels limited by the anatomical borders of the tumor using FASTMAP (15). HOMOGENIZED spectra were acquired in the same voxel (Fig. 5.6) with the sequence presented in Fig. 4.14. To avoid overlap of the HOMOGENIZED cross-peaks with COSY diagonal peaks (19,20), a frequency offset was applied to the excitation pulse and to the receiver. Raw data was zero-filled by a factor of two in both dimension, a quadratic sine in t_1 and an exponential filter function in t_2 was applied. HOMOGENIZED spectra are presented in magnitude mode. Three different PRESS spectra were acquired from $(6\text{ mm})^3$, $(4\text{ mm})^3$ and $(2\text{ mm})^3$ voxels, respectively. The position of the smallest voxel is illustrated in Fig. 5.6. For data acquisition and processing Paravision 3.0.2 and MATLAB 7.0.1 were used.

The SNR of the magnitude HOMOGENIZED projections and magnitude PRESS spectrum were calculated by dividing the Cho peak integral ($\int S_{\text{Cho}}$) with the standard deviation of a region containing no signal $\sigma(S_{\text{noise}})$. In processing the spectra for SNR comparison no filter functions were applied and the spectral resolution was set equal in HOMOGENIZED (direct dimension) and PRESS. To avoid the positive intensity offset introduced by the magnitude mode, the spectrum was baseline corrected by the mean intensity of the noise region $\langle S_{\text{noise}} \rangle$. Hence, the following expression was used for SNR calculation: $\text{SNR} = \int (S_{\text{Cho}} - \langle S_{\text{noise}} \rangle) / \sigma(S_{\text{noise}} - \langle S_{\text{noise}} \rangle)$.

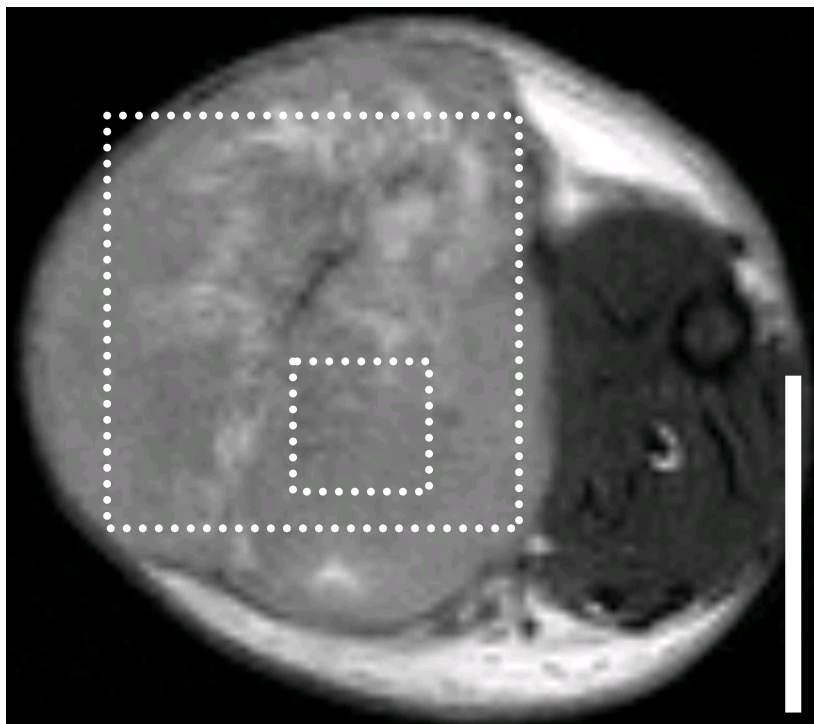


Figure 5.6: Axial fast spin echo image of a FaDu tumor grown in the thigh of a nude mouse. Scale bar: 5 mm. The small square shows the position and size of a $(2\text{ mm})^3$ voxel used for PRESS. The large square indicates the $(6\text{ mm})^3$ voxel used for HOMOGENIZED.

5.4.2 Results

In vivo iZQC spectroscopy experiments were performed in addition to an independent study on the same animal model, where localized spectroscopy (PRESS) was performed on $(2\text{ mm})^3$ voxels because larger voxels did not allow for reproducible high quality spectra. Figure 5.7 shows PRESS spectra from $(2\text{ mm})^3$, $(4\text{ mm})^3$ and $(6\text{ mm})^3$ voxels acquired in 5 minutes each. In the $(2\text{ mm})^3$ voxel, a Cho peak with a linewidth of 85 Hz was observed (Fig. 5.7a). The inhomogeneous structure and small size of the tumor affect the quality of spectra obtained from $(4\text{ mm})^3$ and $(6\text{ mm})^3$ voxels (Fig. 5.7b/c). Localized iZQC spectroscopy is not limited in the size of the selected volume as long as it is inside the anatomical borders of the tumor. Figure 5.8 shows ω_1 -projections of HOMOGENIZED spectra localized to a $(6\text{ mm})^3$ voxel obtained *in vivo* from the same mouse as in Fig. 5.7. Projections were calculated from spectra acquired with 256, 128 and 64 t_1 increments, corresponding to 25 min, 13 min and 7 min acquisition times, respectively. The linewidths of the Cho peak in these spectra were 55 Hz, 110 Hz and 220 Hz, respectively. Spectral quality is not influenced by the large voxel size. Linewidth directly scales with the number of t_1 -increments. SNR is best for the lowest number of increments. The SNR efficiency for the Cho peak in the PRESS (Fig. 5.7a) and the HOMOGENIZED projections in Fig. 5.8 are summarized in Table 5.4.

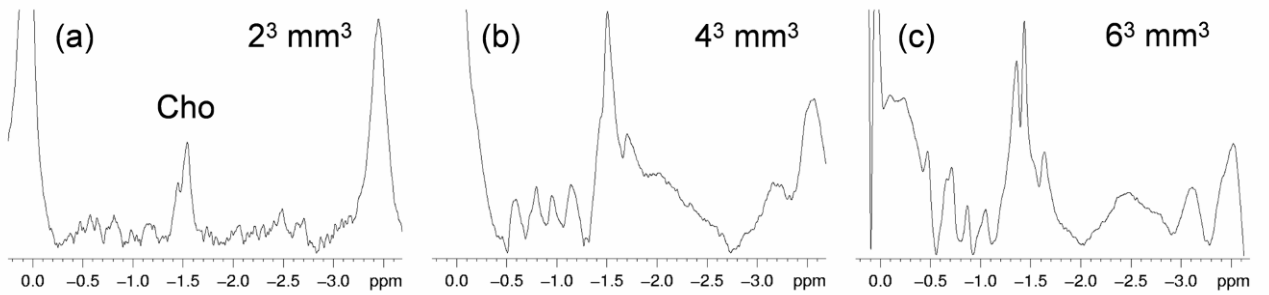


Figure 5.7: *In vivo* PRESS spectra of a FaDu tumor. Voxel size: a.) $(2\text{ mm})^3$, b.) $(4\text{ mm})^3$ and c.) $(6\text{ mm})^3$. $TR = 2\text{ s}$, $TE = 20\text{ ms}$, $TD = 4096$, $SW = 8\text{ ppm}$, 128 averages.

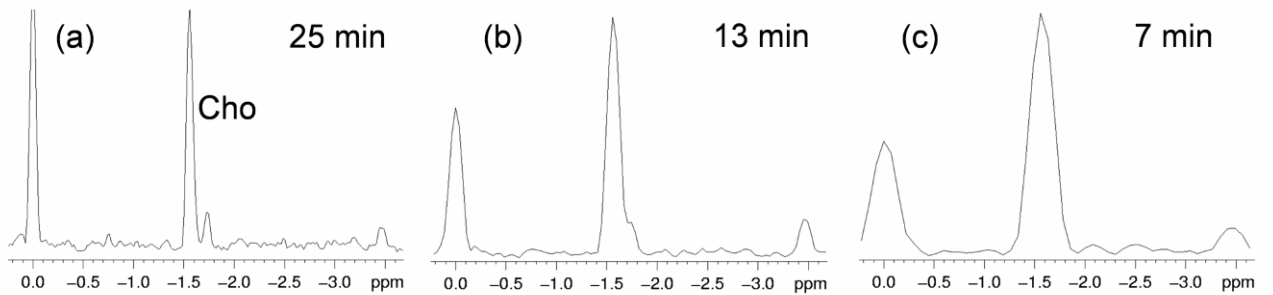


Figure 5.8: Localized *in vivo* iZQC spectra ($(6\text{ mm})^3$ voxel) of a FaDu tumor obtained with the sequence presented in Fig. 4.14. ω_1 -projection of the ω_2 -frequency range -1.3 ppm to -3.7 ppm . $TR = 3\text{ s}$, $TE = 100\text{ ms}$, $TD = 256 \times 1024$, $SW = 10 \times 10\text{ ppm}$, $CG = 16\text{ G/cm} \times 1\text{ ms}$. (a) 256 t_1 increments; (b) 128 t_1 increments; (c) 64 t_1 increments.

The spectra in Fig. 5.8 also illustrate that iZQC techniques provide efficient water and fat suppression. The lipid signal is reduced by two mechanisms. First, signal decay by transverse relaxation is favoured by long echo times used in iZQC techniques. Second, the local nature of the DDF refocusing detectable signal leads to reduction of signal from tissue compartments with high lipid and lower water content (96). From the present data it can not be deduced if

the lipid signal is fully suppressed and the remaining signal at -3.5 ppm originates from lactate.

Table 5.4: SNR efficiency for the HOMOGENIZED projections ((6 mm)³ voxel) presented in Fig. 5.8a-c and the PRESS spectrum ((2 mm)³ voxel) shown in Fig. 5.8a.

	PRESS	HOMOGENIZED 256 t ₁ -incr.	HOMOGENIZED 128 t ₁ -incr.	HOMOGENIZED 64 t ₁ -incr.
SNR per $\sqrt{\text{scantime in minutes}}$	116	79	168	293

Due to the larger voxel size, SNR efficiency of the iZQC experiment is higher by a factor of 1.4 with 128 t₁-increments and a factor of 2.5 higher with 64 t₁-increments, when compared to PRESS.

HOMOGENIZED spectra acquired in less than seven minutes with 64 t₁ increments (Fig. 5.8c) provided higher SNR than PRESS spectra. Obviously, in this spectrum, linewidths were limited by digitization, and spectral resolution was not enhanced compared to PRESS. In HOMOGENIZED spectra acquired with 256 t₁ increments (Fig. 5.8a) lines narrowed, but SNR efficiency was lower than in PRESS, resulting from the required measurement time of 25 minutes. Thus, HOMOGENIZED may be applied *in vivo* either to provide enhanced spectral resolution, or alternatively in large inhomogeneous voxels to provide higher SNR efficiency than conventional methods. However, it is not possible to achieve both resolution and sensitivity enhancement at the same time.

6. iZQC-MRS in presence of local dipole fields

The theory of iZQC-signal refocusing is only understood if the minimum wavelength of inhomogeneities is much longer than a modulation period produced by the correlation gradient. In samples with initially unknown microscopic structure, like biological systems, this condition is hardly granted. Therefore, a clear view on the potential of the technique for future applications requires the investigation of signal refocusing in presence of local dipole fields.

Recently, experimental and numerical investigations have assessed the impact of such local field distortions on image contrast in iMQC-MRI (140,141). Numerical simulations showed that close to a strong perturber, giving rise to local field distortions, signal formation deviates from the desired iMQC behaviour. For iMQC-MRS, this finding raises the question, which degree of magnetic field inhomogeneity imposes an upper limit for resolution enhancement by iMQC detection. In the first part of this chapter⁵, results of extensive numerical simulations and experiments are presented, which assess this limit. The volume ratio $\eta = V_{\text{sample}}/V_{\text{inclusion}}$ of the volume V_{sample} from which the spectrum is acquired and the volume $V_{\text{inclusion}}$ of a spherical inclusion with different magnetic susceptibility, is estimated from simulated spectra and measurements on a model system.

In the second part of the chapter⁶, the question, whether iZQC-MRS can correct for field distortions caused by clustered iron oxide microparticles, is addressed. Iron-oxide microparticles are used for labelling stem cells and making them visible in MR images. They are used in monitoring neuro-regenerative processes and stem cell migration after implantation (128). In this phantom study, the linewidth in conventional single-voxel NMR spectra is compared to the linewidth in HOMOGENIZED spectra along the indirect dimension.

6.1 Maximum local dipole fields for resolution enhancement

6.1.1 Theory

Analytical solutions of the DDF-signal evolution are available for a number of different spin ensembles with the prerequisite of a strong 1D modulation (86). However, significant local dipole fields induced, for instance, by paramagnetic particles or air inclusions, can render these approaches invalid. Here, we consider the case of a binary solution with spin species I and S, in a sample containing the source of a local dipole field at the origin. The local dipole field is created by a spherical volume V of radius R (Fig. 6.1) and susceptibility difference $\Delta\chi$ compared to the surroundings. The resulting dipole field at the external magnetic field B_0 can be written as

⁵ Section 6.1 is an adaptation with ample supplementary material of the article in Ref. (39).

⁶ Section 6.2 contains elements from Ref. (38).

$$B_{\text{dip}}^z(\vec{r}) = B_0 \Delta\chi R^3 \frac{(x^2 + y^2 - 2z^2)}{3|\vec{r}|^5}. \quad [6.1]$$

Transverse components of the static dipole field can be neglected, because their effects are averaged out in the rotating frame in a first order approximation. We analyze signal evolution for a modified HOMOGENIZED sequence as shown in Fig. 6.2.

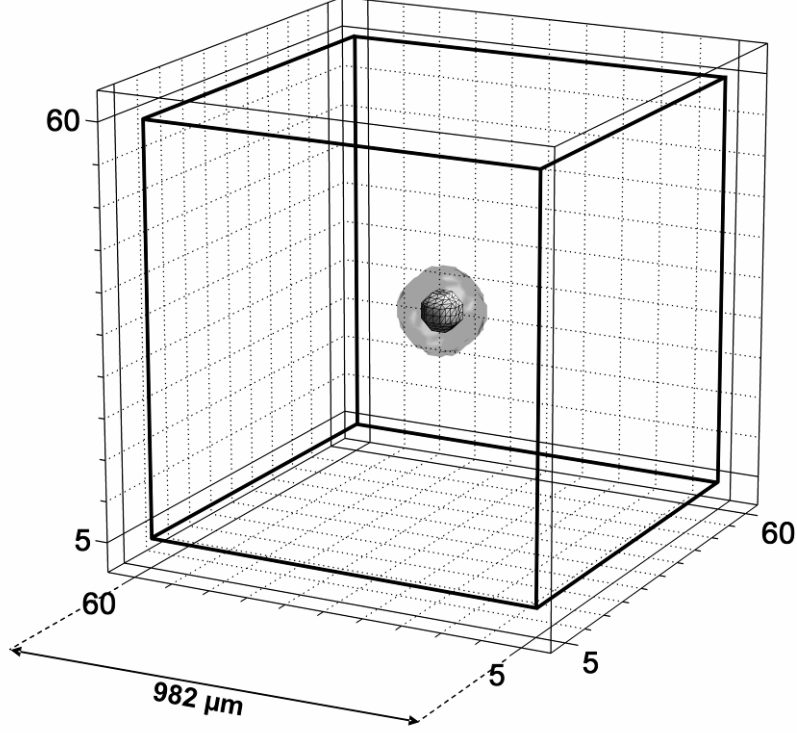


Figure 6.1: Geometrical setup for the simulations: A void spherical inclusion (inner sphere) with a radius of $R = 50 \mu\text{m}$ was placed in the centre of an $(982 \mu\text{m})^3$ isotropic sample cube (bold box). To avoid edge effects, initial magnetization was attributed only to the central 56^3 grid points (minus the inclusion) of a $(1.125 \text{ mm})^3$ cube spanned on a 64^3 element vector array. Different local dipole fields were modelled using different magnetic susceptibility differences $\Delta\chi$ between the inclusion and the surrounding area. Besides the case $B_{\text{dip}} = 0$ ($\Delta\chi = 0$), local dipole fields of glass or air inclusions with $100 \mu\text{m}$ diameter were modelled with $200 \mu\text{m}$ diameter voids (outer sphere) with $\Delta\chi = 0.56 \text{ ppm}$ and $\Delta\chi = 1.16 \text{ ppm}$, respectively. Additionally, the glass sphere was simulated with $\Delta\chi = 4.5 \text{ ppm}$ in a $100 \mu\text{m}$ sphere.

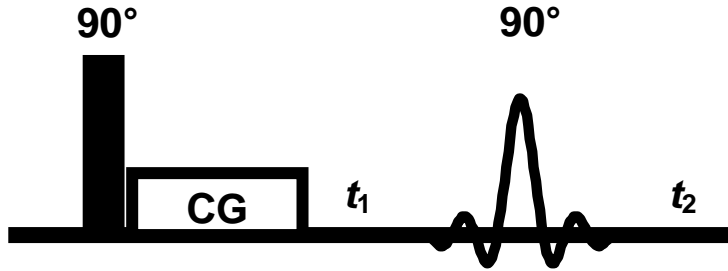


Figure 6.2: iZQC spectroscopy pulse sequence with selective second pulse as used in the simulations. The frequency selective 90° second pulse (sinc shape) acts only on the I (solvent). In simulations both RF-pulses and the CG were applied as operators with duration zero.

During the evolution period t_2 , following the second RF-pulse, signal is formed and evolves under the action of the chemical shift, DDF, and the static dipole field. If relaxation, diffusion, and radiation damping are neglected, the magnetization is described by

$$\begin{aligned} \frac{d\vec{M}(\vec{r}, t_1, t_2)}{dt_2} = & \gamma \vec{M}^I(\vec{r}, t_1, t_2) \times \left[\frac{\Delta\omega_I}{\gamma} \hat{z} + \vec{B}_{DDF}(\vec{r}, t_1, t_2) + B_{dip}^z(\vec{r}) \hat{z} \right] \\ & + \gamma \vec{M}^S(\vec{r}, t_1, t_2) \times \left[\frac{\Delta\omega_S}{\gamma} \hat{z} + \vec{B}_{DDF}(\vec{r}, t_1, t_2) + B_{dip}^z(\vec{r}) \hat{z} \right]. \end{aligned} \quad [6.2]$$

Static dipole fields transform \vec{B}_{DDF} into a non-local function, because B_{dip} imposes a 3D modulation on the magnetization (see the expression of \vec{B}_{DDF} in [3.15]). Writing out the cross product in Eq. [6.2] for each component and using the identities $B_{DDF}^+ = B_{DDF}^x + iB_{DDF}^y$ and $M^+ = M^{S+} + M^{I+}$, evolution of longitudinal and transverse magnetization in t_2 can be written discretely as

$$\begin{aligned} \frac{dM_z(\vec{r}, t_1, t_2)}{dt_2} = & \frac{\gamma}{2} \left\{ M^+(\vec{r}, t_1, t_2) [B_{DDF}^+(\vec{r}, t_1, t_2)]^* \right. \\ & \left. - [M^+(\vec{r}, t_1, t_2)]^* B_{DDF}^+(\vec{r}, t_1, t_2) \right\}, \end{aligned} \quad [6.3]$$

where an asterisk indicates the conjugate transposed, and

$$\begin{aligned} \frac{dM^+(\vec{r}, t_1, t_2)}{dt_2} = & i\gamma \left\{ M_z(\vec{r}, t_1, t_2) B_{DDF}^+(\vec{r}, t_1, t_2) - M^+(\vec{r}, t_1, t_2) [B_{DDF}^z(\vec{r}, t_1, t_2) + B_{dip}^z(\vec{r})] \right\} \\ & - iM^{I+}(\vec{r}, t_1, t_2) \Delta\omega_I - iM^{S+}(\vec{r}, t_1, t_2) \Delta\omega_S. \end{aligned} \quad [6.4]$$

In absence of a local dipole field, $B_{dip} = 0$, the effective DDF becomes a local function in space and is constant in time. An analytical solution for Eq. [6.4] can be found and the detectable signal is given by Eq. [4.5]. In the presence of a significant local dipole field, a generally valid analytical solution for Eq.[6.3] and Eq. [6.4] does not exist. Therefore, these coupled differential equations were solved numerically for three-dimensional Cartesian grids representing different sample geometries and compositions. In the resulting 2D iZQC spectra, the influence and spatial reach of defined local dipole fields on signal formation and linewidths was investigated.

6.1.2 Numerical simulations

6.1.2.1 SIMULATION ALGORITHM

The solution of Eqs. [6.3] and [6.4] requires the calculation of \vec{B}_{DDF} at every time point. Integration of Eq. [3.15] is very time consuming and therefore not efficient. Here, I followed a strategy proposed by Enss et al. (142) and calculated the DDF and the effect of free diffusion

on the magnetization in k -space (142,143). After Fourier transformation, \vec{B}_{DDF} becomes a local function and Eq. [3.15] simplifies to:

$$\vec{B}_{\text{DDF}}(\vec{k}, t_1, t_2) = \frac{\mu_0}{6} \left[3(\hat{k} \cdot \hat{z})^2 - 1 \right] \left[3M_z(\vec{k}, t_1, t_2)\hat{z} - \vec{M}(\vec{k}, t_1, t_2) \right], \quad [6.5]$$

where \vec{k} defines the position in k -space. Inverse Fourier transformation yields $\vec{B}_{\text{DDF}}(\vec{r}, t_1, t_2)$, which then can be used to advance the magnetization vector. The effect of free diffusion in k -space is described by the term

$$\vec{M}_{\text{diff}}(\vec{k}, t_1, t_2) = -D|\vec{k}|^2 \vec{M}(\vec{k}, t_1, t_2), \quad [6.6]$$

which after Fourier transformation is added to the magnetization terms evolved under chemical shift, dipole field perturbation, and the DDF in real space. Relaxation effects were neglected. This approach dramatically accelerates the simulations, because volume integration in Eq. [3.15] is replaced by scalar multiplications in Eqs. [6.5] and [6.6].

The algorithm was implemented and extended for the simulation of 2D iZQC spectra in inhomogeneous fields in MATLAB 7.3.0. The *ode45* differential equation solver was applied, which employs an explicit Runge-Kutta (4,5) formula, the Dormand-Prince pair (144). This one-step solver requires only the immediately preceding time point $\vec{M}(t - dt)$ to calculate the actual value of a function $\vec{M}(t)$.

6.1.2.2 SIMULATION PARAMETERS

The simulations were performed for a $(982 \mu\text{m})^3$ sample cube with the geometry shown in Fig. 6.1. A 4D magnetization array with 64^3 spatial data points represented a $(1.125 \text{ mm})^3$ cube. To avoid boundary artifacts, the outer four layers on all sides of the 56^3 magnetization cube were filled with zeros. The fourth dimension of the array consisted of \vec{M}^{I} and \vec{M}^{S} , representing 110 M on-resonance ($\Delta\omega_{\text{I}} = 0 \text{ Hz}$) water protons (I spins), and 0.1 M off-resonance ($\Delta\omega_{\text{S}} = -250 \text{ Hz}$) metabolite protons (S spins), respectively. To account for the source of the local dipole field, the magnetization was set to zero in a spherical inclusion of $50 \mu\text{m}$ or $100 \mu\text{m}$ radius in the centre of the sample cube (black mesh and grey transparent sphere in Fig. 6.1, respectively).

During the simulation, a magnetization array was iterated for each time step in t_1 and t_2 of the sequence shown in Fig. 6.2. Radio frequency and gradient pulses were applied as operators with zero duration. The second pulse affected \vec{M}^{I} only. The Larmor frequency was set to $\omega_0 = 750 \text{ MHz}$, and the spectral acquisition time was $t_2 = 156 \text{ ms}$. These parameters allowed for 2D spectra with 64×124 digital points, spanning a $800 \times 800 \text{ Hz}$ frequency window. The second spectral dimension was obtained by repeatedly solving the time domain evolution in t_2 for incremented t_1 periods. The correlation gradient strength was $\text{CG} = 16.4 \text{ G/cm}$, generating seven full modulations in longitudinal direction over the sample (eight over the full array) with eight magnetization grid points per modulation period. To eliminate signal from unwanted coherences, a phase cycle was implemented by adding the results of two simulations with opposite excitation pulse phase ($x, -x$) for each t_1 increment.

The simulation program was executed on a multiprocessor compute server equipped with four single core Opteron 800-series processors (2.4 GHz) with 64-bit architecture, a 64-bit operating system, and 48 gigabytes random access memory. A total of six different simulations were performed for this study. Each produced a six dimensional $M^+ \propto M^+(M^{IVS}, t_1, t_2, x, y, z)$ array that was stored in a 62 gigabyte dataset. Three simulations were performed with $B_{dip} = 0$. Simulation SIM1 used a homogeneous 56^3 magnetization cube without inclusion. Edge effects were assessed in simulations SIM2 and SIM3, in which a central sphere of 50 μm and 100 μm radius, respectively, was set to zero. For simulation SIM4, a local dipole field was modeled by setting the proton magnetization to zero and adjusting the magnetic susceptibility difference, relative to the surrounding water, to $\Delta\chi = 4.5 \cdot 10^{-6}$ within a central sphere of $R = 50 \mu\text{m}$. For simulation SIM5, a local dipole field was modeled by setting the magnetization to zero and the susceptibility difference to $\Delta\chi = 0.56 \cdot 10^{-6}$ within an inclusion of $R = 100 \mu\text{m}$. In the region of the sample cube, which was analyzed (outside the inner sphere with $R = 100 \mu\text{m}$), the resulting local dipole fields were identical for SIM4 and SIM5, both modeling the field of a central glass sphere with $R = 50 \mu\text{m}$. A spherical air inclusion was simulated in SIM6 by setting $\Delta\chi = 1.16 \cdot 10^{-6}$ within a central sphere with 100 μm radius. The required CPU times for the simulations were approximately 520 hours for SIM1, SIM2, and SIM3, 1800 hours for SIM4, 600 hours for SIM5, and 700 hours for SIM6.

6.1.2.3 ANALYSIS OF THE SPECTRA

2D HOMOGENIZED spectra were calculated for each of the 56^3 grid points by Fourier transformation of $M^+(t_1, t_2)$. Spectra were analyzed for the whole sample cube and for different regions with respect to dependence on the distance from the inclusion. To this end, M^+ was summed over grid points within four different regions, roughly modeling spherical shells of approximately 100 μm thickness (see sketches in Fig. 6.3). Due to the coarse digital resolution of 17.86 μm along the cube axes, individual shells comprised a maximum of five or six digital points across the shell, corresponding to a thickness of 71 μm or 89 μm , respectively. Along oblique directions, the grid points had larger distances leading to angle-dependent values of grid points per shell and thickness of the shell. Measured from the center of the cube, the shells were arranged as follows: spherical inclusion: six grid points along the axes (0-107 μm); shell 1: five grid points along the axes (125-196 μm), 4156 points in total; shell 2: six grid points along the axes (214-304 μm), 13326 points in total; shell 3: five grid points along the axes (321-393 μm), 20068 points in total; shell 4: six grid points along the axes (411-500 μm), 41082 points in total. To assess the detection limit, η_{limit} , defined as the minimum cube size-inclusion ratio that allowed for detection of the metabolite peak, was determined. Subsequently, spectra were calculated for different magnetization cube sizes by reducing the cube size step by step along all three spatial dimensions. The metabolite peak was designated as detectable, if its maximum intensity (measured in an area of 7 x 7 spectral points around the theoretical peak position) was at least eight times the mean intensity and more than twice the maximum intensity of the surrounding area of 21 x 21 spectral points. Spectral linewidths at half maximum were determined from 1D traces cutting the 2D peak at maximum intensity. Where needed, sub-digital resolution was achieved by linear interpolation.

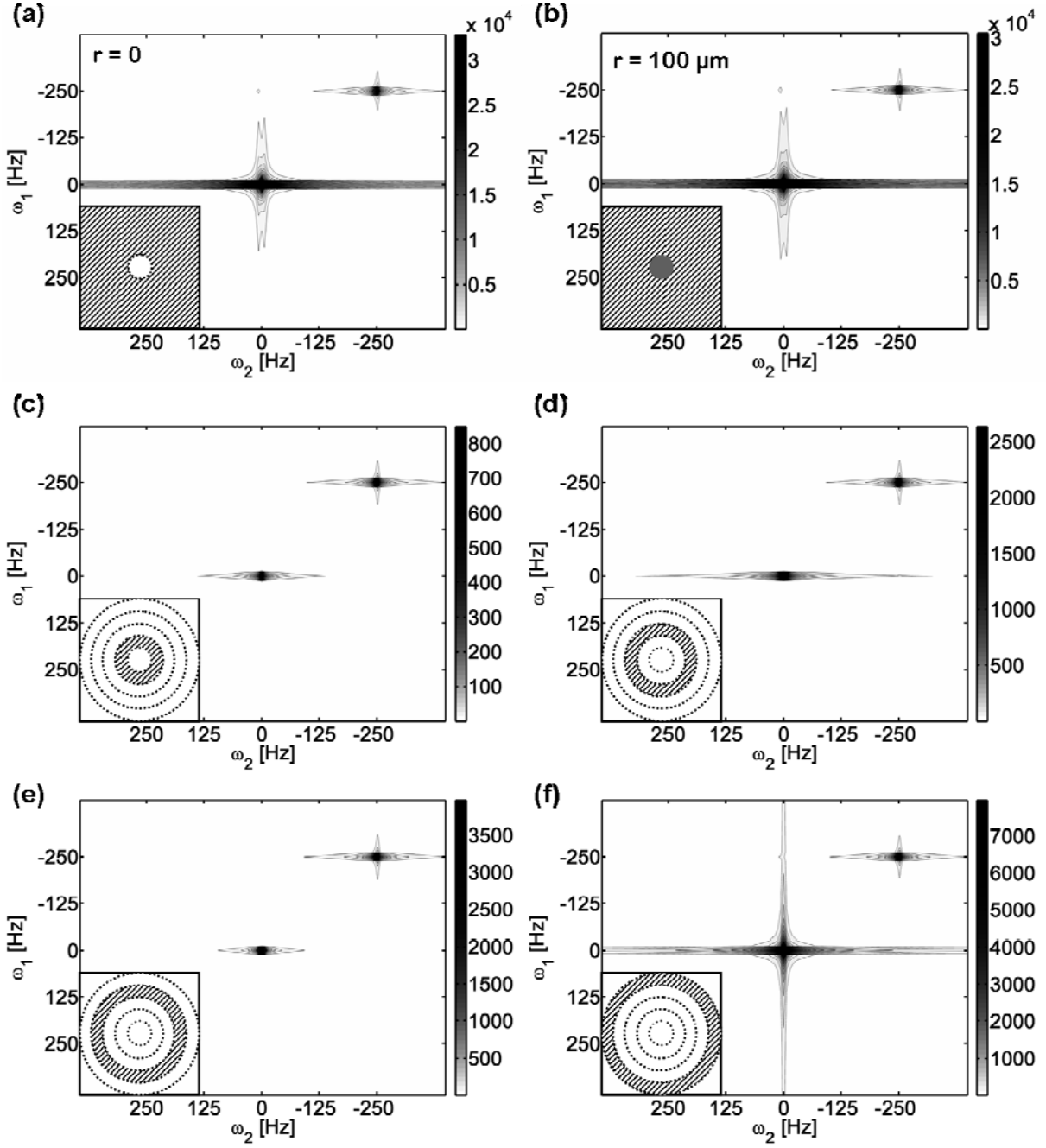
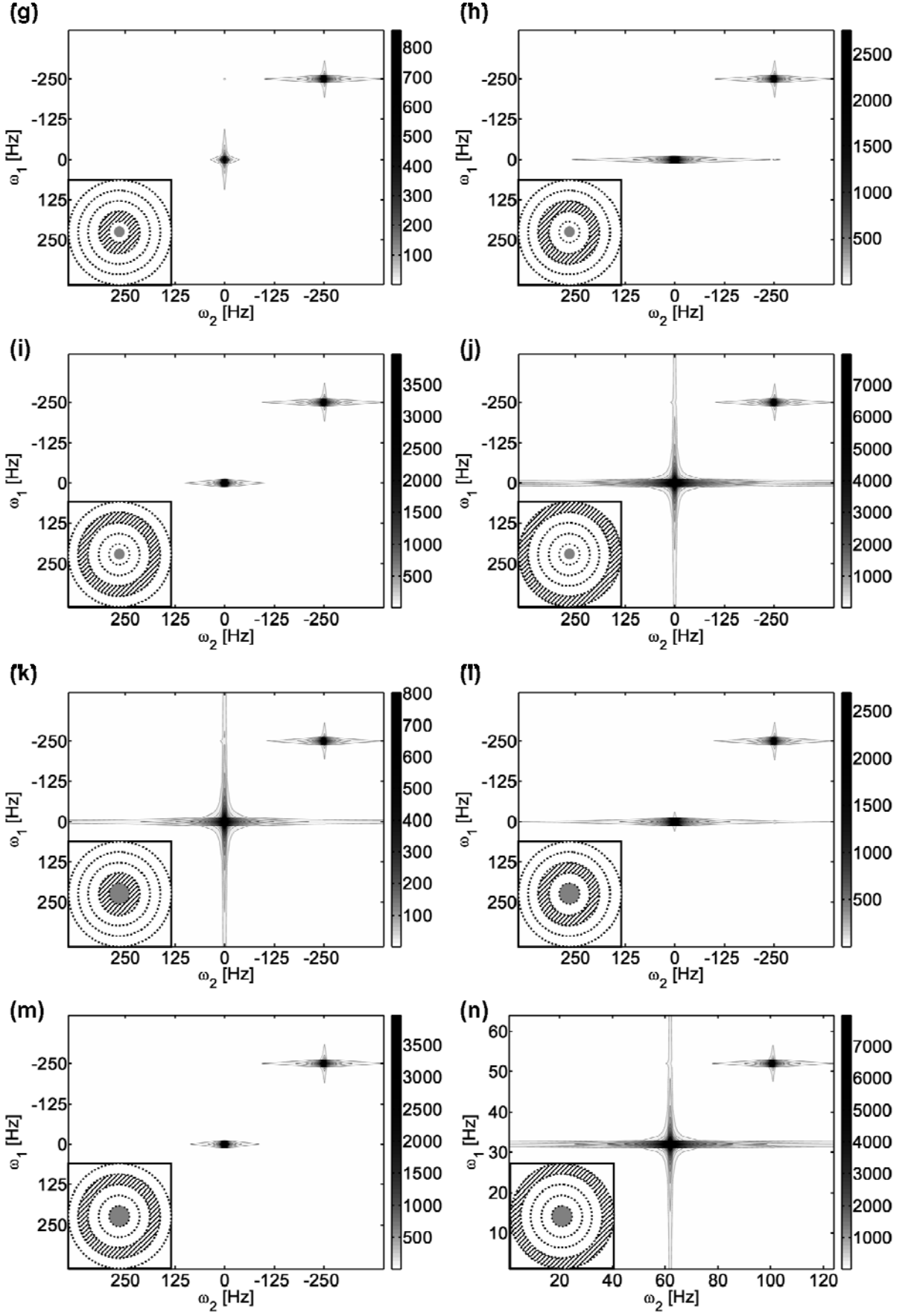


Figure 6.3: Simulated iZQC spectra without local dipole field ($B_{dip} = 0$). The presented spectra were summed over the regions indicated by hatched areas in the insets. Gray circle indicates the area where magnetization was set to zero in the simulations. (a) Full spectrum summed over a whole sample cube except the central $200 \mu\text{m}$ sphere. Simulation was performed for a homogeneous magnetization over the whole cube (no inclusion). (b) Full spectrum for a simulation where the magnetization in the central sphere with $r = 100 \mu\text{m}$ was set to zero. (c-f) Spectra from the simulation shown in (a), but summed only over the shells indicated in the inset, $125\text{-}196 \mu\text{m}$ in (c), $214\text{-}304 \mu\text{m}$ in (d), $321\text{-}393 \mu\text{m}$ in (e), and $411\text{-}500 \mu\text{m}$ in (f). (g-n) Shell specific spectra for $r = 50 \mu\text{m}$ (g-j) and $r = 100 \mu\text{m}$ (k-n). Scale bars in arbitrary intensity units.



6.1.2.4 VALIDITY ASSESSMENT

The simulation program was employed for the case of a homogeneous sample cube ($B_{\text{dip}} = 0$) with a binary mixture of solvent I spins and solute S spins, to verify the outcome in comparison to theoretical predictions. This first run, SIM1, resulted in the spectrum presented in Fig. 6.3a. A cross-peak at $(\Delta\omega_S - \Delta\omega_I, \Delta\omega_S)$ can be observed, as predicted by the analytical solution of the modified Bloch-equations for this setup (Eq. [4.5]). The peak at $(0, \Delta\omega_I)$ is not predicted by the theory, yet it corresponds to previous experimental findings in homogeneous samples (see Fig. 4.2) (29,37). Both in simulations and experiments, the unexpected peak arises because the approximation, that the magnetization is modulated in one defined direction (here z-direction), does not hold any more. Equation [4.5] fails to describe the DDF-signal in such case. However, whereas the reasons for this effect in measured spectra were, presumably, experimental imperfections and relaxation effects, the deviation in the simulations can not be caused by the same factors.

Table 6.1: Peak intensities and linewidths of the solvent (I spins) and solute (S spins) peaks in the simulated spectra for validity assessment. Values are given summed over the whole sample cube, and summed over the individual shells (Shell 1: 125-196 μm , Shell 2: 214-304 μm , Shell 3: 321-393 μm , and Shell 4: 411-500 μm).

	I – peak intensity	S – peak intensity	I / S peak ratio	S – peak width in ω_1	S – peak width in ω_2
SIM1. R = 0 μm , $\Delta\chi = 0$					
Full sample	756440	50038	15	12 Hz	8 Hz
Shell 1	2210	1374	2	12 Hz	8 Hz
Shell 2	17152	4409	4	12 Hz	8 Hz
Shell 3	11106	6634	2	12 Hz	8 Hz
Shell 4	63641	13015	5	12 Hz	8 Hz
SIM2. R = 50 μm , $\Delta\chi = 0$					
Full sample	756650	49932	15	12 Hz	8 Hz
Shell 1	991	1372	0.7	12 Hz	8 Hz
Shell 2	16544	4406	4	12 Hz	8 Hz
Shell 3	11544	6631	2	12 Hz	8 Hz
Shell 4	63778	13008	5	12 Hz	8 Hz
SIM3. R = 100 μm , $\Delta\chi = 0$					
Full sample	763040	49538	15	12 Hz	8 Hz
Shell 1	5620	1292	4	12 Hz	8 Hz
Shell 2	18885	4405	4	12 Hz	8 Hz
Shell 3	10712	6627	2	12 Hz	8 Hz
Shell 4	63791	13000	5	12 Hz	8 Hz

One possible explanation for the appearance of the relatively high solvent peak at $(0, \Delta\omega_I)$ (Table 6.1) is the effect of the sharp transition to zero at the edges of the magnetization cube. To verify this, the spatial distribution of the signal was analyzed by reconstructing additional spectra from four non-overlapping shells of a sphere touching the inner walls of the magnetization cube (Fig. 6.3 c-f). The I/S peak ratios in the first block of Table 6.1 indicate, that the solvent peak intensity was increased in the spectrum from the whole cube including the surface, in contrast to spectra from single shells, where only the outer shell touches the

surface in a total of six points. Thus, the unwanted effect is local and affects only peripheral sample regions. Considering, that the I/S concentration ratio is higher than 1000, the I/S peak ratio of 15 is tolerable (Table 6.1). However, sample geometry for the simulation of inhomogeneity effects is not an isotropic magnetization cube (Fig. 6.1). By setting magnetization values in the centre of the cube to zero, a new source of edge effect is created. Two further validation simulations were performed with $B_{\text{dip}} = 0$: SIM2 with a central void of 100 μm (Fig. 6.3g-j), and SIM3 with 200 μm diameters (Fig. 6.3k-n). It turned out, that a central void affects only the signal of the innermost shell moderately (Table 6.1). Linewidths of the solute peak in the validation spectra were constant both along ω_1 (12 Hz) and ω_2 (8 Hz). This means that edge effects do not influence the spectral lineshape (Fig. 6.4) within the limits of the digital resolution afforded by the simulation.

The last criterion of validation was the expected signal intensity loss with the reduction of sample volume. To check this, the signal was integrated over reduced magnetization cubes around the centre. Starting at the surface a total of 28 equal digital steps were taken until the centre of the sample cube was reached, resulting in 28 spectra after Fourier-transformation. The traces through the cross-peak in these spectra, presented in Fig. 6.4 for SIM1, demonstrate the expected intensity loss. Thereby, the lineshape of the cross-peak remains unaffected.

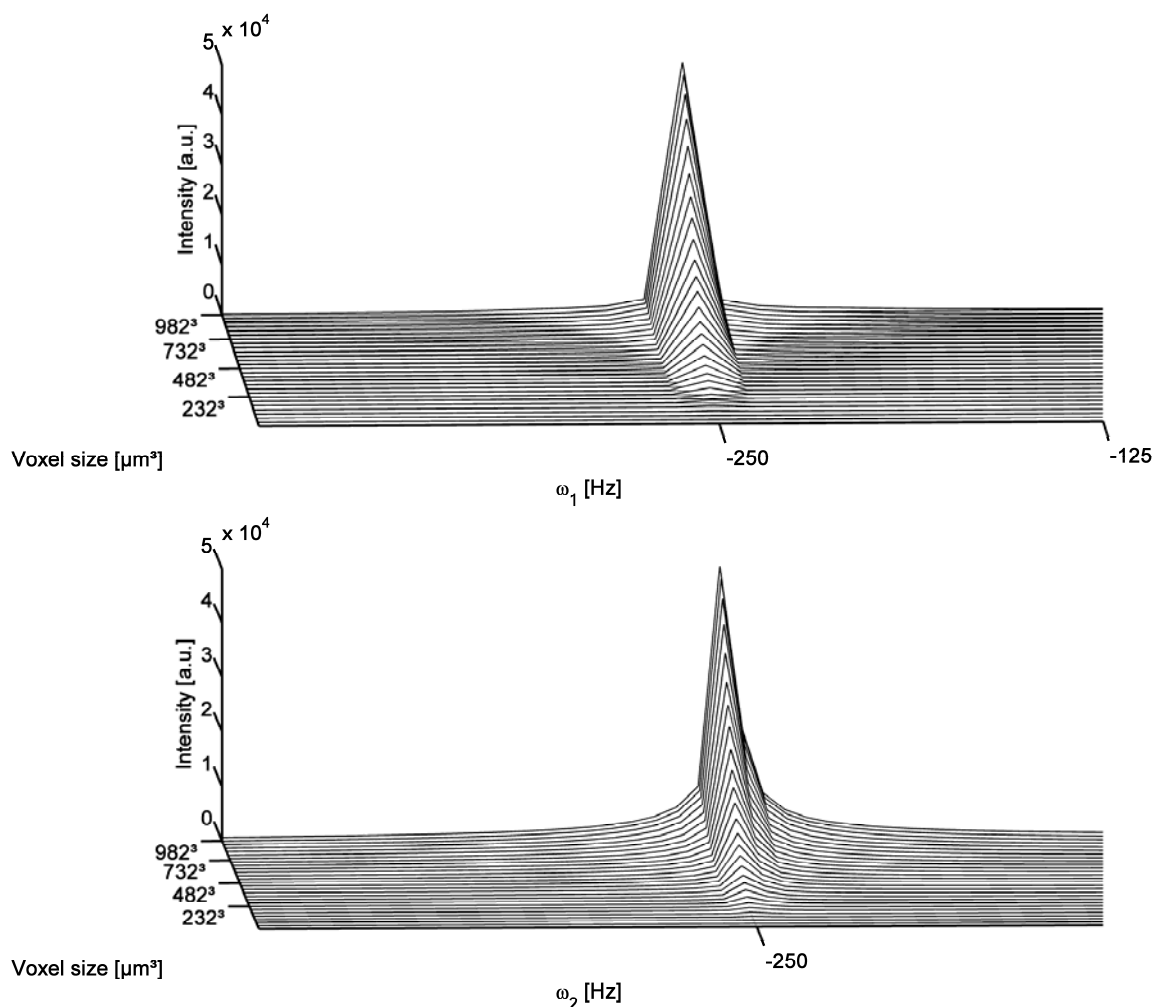


Figure 6.4: Simulated cross-peak intensity dependence on the voxel size. Traces along the indirect (top) and direct (bottom) axes through the cross-peak of the full spectrum calculated with SIM1. The spectral line shape of the S-peak remains unaltered in both dimensions.

6.1.2.5 TOLERANCE OF DIGITIZATION ERROR IN SIMULATIONS

Digitization errors can impair the accuracy of a simulation if Nyquists' theorem is not fulfilled. To avoid these errors a minimum of four data-points should be sampled in each modulation period. This condition was fulfilled in case of $B_{\text{dip}} = 0$, because the gradient strength (Fig. 6.2) was chosen so as to cause eight full modulations in z-direction over 64 grid-points. This resulted in a sampling rate of eight points per period. However, a non-zero local dipole field imposed another modulation with a non-periodic spatial distribution (Eq. [6.1]), which close to the source had a very high frequency and could possibly cause incomplete sampling of the strong modulation. Therefore, it had to be analyzed if and under which circumstances the simulations violate the Nyquist-limit for the digital sampling rate.

The decisive parameter for the maximum intensity of the dipole field is the susceptibility difference of the source to that of the medium ($\Delta\chi$). The characteristic spatial distribution depends on the second order Legendre polynomial with the cosine of the azimuth angle as parameter ($3\cos^2\theta - 1$). Therefore, the imposed modulation is strongest along z, and vanishes along the magic angle ($\pm 54.7^\circ$). In addition, the intensity of B_{dip} is a function of r^{-3} , and thus decreases fast with the distance from the dipole source. The dipole field is constant in time and acts on the transversal magnetization during the t_1 evolution period. Therefore, its effect is enhanced for longer t_1 periods, for decreasing distance to the source, for large susceptibility differences (e.g. air bubble in water), and is strongest along the z-axis. Figure 6.5 shows the spatial distribution and t_1 -dependence of the Nyquist-limit for the dipole perturbation in case of SIM6 (air bubble). Contour lines in the coordinate system built by the distance and azimuth angle axes depict the regions with digitization errors. Shell1 is indicated by vertical dashed lines to emphasize that only this region is affected by undersampling. In Shell2 the limit is exceeded only for the last few t_1 -increments in SIM6. In case of simulations for a glass inclusion SIM4 and SIM5 the Nyquist criterion holds everywhere in the sample, excluding a fraction of the inner-most shell.

In undersampled regions the calculated magnetization dynamics was only a coarse approximation, because the inhomogeneous relaxation effects were underestimated. Yet, the error was localized to a small sample region and a few t_1 -increments (Fig. 6.5). It has to be emphasized, that Shell1 includes ten times less grid-points than Shell4, less than Shell2 or Shell3, and far less than the whole sample cube (see Sec. 6.1.2.3). Contributing peak amplitudes from the inner-most shell were substantially smaller than from the other shells (see Table 6.2). Therefore, the signal integrated over the whole cube, or even just a part of it, was not significantly modified by the deviation in a few grid points in Shell1. This was reflected in the results obtained for the two simulation of the dipole field introduced by a glass sphere with 50 μm radius. SIM4 modelled the sample with the actual geometry and a susceptibility of $\Delta\chi = 4.5$ ppm (Fig. 6.6a), and SIM5 used a sphere with 100 μm radius and $\Delta\chi = 0.56$ ppm (Fig. 6.6b). Only small deviations in peak amplitudes and nearly identical effects on line broadening were observed in the respective spectra (Table 6.2). Differences in both spectra resulted mainly from edge effects and numerical errors. On one hand, SIM5 is affected by edge effects discussed in the previous section. On the other hand, SIM4 cruelly violated the Nyquist-limit in the neighbourhood of the smaller but much stronger dipole than SIM5. Although these errors may compromise the accuracy of the simulation to some degree, they are not substantial and the simulation can be used to estimate order of magnitude effects induced by local dipole fields.

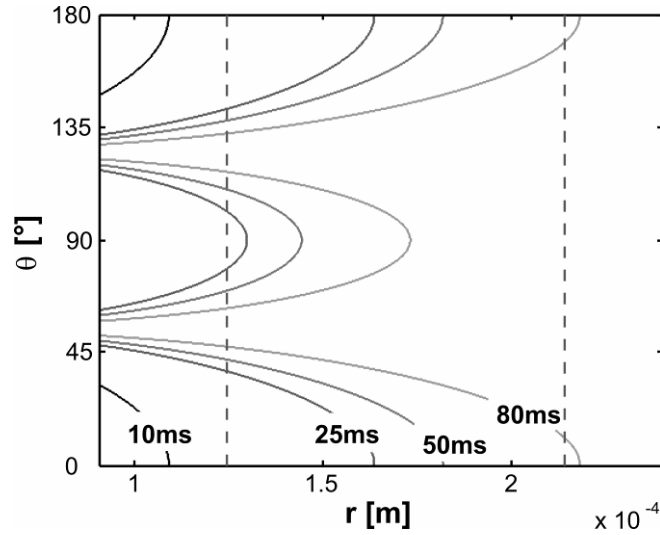


Figure 6.5: The Nyquist limit in the simulations. The regions of the sample cube, where the spatial Nyquist frequency was violated in the simulation SIM6, are shown left to the plotted curves as function of the polar coordinates θ and r . Since spatial modulation of the magnetization increases with t_1 , the regions grow for longer t_1 . Curves are shown for four representative t_1 values (labels). Affected regions are almost completely limited to the first analyzed shell (125 – 196 μm) as indicated by the vertical lines. Note that only a small fraction of the whole sample cube is shown along the r -axis.

Table 6.2: Peak intensities and linewidths of the solvent (I spins) and solute (S spins) peaks in the simulated spectra including the effect of a local dipole field.

	I – peak intensity	S – peak intensity	I / S peak ratio	S – peak width in ω_1	S – peak width in ω_2
SIM4. $R = 50 \mu\text{m}$, $\Delta\chi = 4.5 \text{ ppm}$					
Full sample	461620	20366	23	12 Hz	9 Hz
Shell 1	9167	5	1833	47 Hz	20 Hz
Shell 2	190300	300	634	20 Hz	9 Hz
Shell 3	193650	1718	113	12 Hz	9 Hz
Shell 4	250070	5903	42	12 Hz	8 Hz
SIM5. $R = 100 \mu\text{m}$, $\Delta\chi = 0.56 \text{ ppm}$					
Full sample	462140	23931	19	12 Hz	8 Hz
Shell 1	9269	6	1545	47 Hz	20 Hz
Shell 2	190870	328	582	20 Hz	9 Hz
Shell 3	193540	1832	107	12 Hz	11 Hz
Shell 4	248730	6865	36	12 Hz	8 Hz
SIM6. $R = 100 \mu\text{m}$, $\Delta\chi = 1.16 \text{ ppm}$					
Full sample	744740	12886	58	12 Hz	8 Hz
Shell 1	3624	5	725	96 Hz	17 Hz
Shell 2	87034	108	806	41 Hz	15 Hz
Shell 3	223070	770	290	12 Hz	14 Hz
Shell 4	410310	3335	123	12 Hz	9 Hz

6.1.2.6 RESULTS: THE IMPACT OF B_{DIP} ON LINEWIDTHS AND PEAK INTENSITIES

The effect of dipole perturbation on the spectra can be observed in Fig. 6.6 for the case of SIM4, SIM5 and SIM6. The solvent peak is substantially broadened in both dimensions, yet the effect is stronger in ω_2 . Line broadening of the cross-peak is not significant (Table 6.2). However, the absolute cross-peak intensity is decreased by a factor of 2.5 (see also Fig. 6.7 in comparison with Fig. 6.4), whereas the effect is weaker for the solvent peak (Table 6.2). Figure 6.7 clearly shows that by reducing the volume around the dipole source, the dominant effect is a decrease in cross-peak intensity and not increasing line broadening.

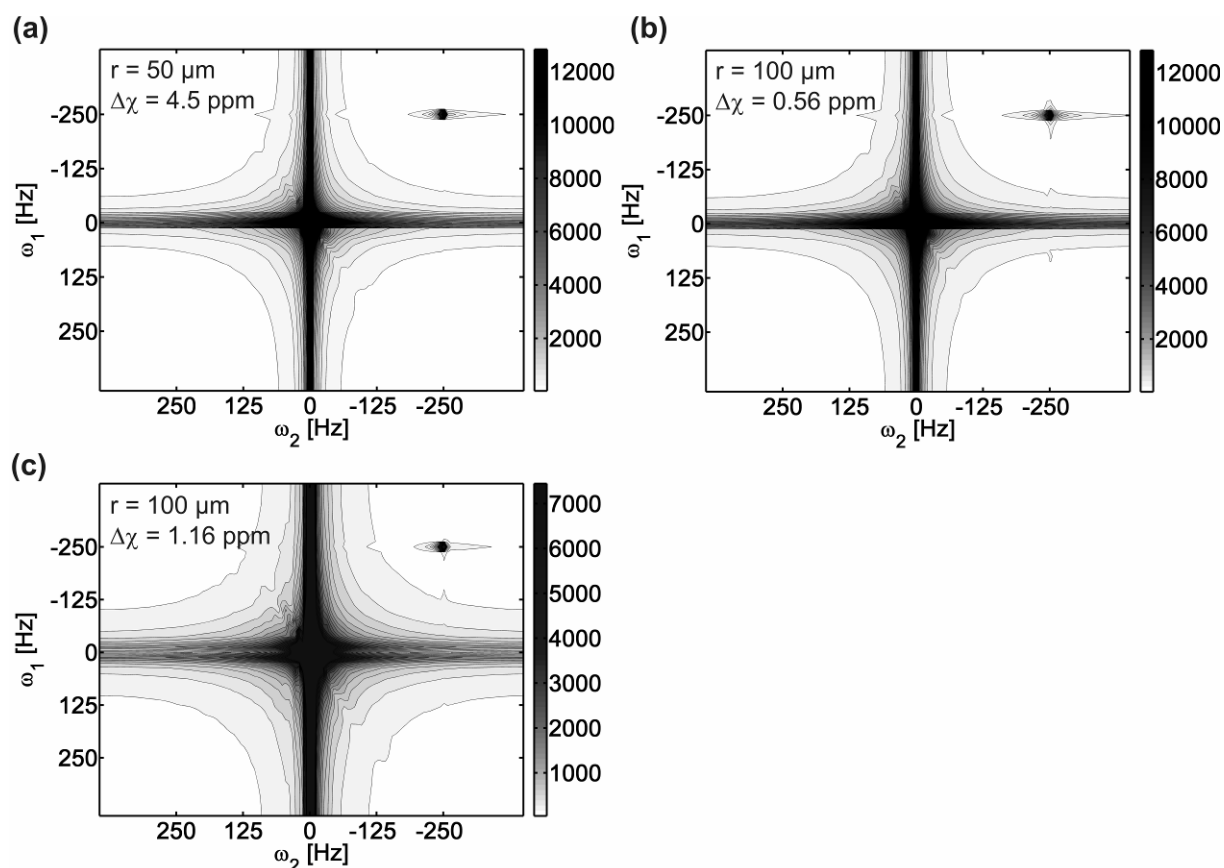


Figure 6.6: Simulated iZQC spectra from samples modelling different sources of local dipole fields, summed over the whole sample cube. (a) Glass sphere with $R = 50 \mu\text{m}$ and $\Delta\chi = 4.5 \text{ ppm}$. (b) Sphere with $R = 100 \mu\text{m}$ and $\Delta\chi = 0.56 \text{ ppm}$ giving rise to the same local field as in (a). (c) Sphere with $R = 100 \mu\text{m}$ and $\Delta\chi = 1.16 \text{ ppm}$ modelling the local field of an air bubble with $r = 50 \mu\text{m}$ and $\Delta\chi = 9.3 \text{ ppm}$. Scale bars in arbitrary intensity units. Note the different intensity scales.

Let us consider Table 6.2 and Fig. 6.8 with the shell-specific traces through the cross-peak for SIM4. The broadening effect of the dipole perturbation was strongest in the inner-most shell, producing pseudo-noise in the simulated spectra surrounding the water resonance within a range of about 125 Hz for the glass simulations, and about 200 Hz for the air simulation. Similarly, broadening of the S peak was the most severe in Shell1. Although the coarse digital resolution denied an exact determination of linewidths, the data in Table 6.2 shows that the broadening of the cross-peak was more pronounced along ω_1 than along ω_2 . This observation seems to contradict the line narrowing properties of iZQC spectra.

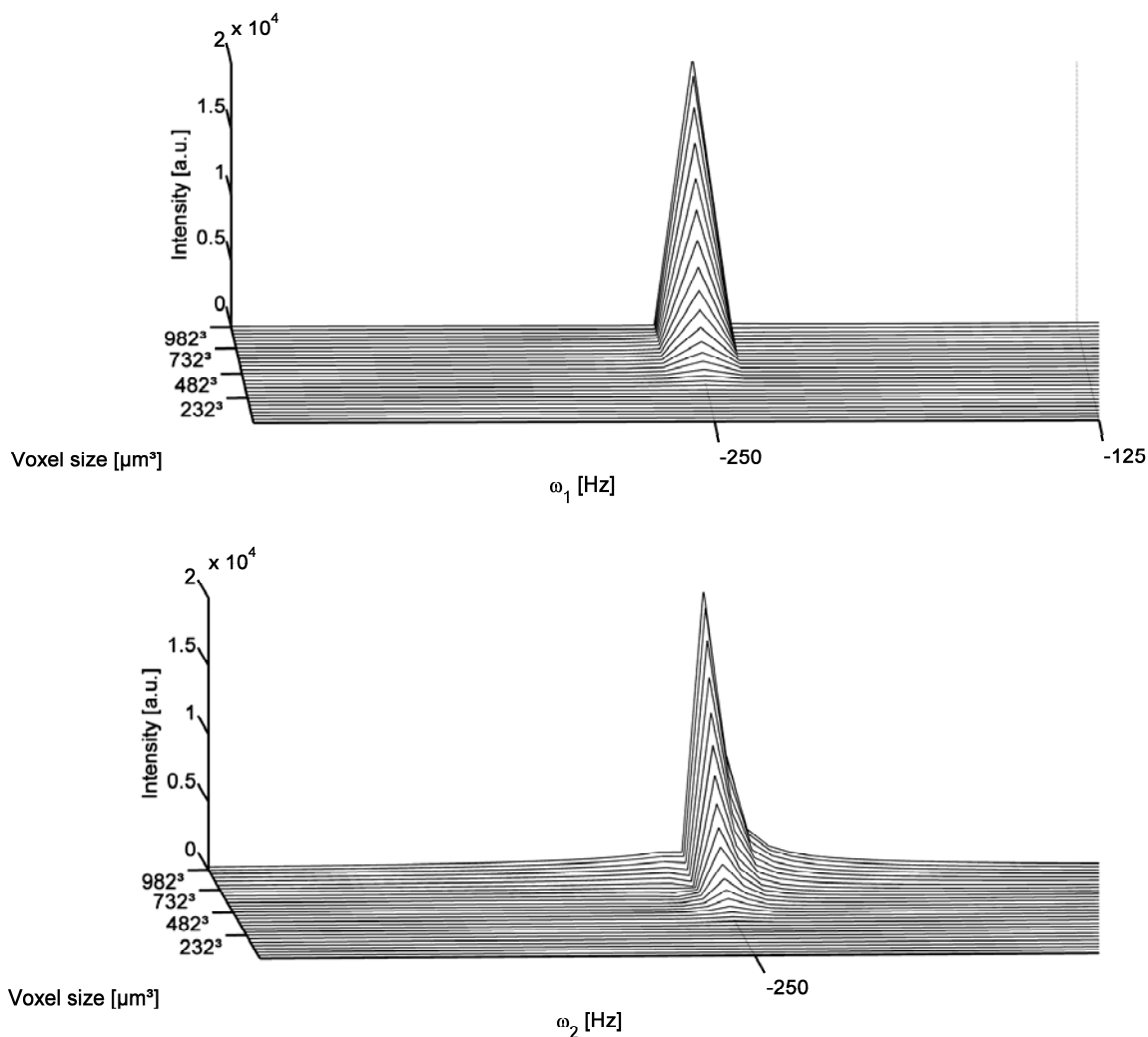


Figure 6.7: Cross-peak intensity profiles in inhomogeneous magnetic field (glass inclusion) as a function of the voxel size. Traces along the indirect (top) and direct (bottom) axes through the cross-peak of the full spectrum calculated with SIM4.

However, the line narrowing property of iZQC spectroscopy is based on the premise that the static B_0 field variation, the local inhomogeneity, is negligible compared to the 1D gradient modulation (see Sec. 3.3). For resolution enhancement, the correlation gradient must be significantly stronger than the dipole perturbation everywhere in the sample. This condition was not fulfilled in the region near the non-zero dipole sources, in Shell1 and Shell2. Although traces through the maximum of the solvent peak are not shown in Fig. 6.8, the line shapes of the pseudo noise and the relative intensities to the cross-peak maximum clearly indicate that spectral quality and relative cross-peak intensity increase with the distance from the inhomogeneity source. This result is confirmed by the shell-specific 2D spectra from the simulated data in SIM6 (Fig. 6.9). Distortion of spectral patterns and of their proportions is illustrated for the strongest dipole source (air bubble). In the inner-most shell, no defined peak was observed (Fig. 6.9a). In the second shell only a weak and still broadened peak was seen (Fig. 6.9b). Both signal amplitudes at the expected peak position were nearly three orders of magnitude smaller than the solvent signal. In both outer shells the peak was hardly broadened and peak amplitude was substantially higher (Fig. 6.9c,d). The largest signal contribution was obtained from those parts of the sample where the local dipole field was weakest. Consequently, for the spectrum from the whole sample cube, the S peak amplitude amounted to 1/58 of the I peak amplitude and no line broadening was observed within the available digital resolution.

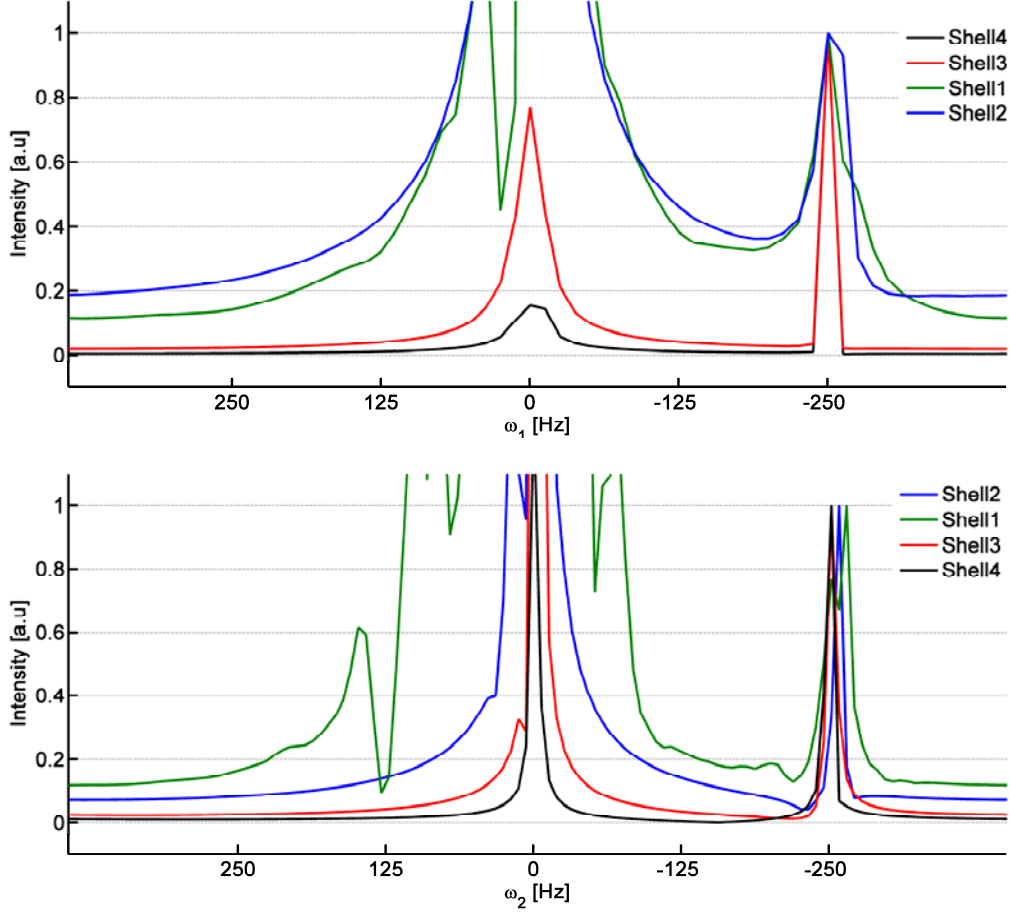


Figure 6.8: *Traces through cross-peak maxima in spectra from the four different shells in the magnetization cube simulated for a glass dipole source (SIM4). Each trace was separately normalized on the cross-peak maximum intensity to enable comparable visualization of the shell-specific line broadening and to emphasize relative amplitude changes. It should be pointed out that absolute intensities increase dramatically with the distance to the dipole source because of the reduction of grid points in the inner shells and also because of the dipole perturbation effect.*

Similarly to the discrete magnetization vectors in the simulated 3D grid, each spin in a real sample interacts within the correlation length with other spins with a broad range of relative frequency differences. This frequency distribution is broader, when approaching an inhomogeneity source. As described in Sec. 6.1.2.5, digitization errors may deny a quantitatively exact analysis in the central regions, but spin dynamics is accurately modelled and the shell-specific treatment can give an insight into the physical process behind the effects. Thus, it can be concluded that the frequency distribution within the correlation length reduces the amplitude of the locally refocused magnetization and causes line broadening along the indirect dimension.

These results suggest that the sample-volume to dipole source volume ratio is an important quality criterion for iZQC-spectra. Considering Fig 6.4 and Fig. 6.7, it becomes obvious that there is a minimum volume fraction η_{limit} , from which a cross-peak in an iZQC-spectrum can be detected. The comparison of Fig. 6.4 and Fig. 6.7 also indicates that η_{limit} depends on $\Delta\chi$. The intensity data in Tables 6.1 and 6.2 show that the simulated cross-peak amplitude was halved in case of a glass dipole source, and reduced by a factor of 75 % for an air bubble. η_{limit} must, therefore, be calculated for each type of inhomogeneity source individually.

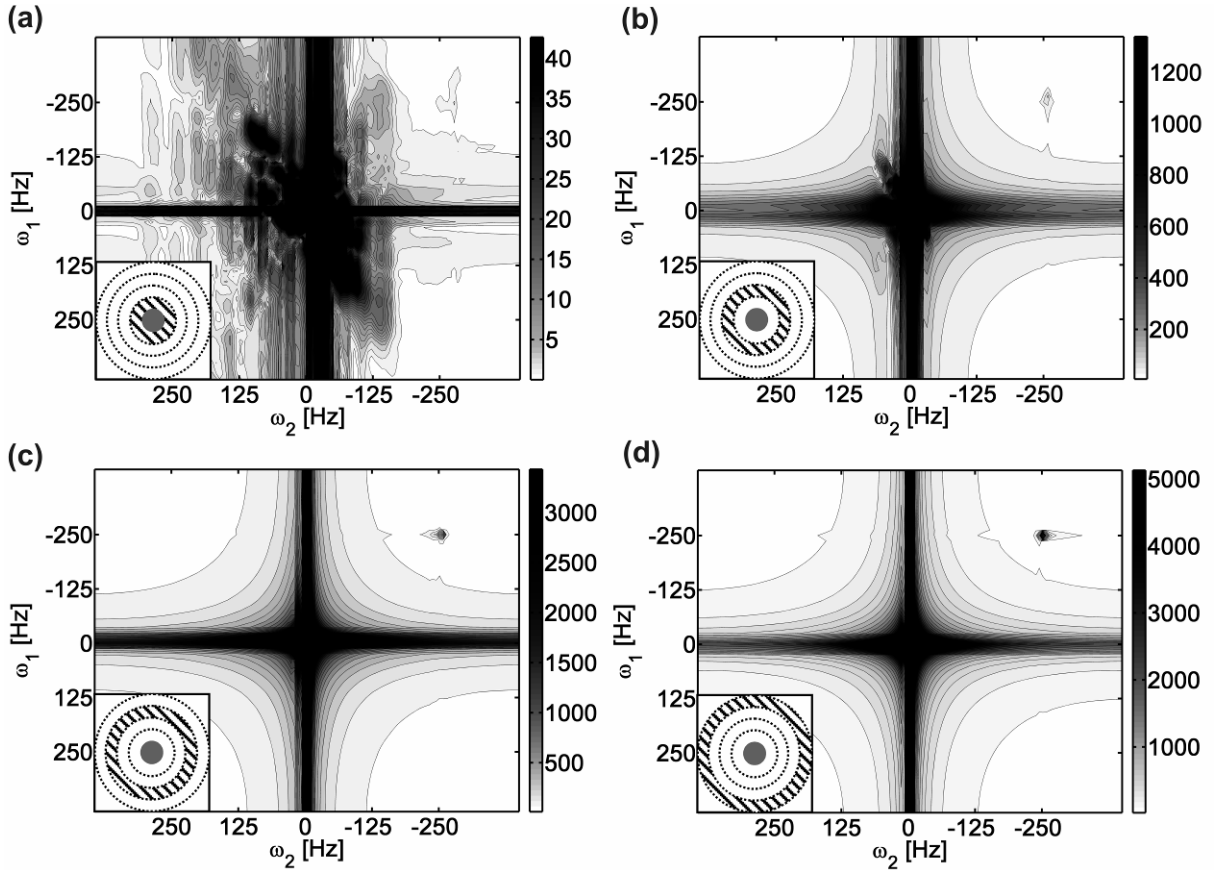


Figure 6.9: Spatial reach of the influence of B_{dip} . Simulated spectra were summed over different shells of a sample that modelled the local dipole field of an air bubble with $R = 50 \mu\text{m}$ and $\Delta\chi = 9.3 \text{ ppm}$. (a) – (d) Insets indicate, in a central slice through the $(982 \mu\text{m})^3$ sample, over which shell the spectra were summed (hatched area). Gray circles indicate the area where magnetization was set to zero in the simulations. Note the different ratio of I and S spin peak intensities. Scale bars in arbitrary intensity units. Different scale is mostly due to the vastly different number of grid points in the individual shells.

6.1.2 Experiments

NMR experiments were performed at 17.6 T with the Bruker Micro 2.5 gradient system and a 5-mm Bruker birdcage resonator as transmit-receive coil (see Sec 5.1). The optimized pulse sequence for spatially localized HOMOGENIZED spectroscopy (Fig. 4.14) was used, omitting the water suppression pulses to avoid saturation effects. Constant sequence parameters were: TR = 5 s, $t_2 = 156.4 \text{ ms}$, TD = 128 x 2048, SW = 10 x 10 ppm, NA = 8 with $\text{ph1} = (x, -x)$, and CG = 7.28 MHz/m ($\sim 17.08 \text{ G/cm}$) for 1 ms. Spectra were obtained after zero filling by a factor of two and Fourier transformation in XWinNMR 3.2 (Bruker). Analysis of the spectra was performed with MATLAB 7.3.0. Localized signal was acquired from sub-millimeter voxels (1 mm^3 , $900^3 \mu\text{m}^3$, $800^3 \mu\text{m}^3$, $750^3 \mu\text{m}^3$, $725^3 \mu\text{m}^3$, $700^3 \mu\text{m}^3$, $675^3 \mu\text{m}^3$, $660^3 \mu\text{m}^3$, $650^3 \mu\text{m}^3$, $640^3 \mu\text{m}^3$, $550^3 \mu\text{m}^3$ and $460^3 \mu\text{m}^3$) in a phantom consisting of 1.5 % water based agar-gel and 0.1 M NAA in a 5 mm sample tube. A 100 μm diameter glass sphere was positioned in the centre of the tube by fine balancing and rotating the phantom while heated in a water bath. By subsequent fast cooling to room temperature the position of the sphere was conserved.

Traces through the NAA methyl cross-peak at -2025 Hz along both axes from all measured spectra are presented in the stack plots of Fig. 6.10. The dominant effect is the reduction of cross-peak intensities with the voxel-size.

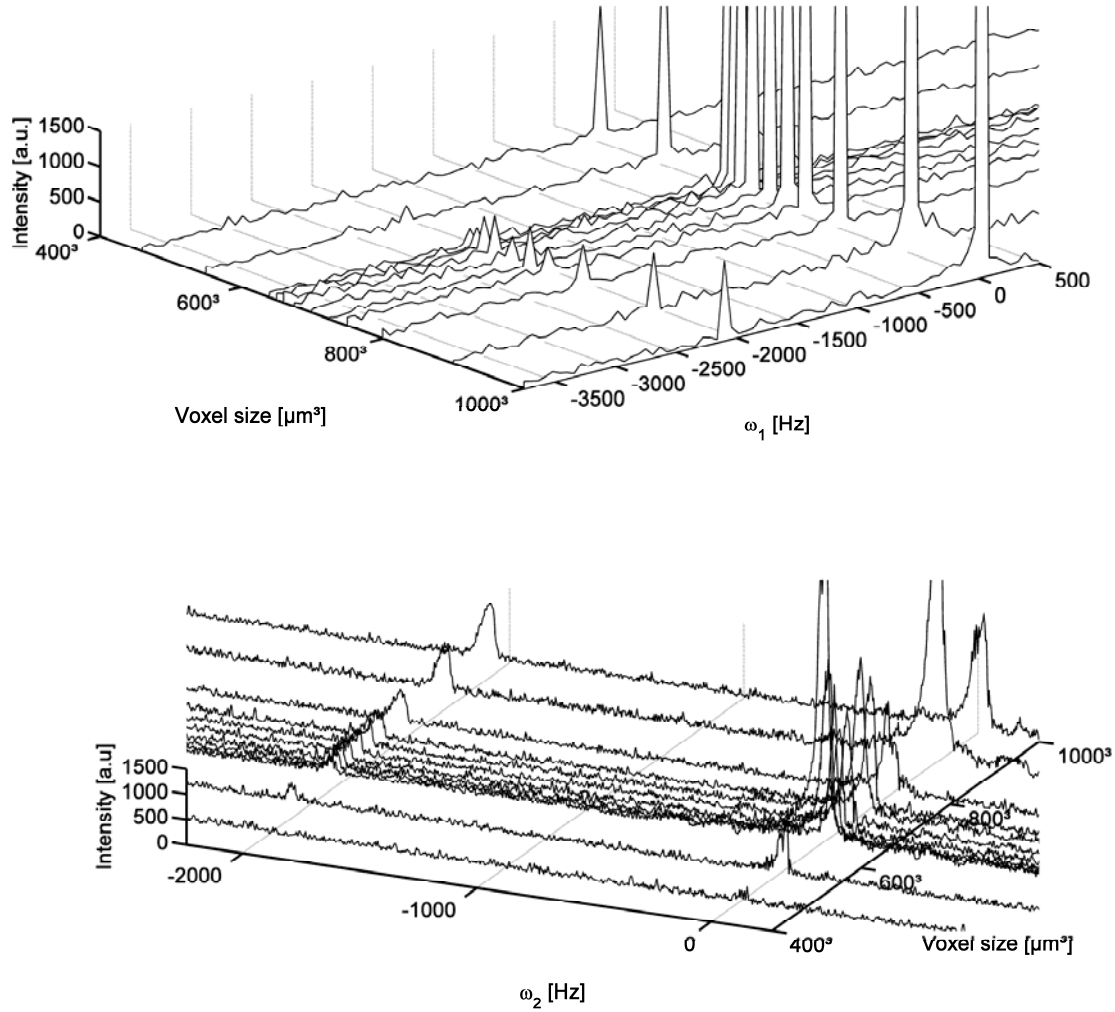


Figure 6.10: *Traces of the experimental 2D spectra as a function of the voxel-size. Single 1D spectra are traces of 2D spectra at -2025 Hz (NAA methyl group resonance). The peak at 0 Hz is pseudo noise from water. Stack plots were rotated for best visualization of the cross-peaks.*

6.1.3 Simulated vs. experimental spectra

Experimental spectra can be directly compared to simulation results for a glass inclusion (SIM4). As a reaction to the decrease in voxel-to dipole-field-source volume ratio, the same major effect of cross-peak intensity reduction was observed both in simulated and detected data (compare Fig 6.7 with Fig. 6.10, and consider also Fig. 6.11 for a direct comparison). The smallest voxel size, where an S peak was still observed was $(550 \mu\text{m})^3$ in case of measured spectra, corresponding to a voxel to dipole source volume ratio of $\eta = 317$, and $(500 \mu\text{m})^3$, corresponding to $\eta = 239$, in case of simulated spectra. For the measured voxel with $(460 \mu\text{m})^3$, corresponding to $\eta = 187$, and for the simulated voxels with $(482 \mu\text{m})^3$ and smaller, corresponding to volume ratios equal to or smaller than $\eta = 191$, no cross-peak was detected. In the simulated spectra, using the dipole field of an air inclusion (SIM6), no peak was observed for voxels smaller than $(607 \mu\text{m})^3$. The experimental data also showed decreasing SNR of 121, 53, and 34 for the metabolite peak in voxels of $(1 \text{ mm})^3$, $(750 \mu\text{m})^3$, and $(550 \mu\text{m})^3$, respectively (Fig. 6.11d-f). These results indicate that there is a limiting volume ratio, η_{limit} , specific to the magnetic susceptibility and size of the inhomogeneity source below which iZQC spectroscopy will not detect any cross-peaks at typical brain

metabolite concentrations. These limiting values for simulations and experiments are summarized in Fig. 6.12.

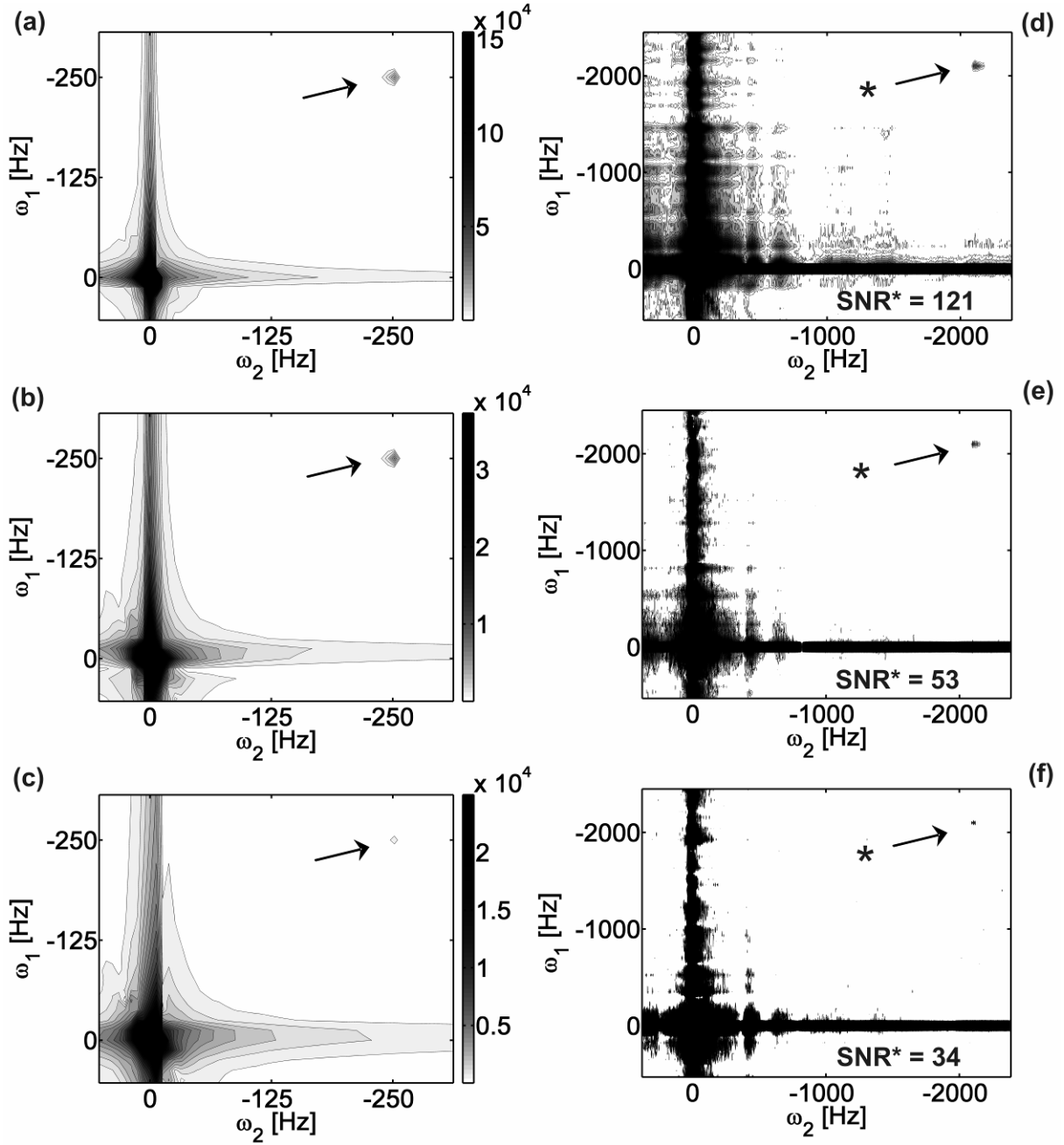


Figure 6.11: Simulated spectra compared to experimental observations for the case of a glass inclusion. Simulated and experimental spectra from a $(1 \text{ mm})^3$ voxel (a and d), from a $(750 \text{ } \mu\text{m})^3$ voxel (b and e), and from a $(550 \text{ } \mu\text{m})^3$ voxel (c and f), respectively. Arrows indicate the I-S cross peak in the simulations and the NAA(CH_3)-water cross peak in the experiments. Scale bars in arbitrary units for peak intensities in the simulated spectra and SNR of the cross-peak for the measured spectra are indicated.

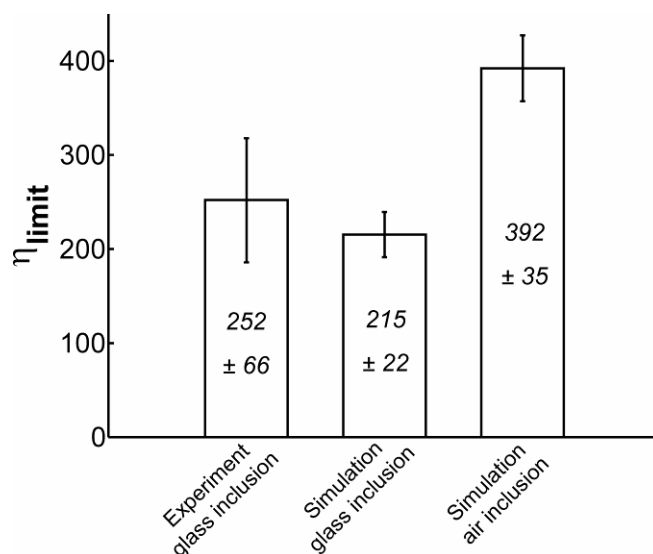


Figure 6.12: Minimum sample per inhomogeneity volume ratio (η_{limit}) defining the detection limit in iZQC-spectroscopy in the presence of local dipole fields. η_{limit} was determined from the smallest sample volume in which the cross peak was observable, according to the criteria defined in the text. Given errors for “Experiment glass inclusion”, “Simulation glass inclusion”, and “Simulation air inclusion” correspond to the step size in analysis of the experiment, and of the data sets SIM4, SIM6, respectively.

6.1.4 Discussion

The maximum tolerable volume ratio of a compact spherical dipole field source to a homogenous cube with watery solution for successful detection of HOMOGENIZED cross-peaks has been assessed. The presented simulations used almost the full capacity of a compute server for hundreds of hours in spite of the many conventions made for speed, which have slightly compromised the outcome. Digitization introduced potential errors in the calculations, because parts of the simulated cube were not sampled to fulfil Nyquists’ theorem for large t_1 values. However, the digitization error was arguably tolerable and the presented results were able to estimate the order of magnitude of dipole perturbation drawing a limit between voxels that yield enough signal for iZQC-cross-peak formation, and voxels from which no iZQC-cross-peak is originating. Simulated spectra were in good agreement with measured spectra. Signal refocusing in iZQC-spectroscopy broke down for centred spherical inhomogeneity sources with a volume of more than 0.1 % to 1 % of the voxel volume and with typical susceptibility differences of 1 to 10 ppm to the medium. There were three major differences between experiments and simulations. First, relaxation effects were not considered in the calculated spectra. However, relaxation time constants in vitro are more than one order of magnitude longer than the simulated FIDs. Thus, relaxation effects can be considered negligible. Second, in experiments, the methyl group of NAA possessed three protons in contrast to the simulations, where only one proton was considered. This means a factor of three in concentration difference. However, the sharp transition from detectable to not detectable peak, and the SNR of 34 for the smallest detectable peak suggest that concentration is not the dominant parameter. Thus, in spite of the concentration difference, measured and calculated results can be compared. Third, the bandwidth of the spectrum was different for experiments and simulations. The larger frequency offset for measurements had no influence on the refocusing efficiency of the DDF, but, essentially, reduced the impact on the cross-peak of the much higher pseudo noise arising from experimental imperfections (Fig. 6.11d-f). Pseudo noise that resulted from the local dipole was limited to a small frequency range around the water resonance. Nonetheless, pseudo noise extended over more than 1000 Hz in the

experimental spectra. It was more pronounced for larger voxels (Fig. 6.11d-f), because it resulted presumably from B_0 and B_1 inhomogeneities over the voxel and eddy currents for large gradient amplitudes. Experimental spectra from a binary system with only 250 Hz frequency difference, would have been additionally contaminated by pseudo noise from experimental imperfections, and therefore not been comparable with the simulations. Thus, the difference in spectral bandwidth even helps comparing experiments and simulations. It should be pointed out though that results were simulated for a basic iZQC pulse sequence and experiments were performed with a sequence optimized for *in vivo* applications. Experimental imperfections introduced by the localization module were not included in simulations, but they were kept at minimum by careful setup. Similarity between simulated and measured spectra and similarity of the derived detection limits strengthen the assumption that experimental errors were negligible.

Determination of the detection limit in case of a single inclusion allows for speculations on the influence of local dipole fields in samples with multiple inhomogeneity sources. Periodic samples can be modelled as an ensemble of unit cubes, where the influence of the neighbouring dipoles is smaller than the effect of the central dipole on a peripheral shell within the unit cube. Along the z-axis, where the dipole field is largest, the sum of the fields of two neighbouring dipoles equals the field of a single dipole if the distance is increased by only 26% (exactly $\sqrt[3]{2}$). Thus, in order to detect iZQC cross-peaks, the minimum size of a voxel including periodic inhomogeneity sources has to be doubled relative to a sample cube with a single centred dipole source, as treated in the present study. In case of clustered inhomogeneities, the minimum volume ratio depends on the exact geometry, which is usually not known in experimental investigations.

Section 6.2 addresses the question if the optimized HOMOGENIZED sequence can produce better spectra than conventional MRS in presence of clustered but very small paramagnetic particles.

6.2 Resolution enhancement in presence of iron-oxide

microparticles

6.2.1 Acquisition parameters

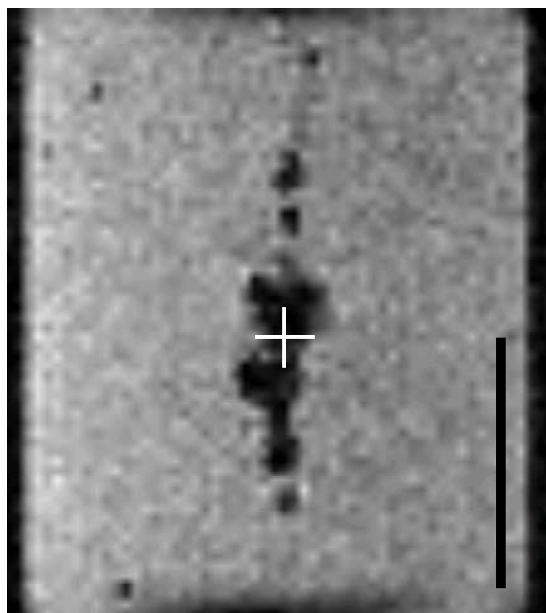


Figure 6.13: Gradient echo image of the phantom with injected iron-oxide particles. Scale bar: 2 mm. The white cross-hair defines the reference for voxel positions (see text).

Phantom experiments were performed in order to investigate the potential of HOMOGENIZED in comparison to the conventional PRESS sequence to enhance spectral resolution in presence of local field inhomogeneities generated by clustered iron-oxide microparticles. Experiments were conducted at 17.6 T using the Bruker Micro 2.5 gradient system, and a 5 mm Bruker birdcage resonator as transmit-receive coil (see Sec. 5.1). The phantom consisted of a 5 mm NMR tube filled with a 1.5 % water based agar-gel containing 50 mM NAA. 2 μ l of a sol containing superparamagnetic iron-oxide particles with a diameter of 6 μ m (25 mg/ml, sicastar®-M-CT-greenF plain, Micromod Partikeltechnologie, Rostock, Germany) were injected with a Hamilton syringe into the centre of the gel. In T_2^* -weighted images, regions of signal loss caused by these small dipoles greatly exceeded the particle size, and, therefore, their distribution could be monitored using images with low resolution as compared to the particle size (Fig. 6.13). Spectra were recorded from a total of three

different voxel sizes: $(2 \text{ mm})^3$, $(3 \text{ mm})^3$, and $3 \times 3 \times 6 \text{ mm}^3$. The voxels were positioned in the centre of the main particle cluster (marked by a white cross-hair in Fig. 6.13). Acquisition parameters for PRESS experiments were: $TR = 3 \text{ s}$, $TE = 60 \text{ ms}$, $SW = 8 \text{ ppm}$, $TD = 4096$, $NA = 16$, $t_{\text{experiment}} = 2 \text{ min}$. In HOMOGENIZED experiments, the timing between the second RF-pulse and the acquisition was varied to match the echo times for PRESS, thus $TE_{\text{Homogenized}} = 50 \text{ ms}$. Other acquisition parameters were: $TR = 3 \text{ s}$, $SW = 8 \times 8 \text{ ppm}$, $TD = 512 \times 2048$, $NA = 4$, $t_{\text{experiment}} = 2 \text{ h}$.

6.2.2 Processing

The raw data of the PRESS experiments were apodized using an exponential function (LB of 5 Hz), zero filled, and Fourier transformed. Phase and baseline correction were performed in the frequency domain. The chemical shifts were referenced to the NAA methyl signal, which was set to 2.0 ppm. Linewidths were measured at peak half maximum. SNR was calculated by dividing the intensity of the NAA methyl peak by the SD of the signal at baseline level. Processing of the HOMOGENIZED time domain data was performed as described above for PRESS with additional application of FT, phase and baseline correction in the indirect dimension (ω_1).

6.2.3 Results

Given the observation that second-order shimming *in vivo* with the present hardware required avoiding air-tissue and muscle-bone boundaries and that it was unsuccessful in the spinal cord of the rat (Sec. 5.2), only first-order shimming was applied to compare conventional localized spectra with those obtained with an iZQC method. Figure 6.14 shows the NAA line in PRESS (a/b/c) and HOMOGENIZED (d/e/f) spectra obtained from voxels that had different sizes and were positioned in the centre of the particle cluster. Prior to the PRESS experiments, a central $(3 \text{ mm})^3$ voxel was shimmed to first order. HOMOGENIZED spectra were acquired without shimming. In the PRESS spectra, a value of 46 Hz was observed for the linewidth in the smallest voxel (Fig. 6.14a), and more than 80 Hz for the $(3 \text{ mm})^3$ and the $3 \times 3 \times 6 \text{ mm}^3$ voxels (Fig. 6.14b/c). Most of the particles were already contained in the $(3 \text{ mm})^3$ voxel and further elongation did not lead to a significant increase in local inhomogeneity. In the HOMOGENIZED spectra, linewidths of 9 Hz were observed, independent of the voxel size. The effects of local inhomogeneities did not cause line broadening along the ω_1 dimension of the 2D spectra. This finding shows that iZQC techniques have the potential to compensate for local field distortions and provide resolved spectra even in the presence of iron-oxide particles.

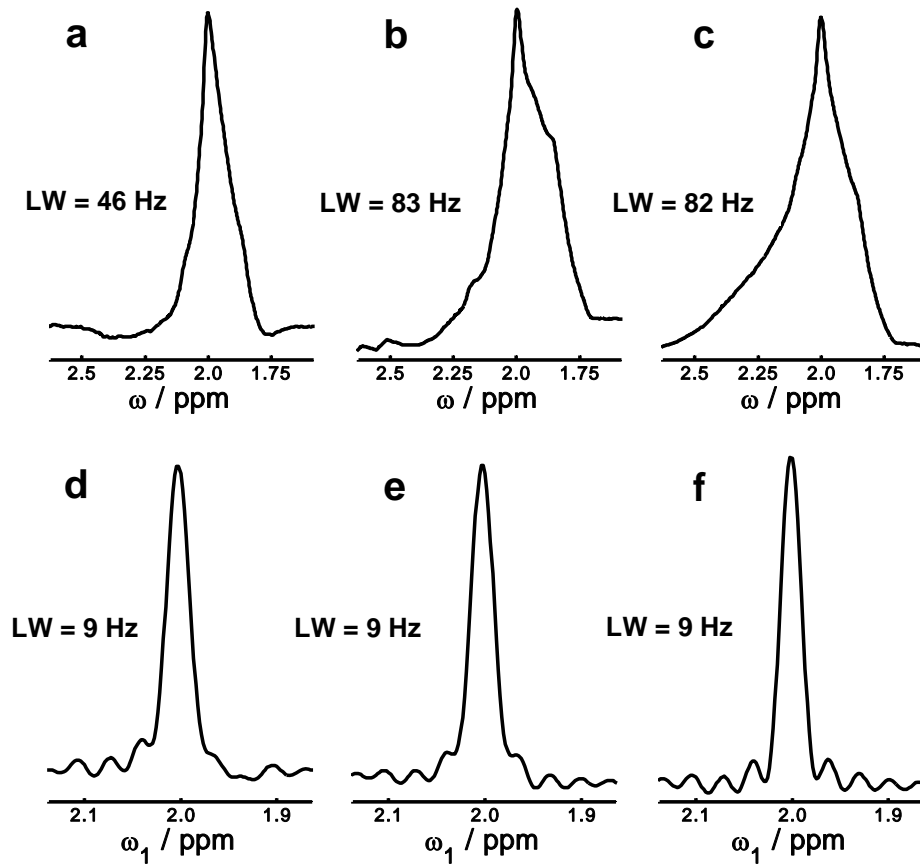


Figure 6.14: Line shapes of the NAA methyl resonance in PRESS and HOMOGENIZED spectra of a phantom with injected iron-oxide particles for different voxel sizes. All voxels were centred at the cross-hair in Fig. 6.13. The results for PRESS are shown in a-c: a) $(2 \text{ mm})^3$ voxel, b) $(3 \text{ mm})^3$ voxel, c) $3 \times 3 \times 6 \text{ mm}^3$ voxel; the results for HOMOGENIZED in d-f: d) $(2 \text{ mm})^3$ voxel, e) $(3 \text{ mm})^3$ voxel, f) $3 \times 3 \times 6 \text{ mm}^3$ voxel. The linewidths (LW) are indicated.

6.2.4 Discussion

As shown by these results, the spectral resolution and quality of conventional localized MRS methods depend on the actual distribution of the magnetic particles. In contrast, as expected from the results presented in Sec. 6.1, linewidths in HOMOGENIZED spectra from sufficiently large voxels were not influenced by iron particles. It turned out that even a $(2\text{ mm})^3$ voxel is sufficiently large to keep the average effect of dipole perturbation caused by $2\text{ }\mu\text{l}$ inhomogeneous medium negligible. iZQC techniques may thus offer the unique potential to perform *in vivo* MRS in tissue containing microscopic iron labels or other, very small sources of field distortions.

6.3 Conclusion

The results presented in the first part of this chapter provide insights in iZQC cross-peak generation in inhomogeneous magnetic fields. Essentially, the presence of a dipole perturbation has the dominating effect of decreasing the amplitude of the solute peak before line broadening can be observed in the spectra. Therefore, iZQC spectroscopy is possible as long as the relative volume occupied by air inclusions does not exceed the order of 0.1% of the sample volume. It becomes evident that iZQC spectroscopy is not feasible in samples with a high density of inhomogeneities with large susceptibility differences. Considering the case of air-filled inclusions in a watery environment, applications are deemed impossible, for example, in porous materials with foam-like composition, in green leaves in plant science, or in investigations of lung epithelium *in vivo*. However, the outcome of the study presented in the second part of the chapter demonstrates, that iZQC spectroscopy may be applied in the presence of clustered sources if these are microscopic. *In vivo* investigations in the presence of very small paramagnetic particles (USPIOs) are potential areas of application for iZQC spectroscopy where conventional NMR fails.

7. Summary

Nuclear magnetic resonance has numerous applications for *in vivo* diagnostics. However, methods requiring homogeneous magnetic fields, particularly magnetic resonance spectroscopy (MRS) techniques, have limited applicability in regions near or on anatomical boundaries that cause strong inhomogeneities. In cases where the shim system can not or just partly correct for these inhomogeneities, methods based on intermolecular multiple quantum coherence (iMQC) detection can provide an alternative solution for *in vivo* MRS.

This dissertation presented the development, validation and application potential of a novel MRS pulse sequence detecting intermolecular zero-quantum coherences (iZQC) with special emphasis on *in vivo* experiments. In addition, the detection limit and spectral behaviour of iZQC-MRS under modelled realistic conditions were systematically approached for the first time.

Based on the original sequence used to detect two dimensional (2D) iZQC-spectra, dubbed HOMOGENIZED, methodological development led to increased sensitivity and water suppression, and decreased T_2 -relaxation effects through the application of a frequency selective 90° RF-pulse in place of a non selective β -pulse. Best water suppression was achieved by placing a pair of selective refocusing units immediately prior to the acquisition window. The same placement was found to be optimal also for single voxel localization units based on slice selective spin echo refocusing. By voxel selection before the iZQC-MRS sequence, the chemical shift artefact could be avoided. However, this led to significant residual signal from outside the voxel. Analytical derivations of signal evolution for several sequences presented in this dissertation provide useful additions to the iZQC MRS theory.

In vivo applications of the developed sequence provided high quality spectra in the central nervous system of the rat, the mouse brain and in subcutaneous xenograft tumor grown on the thigh of the mouse. In all these 2D spectra, the limiting factor of the resolution in the indirect dimension was the digital sampling rate, rather than inhomogeneous line broadening. Nevertheless, linewidths of the cross-peaks were similar or narrower than along the direct axis, where the sampling rate was about ten times higher. The first MR spectroscopic investigation of the rat spinal cord at 17.6 T was performed. Through its insensitivity to macroscopic field inhomogeneities, the localized iZQC method allowed for the selection of larger voxels than conventional methods and still provided the same spectral resolution. This property was used also in tumor tissue to propel the relative signal to noise (SNR) efficiency of the iZQC spectroscopy for the first time above the SNR efficiency of a conventional sequence. Future applications for fast metabolite count in large inhomogeneous organs, like a tumor, are thinkable.

Extensive simulations and phantom experiments assessed the limit of iZQC cross-peak detection in presence of local field distortions. The order of maximum volume ratio between dipole source and voxel was found to be between 0.1 % and 1 %. It is an essential conclusion of this study that the dominant effect of microscopic to mesoscopic inhomogeneities on iZQC spectra under general *in vivo* conditions, like for voxels greater than $(1\text{ mm})^3$ and metabolite concentrations in the millimolar range, is a cross-peak intensity reduction and not line broadening. The iZQC method provided resolution enhancement in comparison to conventional MRS even in the presence of clustered paramagnetic microparticles. However, the vision of iZQC spectroscopy in green leafs or the lung epithelium has to be, unfortunately, abandoned, because cross-peaks can be observed until the volume of the separating medium is much larger than the volume of local dipole sources.

Intermolecular zero-quantum coherence spectroscopy remains an exciting field in NMR research on living organisms. It provides access to the monitoring of relative metabolite concentration changes in the presence of microscopic iron particles, which raises realistic hopes for new applications in studies using stained stem cells.

8. Zusammenfassung

Magnetische Kernresonanz (NMR) hat viele diagnostische *in vivo* Anwendungen. Trotzdem können einige Methoden, wie die NMR-Spektroskopie (MRS), nur in Magnetfeldern mit hervorragender Homogenität angewendet werden. Das ist eine Voraussetzung, die in der Nähe von anatomischen Grenzregionen aufgrund der starken Suszeptibilitätsgradienten nicht erfüllt ist. NMR Forschungstomographen sind in der Regel mit zusätzlichen Shim-Spulen ausgerüstet, die Feldschwankungen kompensieren sollen. Wenn die durch ein Shim-System erreichte Homogenität immer noch nicht genügt, können alternative NMR-Methoden, wie etwa die Messung intermolekularer Mehrquantenkohärenzen (iMQC) die Lösung bereitstellen.

Die hier vorgelegte Dissertation zeigt die Entwicklung und Validierung, sowie das Anwendungspotenzial einer neuen MRS-Pulssequenz, die intermolekulare Nullquantenkohärenzen (iZQC) detektiert und für *in vivo* Experimente besonders geeignet ist. Des Weiteren wurden Detektionsgrenze und spektrale Änderungen in iZQC-MRS unter simulierten realistischen Bedingungen zum ersten Mal analysiert.

Ausgangspunkt der methodischen Entwicklung war die Originalsequenz für die Aufnahme zweidimensionaler iZQC-Spektren, genannt HOMOGENIZED. Die Verwendung eines frequenzselektiven 90° Pulses anstelle des β -Pulses in HOMOGENIZED bewirkt eine Verbesserung in Sensitivität und in der Effizienz der Wasserunterdrückung, sowie eine Verminderung der T_2 -Relaxationseffekte. Die Wasserunterdrückung wurde durch Einfügung zweier wasserfrequenzselektiver Refokussierungspulse unmittelbar vor der Akquisition weiter optimiert. Dieselbe Position erwies sich als optimal für die „single voxel“ Lokalisierungseinheiten. Andererseits vermeidet die Durchführung der Lokalisation vor der iZQC-MRS Sequenz „chemical shift“ Artefakte auf Kosten der Lokalisierungseffizienz. Die zahlreichen analytischen Berechnungen im methodischen Teil dieser Doktorarbeit stellen wichtige Erweiterungen der iZQC MRS Theorie dar.

In vivo Anwendungen der entwickelten Sequenz im zentralen Nervensystem der Ratte, im Gehirn der Maus, sowie im subkutanen Tumor am Oberschenkel der Maus, resultierten in hochwertigen Spektren. Limitierender Faktor für die spektrale Auflösung in der indirekten Dimension in diesen 2D Spektren war die digitale Akquisitionsrate und nicht der, für konventionelle MRS typische, inhomogene Linienverbreiterungseffekt. Trotz der zehnfachen Akquisitionsrate in der direkten Dimension waren die Cross-peaks in der indirekten Dimension immer schmaler. Im Rahmen dieser Doktorarbeit wurde die erste MR spektroskopische Studie im Rückenmark der Ratte bei 17.6 Tesla durchgeführt. Durch die Unempfindlichkeit gegenüber makroskopischen Feldinhomogenitäten war die Selektion größerer Voxel als mit konventionellen Techniken, ohne Verlust an spektraler Auflösung, möglich. Dies wurde auch im Tumorgewebe verwendet, um die relative Signal-zu-Rausch (SNR) Effizienz der neuen iZQC-Methode zum ersten Mal über die SNR-Effizienz einer konventionellen Technik zu treiben. Es besteht die Aussicht auf zukünftige Anwendungen für schnelle Metabolitendetektion in großen Organen und Tumoren.

Die Detektionsgrenze der iZQC-Methoden in der Nähe von lokalen Dipolfeldern wurde mit aufwendigen Simulationen und Experimenten am Phantom abgeschätzt. Um einen Cross-peak zu detektieren darf der eigentliche Dipol nicht mehr als 0.1 % bis 1 % des Voxelvolums belegen. Eine wichtige Folgerung dieser Studie ist, dass unter üblichen *in vivo* Bedingungen, wie Voxel mit einer Größe von $(1\text{ mm})^3$ oder mehr und Metabolitenkonzentrationen im Millimolarbereich, mikroskopische und mesoskopische Inhomogenitäten vielmehr eine

Abnahme der Cross-peak Intensität als eine Linienverbreiterung verursachen. Diese Folgerung wurde auch dadurch bestätigt, dass die iZQC-Sequenz sogar in der Gegenwart von gebündelten paramagnetischen Mikropartikeln hochwertige Spektren lieferte. Leider folgt daraus aber auch, dass die Vorstellung von iZQC-MRS in grünen Blättern oder im Epithel der Lunge verworfen werden muss.

Intermolekulare Nullquantenkohärenzspektroskopie bleibt für zukünftige Entwicklungen und Anwendungen ein sehr interessanter Bereich der NMR-Forschung an lebenden Organismen. Sie ermöglicht die Beobachtung von relativen Metabolitkonzentrationen auch etwa in Proben die Eisenpartikeln enthalten. Dies weckt realistische Hoffnungen für neue MRS Studien auch bei Untersuchungen mit markierten Stammzellen.

9. References

1. Purcell EM, Torrey HC, Pound RV. 1946 Resonance Absorption by Nuclear Magnetic Moments in a Solid. *Physical Review*;69:37-38.
2. Bloch F, Hansen WW, Packard M. 1946 Nuclear Induction. *Physical Review*;69:127.
3. Ernst RR, Anderson WA. 1966 Application of Fourier transform spectroscopy to magnetic resonance. *Review of Scientific Instruments*;37:93-102.
4. Lauterbur PC. 1973 Image Formation by Induced Local Interactions - Examples Employing Nuclear Magnetic-Resonance. *Nature*;242:190-191.
5. Mansfield P, Grannell PK. 1973 NMR Diffraction in Solids. *Journal of Physics C*;6:422-426.
6. Gruetter R, Weisdorf SA, Rajanayagan V, Terpstra M, Merkle H, Truwit CL, Garwood M, Nyberg SL, Ugurbil K. 1998 Resolution improvements in in vivo H-1 NMR spectra with increased magnetic field strength. *Journal of Magnetic Resonance*;135(1):260-264.
7. Otazo R, Mueller B, Ugurbil K, Wald L, Posse S. 2006 Signal-to-noise ratio and spectral linewidth improvements between 1.5 and 7 Tesla in proton echo-planar spectroscopic imaging. *Magnetic Resonance in Medicine*;56:1200-1210.
8. Chen W, Zhu XH. 2005 Dynamic study of cerebral bioenergetics and brain function using in vivo multinuclear MRS approaches. *Concepts in Magnetic Resonance Part A*;27A(2):84-121.
9. Terpstra M, Marjanska M, Henry PG, Tkac I, Gruetter R. 2006 Detection of an antioxidant profile in the human brain in vivo via double editing with MEGA-PRESS. *Magnetic Resonance in Medicine*;56(6):1192-1199.
10. Juchem C, Merkle H, Schick F, Logothetis NK, Pfeuffer J. 2004 Region and volume dependencies in spectral line width assessed by H-1 2D MR chemical shift imaging in the monkey brain at 7 T. *Magnetic Resonance Imaging*;22(10):1373-1383.
11. de Graaf RA. *In vivo NMR spectroscopy: Principles and Techniques*: John Wiley & Sons, Ltd.; 1998.
12. Hoult DI. 1987 Shimming on Spatially Localized Signals. *Journal of Magnetic Resonance*;73(1):174-177.
13. Holz D, Jensen D, Proksa R, Tochtrop M, Vollmann W. 1988 Automatic Shimming for Localized Spectroscopy. *Medical Physics*;15(6):898-903.
14. Gruetter R, Boesch C. 1992 Fast, Noniterative Shimming of Spatially Localized Signals - In vivo Analysis of the Magnetic-Field Along Axes. *Journal of Magnetic Resonance*;96(2):323-334.
15. Gruetter R. 1993 Automatic, Localized In vivo Adjustment of All 1st-Order and 2nd-Order Shim Coils. *Magnetic Resonance in Medicine*;29(6):804-811.
16. Bottomley PA; Selective volume method for performing localized MR spectroscopy. US patent 4480228. 1984.
17. Frahm J, Merboldt KD, Hanicke W. 1987 Localized proton spectroscopy using stimulated echoes. *Journal of Magnetic Resonance*;72:502-508.
18. Garwood M, DelaBarre L. 2001 The return of the frequency sweep: Designing adiabatic pulses for contemporary NMR. *Journal of Magnetic Resonance*;153:155-177.
19. Jeener J. 1971; Basko Polje, Yugoslavia.
20. Aue WP, Bartholdi E, Ernst RR. 1976 2-dimensional spectroscopy - Application to nuclear magnetic-resonance. *Journal of Chemical Physics*;64:2229-2246.
21. Berkowitz BA, Wolff SD, Balaban RS. 1988 Detection of metabolites in vivo using 2d proton homonuclear correlated spectroscopy. *Journal of Magnetic Resonance*;79:547-553.

22. Ballon D, Mahmood U, Jakubowski A, Koutcher JA. 1993 Resolution enhanced NMR-spectroscopy in biological-systems via magnetic-susceptibility matched sample immersion chambers. *Magnetic Resonance in Medicine*;30:754-758.
23. Andrew ER, Bradbury A, Eades RG. 1959 Removal of dipolar broadening of nuclear magnetic resonance spectra of solids by specimen rotation. *Nature*;183:1802-1803.
24. Wind RA, Hu JZ, Rommereim DN. 2003 High-resolution H-1 NMR spectroscopy in live mouse subjected to 1.5 Hz magic angle spinning. *Magnetic Resonance in Medicine*;50:1113-1119.
25. Garbow JR, Weitekamp DP, Pines A. 1983 Total Spin Coherence Transfer Echo Spectroscopy. *Journal of Chemical Physics*;79(11):5301-5310.
26. de Graaf RA, Rothman DL, Behar KL. 2007 High resolution NMR spectroscopy of rat brain in vivo through indirect zero-quantum-coherence detection. *Journal of Magnetic Resonance*;187:320-326.
27. Vathyam S, Lee S, Warren WS. 1996 Homogeneous NMR spectra in inhomogeneous fields. *Science*;272(5258):92-96.
28. Faber C. 2007 Resolution Enhancement in In Vivo NMR Spectroscopy. *Annual Reports on NMR Spectroscopy*;61:1-50.
29. Chen Z, Hou T, Chen ZW, Hwang DW, Hwang LP. 2004 Selective intermolecular zero-quantum coherence in high-resolution NMR under inhomogeneous fields. *Chemical Physics Letters*;386(1-3):200-205.
30. Lin YY, Ahn S, Murali N, Brey W, Bowers CR, Warren WS. 2000 High-resolution, > 1 GHz NMR in unstable magnetic fields. *Physical Review Letters*;85(17):3732-3735.
31. Galiana G, Branca RT, Warren WS. 2005 Ultrafast intermolecular zero quantum spectroscopy. *Journal of the American Chemical Society*;127(50):17574-17575.
32. Balla DZ, Faber C. 2008 Localized Intermolecular Zero-Quantum Coherence Spectroscopy In Vivo. *Concepts in Magnetic Resonance Part A*;32A(2):117-133.
33. Richter W, Lee SH, Warren WS, He QH. 1995 Imaging with Intermolecular Multiple-Quantum Coherences in Solution Nuclear-Magnetic-Resonance. *Science*;267(5198):654-657.
34. Bowtell R, Robyr P. 1996 Structural investigations with the dipolar demagnetizing field in solution NMR. *Physical Review Letters*;76(26):4971-4974.
35. Warren WS, Ahn S, Mescher M, Garwood M, Ugurbil K, Richter W, Rizi RR, Hopkins J, Leigh JS. 1998 MR imaging contrast enhancement based on intermolecular zero quantum coherences. *Science*;281(5374):247-251.
36. Richter W, Richter M, Warren WS, Merkle H, Andersen P, Adriany G, Ugurbil K. 2000 Functional magnetic resonance imaging with intermolecular multiple-quantum coherences. *Magnetic Resonance Imaging*;18(5):489-494.
37. Balla D, Faber C. 2004 Solvent suppression in liquid state NMR with selective intermolecular zero-quantum coherences. *Chemical Physics Letters*;393(4-6):464-469.
38. Balla DZ, Faber C. 2007 In vivo intermolecular zero-quantum coherence MR spectroscopy in the rat spinal cord at 17.6 T. *Magnetic Resonance Materials in Physics Biology and Medicine*;20:183-191.
39. Balla DZ, Faber C. 2008 Intermolecular zero-quantum coherence NMR spectroscopy in the presence of local dipole fields. *Journal of Chemical Physics*;128:154522.
40. Balla DZ, Melkus G, Faber C. 2006 Spatially localized intermolecular zero-quantum coherence spectroscopy for in vivo applications. *Magnetic Resonance in Medicine*;56(4):745-753.
41. van de Ven FJM. *Multidimensional NMR in Liquids: Basic Principles and Experimental Methods*: VCH Publishers, Inc.; 1995.
42. Warren WS, Richter W, Andreotti AH, Farmer BT. 1993 Generation of Impossible Cross-Peaks between Bulk Water and Biomolecules in Solution NMR. *Science*;262(5142):2005-2009.

-
43. He QH, Richter W, Vathyam S, Warren WS. 1993 Intermolecular Multiple-Quantum Coherences and Cross Correlations in Solution Nuclear-Magnetic-Resonance. *Journal of Chemical Physics*;98(9):6779-6800.
 44. Jeener J, Vlassenbroek A, Broekaert P. 1995 Unified Derivation of the Dipolar Field and Relaxation Terms in the Bloch-Redfield Equations of Liquid NMR. *Journal of Chemical Physics*;103(4):1309-1332.
 45. Minot ED, Callaghan PT, Kaplan N. 1999 Multiple echoes, multiple quantum coherence, and the dipolar field: Demonstrating the significance of higher order terms in the equilibrium density matrix. *Journal of Magnetic Resonance*;140(1):200-205.
 46. Jeener J. 2000 Equivalence between the "classical" and the "Warren" approaches for the effects of long range dipolar couplings in liquid nuclear magnetic resonance. *Journal of Chemical Physics*;112(11):5091-5094.
 47. Bowtell R, Bowley RM, Glover P. 1990 Multiple Spin Echoes in Liquids in a High Magnetic-Field. *Journal of Magnetic Resonance*;88(3):643-651.
 48. Bowden GJ, Heseltine T, Prandolini MJ. 1995 Double quantum and cross correlation peaks in COSY NMR spectra. *Chemical Physics Letters*;233:639-643.
 49. Lee S, Richter W, Vathyam S, Warren WS. 1996 Quantum treatment of the effects of dipole-dipole interactions in liquid nuclear magnetic resonance. *Journal of Chemical Physics*;105(3):874-900.
 50. Levitt MH. 1996 Demagnetization field effects in two-dimensional solution NMR. *Concepts in Magnetic Resonance*;8(2):77-103.
 51. Ahn S, Lee S, Warren WS. 1998 The competition between intramolecular J couplings, radiation damping, and intermolecular dipolar couplings in two-dimensional solution nuclear magnetic resonance. *Molecular Physics*;95(5):769-785.
 52. Warren WS, Ahn S. 1998 The boundary between liquidlike and solidlike behavior in magnetic resonance. *Journal of Chemical Physics*;108(4):1313-1325.
 53. Chen Z, Kennedy SD, Zhong JH. 1999 Theoretical formalism and experimental confirmation of intermolecular dipolar effects under time-averaged magnetic field gradients. *Chemical Physics Letters*;313(1-2):217-224.
 54. Kimmich R, Ardelean I. 1999 Intermolecular multiple-quantum coherence transfer echoes and multiple echoes in nuclear magnetic resonance. *Journal of Chemical Physics*;110(8):3708-3713.
 55. Ardelean I, Kimmich R. 2000 Diffusion measurements with the pulsed gradient nonlinear spin echo method. *Journal of Chemical Physics*;112(12):5275-5280.
 56. Ardelean I, Kimmich R. 2000 Demagnetizing field effects on the Hahn echo. *Chemical Physics Letters*;320(1-2):81-86.
 57. Ardelean I, Kimmich R. 2000 Erratum to "Demagnetizing field effects on the Hahn echo" [Chem. Phys. Lett. 320 (2000) 81]. *Chemical Physics Letters*;332:624-625.
 58. Ardelean I, Kossel E, Kimmich R. 2001 Attenuation of homo- and heteronuclear multiple spin echoes by diffusion. *Journal of Chemical Physics*;114(19):8520-8529.
 59. Chen Z, Chen ZW, Zhong JH. 2001 Quantitative study of longitudinal relaxation related to intermolecular dipolar interactions in solution NMR. *Chemical Physics Letters*;333(1-2):126-132.
 60. Chen Z, Zheng SK, Zhong JH. 2001 Optimal RF flip angles for multiple spin-echoes and iMQCs of different orders with the CRAZED pulse sequence. *Chemical Physics Letters*;347(1-3):143-148.
 61. Chen Z, Zhong JH. 2001 Unconventional diffusion behaviors of intermolecular multiple-quantum coherences in nuclear magnetic resonance. *Journal of Chemical Physics*;114(13):5642-5653.
 62. Ramanathan C, Bowtell R. 2001 Dynamics of the nuclear magnetic resonance COSY-revamped by asymmetric z-gradients (CRAZED) experiment. *Journal of Chemical Physics*;114(24):10854-10859.

63. Ardelean I, Kimmich R. 2002 Response to "Comment on 'Diffusion measurements with the pulsed gradient nonlinear spin echo method' " [J. Chem. Phys. 116, 1204 (2002)]. *Journal of Chemical Physics*;116(3):1206-1206.
64. Chen Z, Chen ZW, Zhong JH. 2002 Observation and characterization of intermolecular homonuclear single-quantum coherences in liquid nuclear magnetic resonance. *Journal of Chemical Physics*;117(18):8426-8435.
65. Jeener J. 2002 Comment on "Diffusion measurements with the pulsed gradient nonlinear spin echo method" [J. Chem. Phys. 112, 5275 (2000)]. *Journal of Chemical Physics*;116(3):1204-1205.
66. Marques JP, Grant S, Blackband S, Bowtell RW. 2005 Intermolecular multiple quantum coherences at high magnetic field: The nonlinear regime. *Journal of Chemical Physics*;123(16):164311.
67. Zheng BW, Chen Z, Cai SH, Zhong JH, Ye CH. 2005 Theoretical formalism and experimental verification of line shapes of NMR intermolecular multiple-quantum coherence spectra. *Journal of Chemical Physics*;123(7):074317-1-7.
68. Ahn S, Warren WS. 1998 Effects of intermolecular dipolar couplings in solution NMR in separated time intervals: the competition for coherence transfer pathways. *Chemical Physics Letters*;291(1-2):121-129.
69. Cai CB, Chen Z, Cai SH, Hwang LP, Zhong JH. 2005 Finite difference simulation of diffusion behaviors under inter- and intra-molecular multiple-quantum coherences in liquid NMR. *Chemical Physics Letters*;407(4-6):438-443.
70. Cai CB, Chen Z, Cai SH, Zhong JH. 2005 A simulation algorithm based on Bloch equations and product operator matrix: application to dipolar and scalar couplings. *Journal of Magnetic Resonance*;172(2):242-253.
71. Chen Z, Chen ZW, Zhong JH. 2001 Quantitative characterization of intermolecular dipolar interactions of two-component systems in solution nuclear magnetic resonance. *Journal of Chemical Physics*;115(23):10769-10779.
72. Chen Z, Lin GX, Zhong JH. 2001 Diffusion of intermolecular zero- and double-quantum coherences in two-component spin systems. *Chemical Physics Letters*;333(1-2):96-102.
73. Engelsberg M, Barros W. 2005 Distant-dipole field in liquids and diffusion: A perturbative approach. *Journal of Chemical Physics*;122(3):034501.
74. Engelsberg M, Barros W, Hallwass F. 2004 Intermolecular double-quantum coherences in two-dimensional spectra of binary mixtures in solution. The role of diffusion. *Journal of Chemical Physics*;120(22):10659-10665.
75. Richter W, Warren WS. 2000 Intermolecular multiple quantum coherences in liquids. *Concepts in Magnetic Resonance*;12(6):396-409.
76. Zhu XQ, Cai CB, Chen Z, Zhong JH. 2005 Multiplet patterns due to co-existing intermolecular dipolar and intramolecular scalar couplings in liquid nuclear magnetic resonance. *Chinese Physics*;14(3):516-523.
77. Zhu XQ, Chen Z, Cai SH, Zhong JH. 2005 Selection of intra- or inter-molecular multiple-quantum coherences in NMR of highly polarized solution. *Physica B*;362(1-4):286-294.
78. Ahn S, Lisitza N, Warren WS. 1998 Intermolecular zero-quantum coherences of multi-component spin systems in solution NMR. *Journal of Magnetic Resonance*;133(2):266-272.
79. Ardelean I, Kimmich R, Stapf S, Demco DE. 1998 The nonlinear stimulated echo in the presence of inequivalent spins. *Journal of Magnetic Resonance*;132(1):138-143.
80. Warren WS, Huang SY, Ahn S, Lin YY. 2002 Understanding third-order dipolar effects in solution nuclear magnetic resonance: Hahn echo decays and intermolecular triple-quantum coherences. *Journal of Chemical Physics*;116(5):2075-2084.

81. Ahn S, Warren WS, Lee S. 1997 Quantum treatment of intermolecular multiple-quantum coherences with intramolecular J coupling in solution NMR. *Journal of Magnetic Resonance*;128(2):114-129.
82. Warren WS, Lee S, Richter W, Vathyam S. 1995 Correcting the classical dipolar demagnetizing field in solution NMR. *Chemical Physics Letters*;247(3):207-214.
83. Broekaert P, Vlassenbroek A, Jeener J, Lippens G, Wieruszeski JM. 1996 Observation and selective suppression of the dipolar-field effects in 2D NMR in liquids in homogeneous fields. *Journal of Magnetic Resonance*;120(1):97-104.
84. Bachiller PR, Ahn S, Warren WS. 1996 Detection of intermolecular heteronuclear multiple-quantum coherences in solution NMR. *Journal of Magnetic Resonance*;122(1):94-99.
85. Edzes HT. 1990 The Nuclear Magnetization as the Origin of Transient Changes in the Magnetic-Field in Pulsed NMR Experiments. *Journal of Magnetic Resonance*;86(2):293-303.
86. Deville G, Bernier M, Delrieux JM. 1979 NMR Multiple Echoes Observed in Solid He-3. *Physical Review B: Condensed Matter*;19(11):5666-5688.
87. Einzel D, Eska G, Hirayoshi Y, Kopp T, Wolfle P. 1984 Multiple Spin Echoes in a Normal Fermi-Liquid. *Physical Review Letters*;53(24):2312-2315.
88. Körber H, Dormann E, Eska G. 1991 Multiple spin echoes for protons in water. *Journal of Magnetic Resonance*;93:589-595.
89. Jones RPO, Morris GA, Waterton JC. 1992 Multiple Spin Echoes in a High-Resolution Spectrometer. *Journal of Magnetic Resonance*;98(1):115-122.
90. Bedford AS, Bowtell R, Bowley RM. 1991 Multiple Spin Echoes in Multicomponent Liquids. *Journal of Magnetic Resonance*;93(3):516-532.
91. Marques JP, Bowtell R. 2005 Application of a fourier-based method for rapid calculation of field inhomogeneity due to spatial variation of magnetic susceptibility. *Concepts in Magnetic Resonance*;25B(1):65-78.
92. Faber C, Pracht E, Haase A. 2003 Resolution enhancement in in vivo NMR spectroscopy: detection of intermolecular zero-quantum coherences. *Journal of Magnetic Resonance*;161(2):265-274.
93. Levitt MH. *Spin Dynamics: Basics of Nuclear Magnetic Resonance*: John Wiley & Sons, Ltd.; 2001.
94. Chen Z, Chen Z, Zhong J. IDEAL-II: Improved IDEAL (Intermolecular Dipolar Interaction Enhanced All Lines) Method for High-Resolution MRS in Inhomogeneous Fields. 2004; Kyoto, Japan. p 2300.
95. Chen Z, Chen ZW, Zhong JH. 2004 High-resolution NMR spectra in inhomogeneous fields via IDEAL (intermolecular dipolar-interaction enhanced all lines) method. *Journal of the American Chemical Society*;126(2):446-447.
96. Faber C. 2005 Solvent-localized NMR spectroscopy using the distant dipolar field: A method for NMR separations with a single gradient. *Journal of Magnetic Resonance*;176(1):120-124.
97. Weiss K, Melkus G, Jakob PM, Faber C. 2008 Quantitative in vivo ¹H spectroscopic imaging of metabolites in the early postnatal mouse brain at 17.6 T. *Magnetic Resonance Materials in Physics Biology and Medicine*;in press.
98. de Graaf RA, Brown PB, McIntyre S, Nixon TW, Behar KL, Rothman DL. 2006 High magnetic field water and metabolite proton T₁ and T₂ relaxation in rat brain in vivo. *Magnetic Resonance in Medicine*;56:386-394.
99. Reinoso R, Telfer B, Rowland M. 1997 Tissue water content in rats measured by desiccation. *Journal of Pharmacological and Toxicological Methods*;38:87-92.
100. Neuberger T, Webb A, Faber C, Behr VC, Neubauer S, Schneider JE. Measurement of T₁ relaxation times of major metabolites in the mouse brain at 11.7 and 17.6 Tesla

- using voxel-localized proton magnetic resonance spectroscopy. *Proceedings of the ISMRM 2006*.
101. Barros W, Gochberg DF. 2006 Fast single-gradient simultaneous measurement of D and T-2 in liquids via the distant dipolar field. *Chemical Physics Letters*;431(1-3):174-178.
102. Zhong JH, Chen Z, Kwok E, Kennedy S. 2001 Enhanced sensitivity to molecular diffusion with intermolecular double-quantum coherences: implications and potential applications. *Magnetic Resonance Imaging*;19(1):33-39.
103. Barros W, Gore JC, Gochberg DF. 2006 Simultaneous measurement of D and T-2 using the distant dipolar field. *Journal of Magnetic Resonance*;178(1):166-169.
104. Jeener J. 2002 Macroscopic molecular diffusion in liquid NMR, revisited. *Concepts in Magnetic Resonance*;14(2):79-88.
105. Meiboom S, Gill D. 1958 Modified Spin-Echo Method for Measuring Nuclear Relaxation Times. *The Review of Scientific Instruments*;29(8):688-691.
106. Carr HY, Purcell EM. 1954 Effects of Diffusion on Free Precession in Nuclear Magnetic Resonance Experiments. *Physical Review*;94(3):630-638.
107. Branca RT, Warren WS. 2009 Solvent suppression without crosspeak attenuation in iZQC experiments. *Chemical Physics Letters*;470:325-331.
108. Govindaraju V, Young K, Maudsley AA. 2000 Proton NMR chemical shifts and coupling constants for brain metabolites. *Nmr in Biomedicine*;13(3):129-153.
109. Bifone A, Payne GS, Leach MO. 1998 In vivo multiple spin echoes. *Journal of Magnetic Resonance*;135(1):30-36.
110. Mescher M, Richter W, DelaBarre L, Garwood M, Warren WS. Localized Spectroscopy with Intermolecular Zero Quantum Coherences: Phantom Results. *Proceedings of the ISMRM 2000*.
111. Hwang TL, Shaka AJ. 1995 Water Suppression that works. Excitation sculpting using arbitrary waveforms and pulses field gradients. *Journal of Magnetic Resonance*;112:275-279.
112. Behr VC, Weber T, Neuberger T, Vroemen M, Weidner N, Bogdahn U, Haase A, Jakob PM, Faber C. 2004 High-resolution MR imaging of the rat spinal cord in vivo in a wide-bore magnet at 17.6 Tesla. *Magnetic Resonance Materials in Physics Biology and Medicine*;17(3-6):353-358.
113. Guizar-Sahagun G, Rivera F, Babinski E, Berlanga E, Madrazo M, Francobourland R, Grijalva I, Gonzalez J, Contreras B, Madrazo I. 1994 Magnetic-Resonance-Imaging of the Normal and Chronically Injured Adult-Rat Spinal-Cord in-Vivo. *Neuroradiology*;36(6):448-452.
114. Fraidakis M, Klason T, Cheng H, Olson L, Spenger C. 1998 High-resolution MRI of intact and transected rat spinal cord. *Experimental Neurology*;153(2):299-312.
115. Meyerand ME, Cremillieux Y, Wadghiri YZ, Azzawi A, Hoopes PJ, Dunn JF. 1998 In vivo gradient echo microimaging of rodent spinal cord at 7 T. *Magnetic Resonance in Medicine*;40(5):789-791.
116. Franconi F, Lemaire L, Marescaux L, Jallet P, Le Jeune JJ. 2000 In vivo quantitative microimaging of rat spinal cord at 7T. *Magnetic Resonance in Medicine*;44(6):893-898.
117. Bonny JM, Gaviria M, Donnat JP, Jean B, Privat A, Renou JP. 2004 Nuclear magnetic resonance microimaging of mouse spinal cord in vivo. *Neurobiology of Disease*;15(3):474-482.
118. Weber T, Vroemen M, Behr V, Neuberger T, Jakob P, Haase A, Schuierer G, Bogdahn U, Faber C, Weidner N. 2006 In vivo high-resolution MR imaging of neuropathologic changes in the injured rat spinal cord. *American Journal of Neuroradiology*;27(3):598-604.

119. Flanders AE, Spettell CM, Tartaglino LM, Friedman DP, Herbison GJ. 1996 Forecasting motor recovery after cervical spinal cord injury: Value of MR imaging. *Radiology*;201(3):649-655.
120. Bilgen M, Abbe R, Liu SJ, Narayana PA. 2000 Spatial and temporal evolution of hemorrhage in the hyperacute phase of experimental spinal cord injury: In vivo magnetic resonance imaging. *Magnetic Resonance in Medicine*;43(4):594-600.
121. Narayana PA, Grill RJ, Chacko T, Vang R. 2004 Endogenous recovery of injured spinal cord: Longitudinal in vivo magnetic resonance imaging. *Journal of Neuroscience Research*;78(5):749-759.
122. Bilgen M, Al-Hafez B, Alrefae T, He Y-Y, Smirnova IV, Aldur MM, Festoff BW. 2007 Longitudinal magnetic resonance imaging of spinal cord injury in mouse: changes in signal patterns associated with the inflammatory response. *Magnetic Resonance Imaging*;25(5):657-664.
123. Callot V, Duhamel G, Cozzone PJ. 2007 In vivo mouse spinal cord imaging using echo-planar imaging at 11.75 T. *Magnetic Resonance Materials in Physics Biology and Medicine*; DOI: 10.1007/s10334-007-0079-x.
124. Teng YD, Lavik EB, Qu XL, Park KI, Ourednik J, Zurakowski D, Langer R, Snyder EY. 2002 Functional recovery following traumatic spinal cord injury mediated by a unique polymer scaffold seeded with neural stem cells. *Proceedings of the National Academy of Sciences of the United States of America*;99(5):3024-3029.
125. Okano H, Ogawa Y, Nakamura M, Kaneko S, Iwanami A, Toyama Y. 2003 Transplantation of neural stem cells into the spinal cord after injury. *Seminars in Cell & Developmental Biology*;14(3):191-198.
126. Pfeifer K, Vroemen M, Blesch A, Weidner N. 2004 Adult neural progenitor cells provide a permissive guiding substrate for corticospinal axon growth following spinal cord injury. *European Journal of Neuroscience*;20(7):1695-1704.
127. Prang P, Muller R, Eljaouhari A, Heckmann K, Kunz W, Weber T, Faber C, Vroemen M, Bogdahn U, Weidner N. 2006 The promotion of oriented axonal regrowth in the injured spinal cord by alginate-based anisotropic capillary hydrogels. *Biomaterials*;27(19):3560-3569.
128. Bulte JWM, Duncan ID, Frank JA. 2002 In vivo magnetic resonance tracking of magnetically labeled cells after transplantation. *Journal of Cerebral Blood Flow and Metabolism*;22(8):899-907.
129. Kendi ATK, Tan FU, Kendi M, Huvaj S, Tellioglu S. 2004 MR spectroscopy of cervical spinal cord in patients with multiple sclerosis. *Neuroradiology*;46(9):764-769.
130. Zelaya FO, Chalk JB, Mullins P, Brereton IM, Doddrell DM. 1996 Localized H-1 NMR spectroscopy of rat spinal cord in vivo. *Magnetic Resonance in Medicine*;35(4):443-448.
131. Cooke FJ, Blamire AM, Manners DN, Styles P, Rajagopalan B. 2004 Quantitative proton magnetic resonance spectroscopy of the cervical spinal cord. *Magnetic Resonance in Medicine*;51(6):1122-1128.
132. Marliani AF, Clementi V, Albini-Riccioli L, Agati R, Leonardi M. 2007 Quantitative proton magnetic resonance spectroscopy of the human cervical spinal cord at 3 Tesla. *Magnetic Resonance in Medicine*;57:160-163.
133. Bilgen M, Elshafiey I, Narayana PA. 2001 In vivo magnetic resonance microscopy of rat spinal cord at 7 T using implantable RF coils. *Magnetic Resonance in Medicine*;46(6):1250-1253.
134. Silver X, Ni WX, Mercer EV, Beck BL, Bossart EL, Inglis B, Mareci TH. 2001 In vivo H-1 magnetic resonance imaging and spectroscopy of the rat spinal cord using an inductively-coupled chronically implanted RF coil. *Magnetic Resonance in Medicine*;46(6):1216-1222.

-
135. Tkac I, Starcuk Z, Choi IY, Gruetter R. 1999 In vivo H-1 NMR spectroscopy of rat brain at 1 ms echo time. *Magnetic Resonance in Medicine*;41(4):649-656.
 136. Naressi A, Couturier C, Devos JM, Janssen M, Mangeat C, de Beer R, Graveron-Demilly D. 2001 Java-based graphical user interface for the MRUI quantitation package. *Magnetic Resonance Materials in Physics Biology and Medicine*;12(2-3):141-152.
 137. Friedrichs MS. 1995 A model-free algorithm for the removal of baseline artifacts. *Journal of Biomolecular NMR*;5(2):147-153.
 138. Vanhamme L, van den Boogaart A, Van Huffel S. 1997 Improved method for accurate and efficient quantification of MRS data with use of prior knowledge. *Journal of Magnetic Resonance*;129(1):35-43.
 139. Rangan SR. 1972 A new human cell line (FaDu) from a hypopharyngeal carcinoma. *Cancer*;29:117-121.
 140. Faber C, Heil C, Zahneisen B, Balla DZ, Bowtell R. 2006 Sensitivity to local dipole fields in the CRAZED experiment: An approach to bright spot MRI. *Journal of Magnetic Resonance*;182:315-324.
 141. Shannon KL, Branca RT, Galiana G, Cenzano S, Bouchard LS, Soboyejo W, Warren WS. 2004 Simultaneous acquisition of multiple orders of intermolecular multiple-quantum coherence images in vivo. *Magnetic Resonance Imaging*;22(10):1407-1412.
 142. Enss T, Ahn S, Warren WS. 1999 Visualizing the dipolar field in solution NMR and MR imaging: three-dimensional structure simulations. *Chemical Physics Letters*;305(1-2):101-108.
 143. Garrett-Roe S, Warren WS. 2000 Numerical studies of intermolecular multiple quantum coherences: High-resolution NMR in inhomogeneous fields and contrast enhancement in MRI. *Journal of Magnetic Resonance*;146(1):1-13.
 144. Dormand JR, Prince PJ. 1980 A family of embedded Runge-Kutta formulae. *Journal of Computational and Applied Mathematics*;6:19-26.

Appendix A

The steps leading to Eq.[3.19] will be described here (27,78). After the second β -pulse, the longitudinal and transverse magnetizations are

$$\begin{aligned} M_z(t_2 = 0) &= -\sin \beta \left[M_0^I \cos(\Delta\omega_I t_1 + k_m s) + M_0^S \cos(\Delta\omega_S t_1 + k_m s) \right] \\ M^{I+}(t_2 = 0) &= M_y^I + iM_x^I = M_0^I \left[\cos \beta \cos(\Delta\omega_I t_1 + k_m s) + i \sin(\Delta\omega_I t_1 + k_m s) \right] \\ M^{S+}(t_2 = 0) &= M_y^S + iM_x^S = M_0^S \left[\cos \beta \cos(\Delta\omega_S t_1 + k_m s) + i \sin(\Delta\omega_S t_1 + k_m s) \right]. \end{aligned} \quad [A.1]$$

During t_2 , transverse magnetization evolves as described by Eq. [3.17], and therefore after t_2 we have

$$\begin{aligned} M_z(t_2) &= -\sin \beta \left[M_0^I \cos(\Delta\omega_I t_1 + k_m s) + M_0^S \cos(\Delta\omega_S t_1 + k_m s) \right] \\ M^+(t_2) &= M_0^I \left[\cos \beta \cos(\Delta\omega_I t_1 + k_m s) + i \sin(\Delta\omega_I t_1 + k_m s) \right] e^{i \left[\Delta\omega_I t_2 + \gamma \left(B_{DDF}^I + \frac{2}{3} B_{DDF}^S \right) t_2 \right]} \\ &\quad + M_0^S \left[\cos \beta \cos(\Delta\omega_S t_1 + k_m s) + i \sin(\Delta\omega_S t_1 + k_m s) \right] e^{i \left[\Delta\omega_S t_2 + \gamma \left(B_{DDF}^S + \frac{2}{3} B_{DDF}^I \right) t_2 \right]}. \end{aligned} \quad [A.2]$$

By replacing (see Eq. [3.16])

$$B_{DDF}^{I,S} = -\sin \beta \Delta_s \mu_0 M_0^{I,S} \cos(\Delta\omega_{I,S} t_1 + k_m s), \quad [A.3]$$

we get

$$\begin{aligned} M^+(t_2) &= M_0^I \left[\cos \beta \cos(\Delta\omega_I t_1 + k_m s) + i \sin(\Delta\omega_I t_1 + k_m s) \right] \\ &\quad \times \exp i \left\{ \Delta\omega_I t_2 - \sin \beta \left[\tau_{dl}^{-1} \cos(\Delta\omega_I t_1 + k_m s) + \frac{2}{3} \tau_{ds}^{-1} \cos(\Delta\omega_S t_1 + k_m s) \right] t_2 \right\} \\ &\quad + M_0^S \left[\cos \beta \cos(\Delta\omega_S t_1 + k_m s) + i \sin(\Delta\omega_S t_1 + k_m s) \right] \\ &\quad \times \exp i \left\{ \Delta\omega_S t_2 - \sin \beta \left[\tau_{ds}^{-1} \cos(\Delta\omega_S t_1 + k_m s) + \frac{2}{3} \tau_{dl}^{-1} \cos(\Delta\omega_I t_1 + k_m s) \right] t_2 \right\}, \end{aligned} \quad [A.4]$$

where $\tau_{dl,S} = (\gamma \mu_0 M_0^{I,S})^{-1}$. Using the relations $\cos A = (e^{iA} + e^{-iA})/2$ and $\sin A = (e^{iA} - e^{-iA})/2i$, we do the regrouping

$$\begin{aligned} \cos(\Delta\omega_{I,S} t_1 + k_m s) + i \sin(\Delta\omega_{I,S} t_1 + k_m s) &\rightarrow \\ \frac{e^{i(\Delta\omega_{I,S} t_1 + k_m s)} + e^{-i(\Delta\omega_{I,S} t_1 + k_m s)}}{2} + \frac{e^{i(\Delta\omega_{I,S} t_1 + k_m s)} - e^{-i(\Delta\omega_{I,S} t_1 + k_m s)}}{2}, \end{aligned} \quad [A.5]$$

and by using the Jacobi-Anger expansion $e^{i\xi\cos\phi} = \sum_{l=-\infty}^{\infty} i^l J_l(\xi) e^{il\phi}$, where J_l is a Bessel-function of the first kind, we get

$$e^{i\left\{\Delta\omega_{1,s}t_2 - \sin\beta\Delta_s\left[\tau_{dl,s}^{-1}\cos(\Delta\omega_{1,s}t_1 + k_ms) + \frac{2}{3}\tau_{ds,I}^{-1}\cos(\Delta\omega_{s,I}t_1 + k_ms)\right]t_2\right\}} \rightarrow$$

$$e^{i\Delta\omega_{1,s}t_2} \times \sum_{p=-\infty}^{\infty} i^p J_p\left(-\frac{\sin\beta\Delta_s t_2}{\tau_{dl,s}}\right) e^{ip(\Delta\omega_{1,s}t_1 + k_ms)} \times \sum_{l=-\infty}^{\infty} i^l J_l\left(-\frac{2}{3}\frac{\sin\beta\Delta_s t_2}{\tau_{ds,I}}\right) e^{il(\Delta\omega_{s,I}t_1 + k_ms)}. \quad [A.6]$$

Thus,

$$M^+(t_2) = \frac{M_0^I}{2} \left\{ \cos\beta \left[e^{i(\Delta\omega_{1,t_1} + k_ms)} + e^{-i(\Delta\omega_{1,t_1} + k_ms)} \right] + \left[e^{i(\Delta\omega_{1,t_1} + k_ms)} - e^{-i(\Delta\omega_{1,t_1} + k_ms)} \right] \right\} e^{i\Delta\omega_{1,t_2}}$$

$$\times \sum_{p=-\infty}^{\infty} i^p J_p\left(-\sin\beta\Delta_s t_2/\tau_{dl}\right) e^{ip(\Delta\omega_{1,t_1} + k_ms)} \times \sum_{l=-\infty}^{\infty} i^l J_l\left(-\frac{2}{3}\sin\beta\Delta_s t_2/\tau_{ds}\right) e^{il(\Delta\omega_{s,t_1} + k_ms)}$$

$$+ \frac{M_0^S}{2} \left\{ \cos\beta \left[e^{i(\Delta\omega_{s,t_1} + k_ms)} + e^{-i(\Delta\omega_{s,t_1} + k_ms)} \right] + \left[e^{i(\Delta\omega_{s,t_1} + k_ms)} - e^{-i(\Delta\omega_{s,t_1} + k_ms)} \right] \right\} e^{i\Delta\omega_{s,t_2}}$$

$$\times \sum_{q=-\infty}^{\infty} i^q J_q\left(-\sin\beta\Delta_s t_2/\tau_{ds}\right) e^{iq(\Delta\omega_{s,t_1} + k_ms)} \times \sum_{n=-\infty}^{\infty} i^n J_n\left(-\frac{2}{3}\sin\beta\Delta_s t_2/\tau_{dl}\right) e^{in(\Delta\omega_{1,t_1} + k_ms)}. \quad [A.7]$$

Spatial averaging across the sample eliminates all terms that depend on the absolute spatial phase. To find the effect of the spatial modulation imposed by CG, we collect all the position-dependent terms as follows:

$$(e^{ik_ms} \pm e^{-ik_ms}) \times \sum_p e^{ipk_ms} \times \sum_l e^{ilk_ms} = \sum_p \sum_l \left\{ e^{i[(1+p+l)k_ms]} \pm e^{i[(-1+p+l)k_ms]} \right\}. \quad [A.8]$$

and similarly for the term including q and n . In order to survive spatial averaging, one of the terms in the double sum must be constant with respect to position and therefore it must have a coefficient of zero for the s -direction:

$$1 + p + l = 0, \quad [A.9]$$

or

$$-1 + p + l = 0. \quad [A.10]$$

Only pairs with $(p, l) = \{(-k, k \pm 1), k \in \mathbb{Z}\}$ satisfy this condition. Subsequently using the Bessel function identities $J_{-n}(\xi) = (-1)^n J_n(\xi)$, $J_{n-1}(\xi) + J_{n+1}(\xi) = \frac{2n}{\xi} J_n(\xi)$,

$J_{n-1}(\xi) - J_{n+1}(\xi) = 2J'_n(\xi)$, and $J'_n(\xi) = J_{n-1}(\xi) - \frac{n}{\xi} J_n(\xi)$ we obtain Eq. [3.19].

Appendix B

Derivation of Eq. [4.9] is presented here in analogy to the approach in Appendix A, but for a $\beta = 90^\circ$ pulse selecting the I-spins (37). We start the analysis at the time point immediately after β :

$$M_z(t_2 = 0) = -M_0^I \cos(\Delta\omega_1 t_1 + k_m s)$$

$$M^{I+}(t_2 = 0) = iM_x^I = iM_0^I \sin(\Delta\omega_1 t_1 + k_m s)$$

$$M^{S+}(t_2 = 0) = M_0^S e^{i(\Delta\omega_S t_1 + k_m s)}. \quad [B.1]$$

After evolution in t_2 under the action of chemical shift and DDF, the transverse magnetization can be written as

$$M^+(t_2) = iM_0^I \sin(\Delta\omega_1 t_1 + k_m s) e^{i\left[\Delta\omega_1 t_2 + \gamma\left(B_{DDF}^I + \frac{2}{3}B_{DDF}^S\right)t_2\right]} + M_0^S e^{i(\Delta\omega_S t_1 + k_m s)} e^{i\left[\Delta\omega_S t_2 + \gamma\left(B_{DDF}^S + \frac{2}{3}B_{DDF}^I\right)t_2\right]}, \quad [B.2]$$

where

$$B_{DDF}^I = \Delta_z \mu_0 M_z(t_2), \quad [B.3]$$

with $M_z(t_2) = M_z(t_2 = 0)$, and

$$B_{DDF}^S = 0. \quad [B.4]$$

Therefore Eq. [B.2] can be rewritten as

$$M^+(t_2) = iM_0^I \sin(\Delta\omega_1 t_1 + k_m s) e^{i[\Delta\omega_1 t_2 + \gamma\Delta_z M_z t_2]} + M_0^S e^{i(\Delta\omega_S t_1 + k_m s)} e^{i\left[\Delta\omega_S t_2 + \gamma\frac{2}{3}\Delta_z M_z t_2\right]}, \quad [B.5]$$

which, after replacing M_z with the term given in Eq. [B.1], and by using the relation $\sin A = (e^{iA} - e^{-iA})/2i$, takes the form

$$M^+(t_2) = M_0^I \frac{e^{i(\Delta\omega_1 t_1 + k_m s)} - e^{-i(\Delta\omega_1 t_1 + k_m s)}}{2} e^{i[\Delta\omega_1 t_2 + \gamma\Delta_z M_z t_2]} + M_0^S e^{i(\Delta\omega_S t_1 + k_m s)} e^{i\Delta\omega_S t_2} e^{-i\gamma\frac{2}{3}\Delta_z M_0^I \cos(\Delta\omega_1 t_1 + k_m s)t_2}. \quad [B.6]$$

Knowing that $e^{i\xi \cos \phi} = \sum_{l=-\infty}^{\infty} i^l J_l(\xi) e^{il\phi}$, we get

$$M^+(t_2) = \frac{1}{2} M_0^I \left(e^{i(\Delta\omega_1 t_1 + k_m s)} - e^{-i(\Delta\omega_1 t_1 + k_m s)} \right) e^{i\Delta\omega_2 t_2} \sum_{n=-\infty}^{\infty} i^n J_n \left(-\frac{\Delta_s t_2}{\tau_{dl}} \right) e^{in(\Delta\omega_1 t_1 + k_m s)}$$

$$+ M_0^S e^{i(\Delta\omega_8 t_1 + k_m s)} e^{i\Delta\omega_8 t_2} \sum_{p=-\infty}^{\infty} i^p J_p \left(-\frac{2}{3} \frac{\Delta_s t_2}{\tau_{dl}} \right) e^{ip(\Delta\omega_1 t_1 + k_m s)}, \quad [B.7]$$

which is

$$\begin{aligned} M^+(t_2) = & \frac{1}{2} M_0^I e^{i\Delta\omega_2 t_2} \sum_{n=-\infty}^{\infty} i^n J_n \left(-\frac{\Delta_s t_2}{\tau_{dl}} \right) \left[e^{i(n+1)(\Delta\omega_1 t_1 + k_m s)} - e^{i(n-1)(\Delta\omega_1 t_1 + k_m s)} \right] \\ & + M_0^S e^{i\Delta\omega_8 t_2} \sum_{p=-\infty}^{\infty} i^p J_p \left(-\frac{2}{3} \frac{\Delta_s t_2}{\tau_{dl}} \right) e^{i[(p\Delta\omega_1 + \Delta\omega_8)t_1 + (p+1)k_m s]}. \end{aligned} \quad [B.8]$$

However, spatial averaging will cancel out every term in the sums, except for those, the coefficients of which are solutions of the following equations:

$$n + 1 = 0, \quad [B.9]$$

or

$$n - 1 = 0, \quad [B.10]$$

and

$$p + 1 = 0. \quad [B.11]$$

These conditions are fulfilled only for $n = -1$ or $+1$, and $p = -1$, so that

$$\begin{aligned} M^+(t_2) = & \frac{1}{2} M_0^I e^{i\Delta\omega_2 t_2} \overbrace{\left[i^{-1} J_{-1} \left(-\frac{\Delta_s t_2}{\tau_{dl}} \right) - i^{+1} J_{+1} \left(-\frac{\Delta_s t_2}{\tau_{dl}} \right) \right]}^0 \\ & + M_0^S e^{i\Delta\omega_8 t_2} e^{i(\Delta\omega_8 - \Delta\omega_1)t_1} i^{-1} J_{-1} \left(-\frac{2}{3} \frac{\Delta_s t_2}{\tau_{dl}} \right). \end{aligned} \quad [B.12]$$

Since $J_{-n}(\xi) = (-1)^n J_n(\xi)$ the transverse magnetization for a selective $\beta = 90^\circ$ after the evolution in t_2 has the final form given in Eq. [4.9].

Appendix C

If considering relaxation processes during the evolution of the magnetization in a SEL-HOMOGENIZED sequence, the solution is given by Eq. [4.10]. Here I present the derivation steps leading to this equation, starting at time point $t_2 = 0$ and assuming that $t_1 \ll T_1^{LS}$:

$$\begin{aligned} M_z(t_2 = 0) &= -M_0^I \cos(\Delta\omega_1 t_1 + k_m s) e^{-t_1/T_2^I} \\ M^{I+}(t_2 = 0) &= iM_x^I = iM_0^I \sin(\Delta\omega_1 t_1 + k_m s) e^{-t_1/T_2^I} \\ M^{S+}(t_2 = 0) &= M_0^S e^{i(\Delta\omega_S t_1 + k_m s)} e^{-t_1/T_2^S}. \end{aligned} \quad [C.1]$$

Relaxation creates additional terms in the modified Bloch-equations, so that we have

$$\frac{dM_z}{dt_2} = -\frac{M_z - M_0^I}{T_1^I}, \quad [C.2]$$

and

$$\begin{aligned} \frac{dM^+}{dt_2} &= i\gamma M^{I+} \left[B_{DDF}^I + \gamma^{-1} (\Delta\omega_1 + k_m s) \right] - \frac{M^{I+}}{T_2^I} \\ &\quad + i\gamma M^{S+} \left[\frac{2}{3} B_{DDF}^I + \gamma^{-1} (\Delta\omega_S + k_m s) \right] - \frac{M^{S+}}{T_2^S}. \end{aligned} \quad [C.3]$$

The solution of Eq. [C.2] for the longitudinal magnetization is

$$\begin{aligned} M_z(t_2) &= M_z(t_2 = 0) e^{-t_2/T_1^I} + M_0^I (1 - e^{-t_2/T_1^I}) \\ &= -M_0^I \cos(\Delta\omega_1 t_1 + k_m s) e^{-t_1/T_2^I} e^{-t_2/T_1^I} + M_0^I (1 - e^{-t_2/T_1^I}). \end{aligned} \quad [C.4]$$

The second term in Eq. [C.4] does not contain any spatially modulated terms and can be left out in further calculations, because it produces only a slight phase shift in the observed signal. We get the Bloch-equation for the evolution of the transverse magnetization after substituting Eq. [C.4] into Eq. [C.3]:

$$\begin{aligned} \frac{dM^+}{dt_2} &= -M^{I+} \frac{i\Delta_s}{\tau_{dl}} \cos(\Delta\omega_1 t_1 + k_m s) e^{-t_1/T_2^I} e^{-t_2/T_1^I} - \frac{M^{I+}}{T_2^I} \\ &\quad - M^{S+} \frac{2}{3} \frac{i\Delta_s}{\tau_{dl}} \cos(\Delta\omega_1 t_1 + k_m s) e^{-t_1/T_2^I} e^{-t_2/T_1^I} - \frac{M^{S+}}{T_2^S}. \end{aligned} \quad [C.5]$$

The solutions of Eq. [C.5] are

$$\ln \left[\frac{M^{I+}(t_2)}{M^{I+}(0)} \right] = \int_0^{t_2} dt_2' \left[-\frac{i\Delta_s}{\tau_{dl}} \cos(\Delta\omega_1 t_1 + k_m s) e^{-t_1/T_2^I} e^{-t_2'/T_1^I} - \frac{1}{T_2^I} \right]$$

$$= -\frac{i\Delta_s}{\tau_{dl}} \cos(\Delta\omega_1 t_1 + k_m s) e^{-t_1/T_2^I} \left(1 - e^{-t_2/T_1^I}\right) T_1^I - \frac{t_2}{T_2^I}, \quad [C.6]$$

and

$$\begin{aligned} \ln \left[\frac{M^{S+}(t_2)}{M^{S+}(0)} \right] &= \int_0^{t_2} dt_2' \left[-\frac{2}{3} \frac{i\Delta_s}{\tau_{dl}} \cos(\Delta\omega_1 t_1 + k_m s) e^{-t_1/T_2^I} e^{-t_2'/T_1^I} - \frac{1}{T_2^S} \right] \\ &= -\frac{2}{3} \frac{i\Delta_s}{\tau_{dl}} \cos(\Delta\omega_1 t_1 + k_m s) e^{-t_1/T_2^I} \left(1 - e^{-t_2/T_1^I}\right) T_1^I - \frac{t_2}{T_2^S}. \end{aligned} \quad [C.7]$$

Substituting Eq. [C.1] into Eqs. [C.6] and [C.7] we get

$$\begin{aligned} M^{I+}(t_2) &= iM_0^I \sin(\Delta\omega_1 t_1 + k_m s) e^{-t_1/T_2^I} e^{-\frac{i\Delta_s}{\tau_{dl}} \cos(\Delta\omega_1 t_1 + k_m s) e^{-t_1/T_2^I} \left(1 - e^{-t_2/T_1^I}\right) T_1^I - \frac{t_2}{T_2^I}} \\ &= iM_0^I \sin(\Delta\omega_1 t_1 + k_m s) e^{-(t_1+t_2)/T_2^I} e^{i\xi \cos(\Delta\omega_1 t_1 + k_m s)}, \end{aligned} \quad [C.8]$$

and

$$M^{S+}(t_2) = M_0^S e^{i(\Delta\omega_s t_1 + k_m s)} e^{-(t_1+t_2)/T_2^S} e^{i\frac{2}{3}\xi \cos(\Delta\omega_1 t_1 + k_m s)} \quad [C.9]$$

where

$$\xi = -\frac{\Delta_s}{\tau_{dl}} e^{-t_1/T_2^I} \left(1 - e^{-t_2/T_1^I}\right) T_1^I. \quad [C.10]$$

Following further the steps 6 to 12 from Appendix B we finally get Eq. [4.10].

Appendix D

For the pulse sequence in Fig. 4.13 the longitudinal magnetization outside the voxel after the second pulse is

$$M_z(T_{Sp}^-) = M_0^I \cos(\Delta\omega_I t_p + \phi_{Spoiler}) + M_0^S \cos(\Delta\omega_S t_p + \phi_{Spoiler}), \quad [D.1]$$

where $\phi_{Spoiler} = \sum_{Spoiler} \gamma G_{Sp} T_{Sp} s$. Equation [D.1] is valid for those regions in the sample experiencing two, four, or six spoiler gradients. At the end of the period t_1 containing the CG, with $\phi_{CG} = \gamma G T z$, the magnetization can be written as

$$\begin{aligned} M_z(t_1) &= 0, \\ M^+(t_1) &= M_0^I \cos(\Delta\omega_I t_p + \phi_{Spoiler}) e^{i(\Delta\omega_I t_1 + \phi_{CG})} \\ &\quad + M_0^S \cos(\Delta\omega_S t_p + \phi_{Spoiler}) e^{i(\Delta\omega_S t_1 + \phi_{CG})}, \end{aligned} \quad [D.2]$$

if gradient dephasing and diffusion during T_{Sp} totally spoil transverse magnetization and Δ_s during t_p is zero as a result of the magic angle modulation. After the last 90° frequency selective pulse on I spins the longitudinal magnetization is

$$M_z(t_2^-) = -M_0^I \cos(\Delta\omega_I t_p + \phi_{Spoiler}) \cos(\Delta\omega_I t_1 + \phi_{CG}) \quad [D.3]$$

and the transverse magnetization during t_2 evolves into

$$\begin{aligned} M^+(t_2) &= M_0^S \cos(\Delta\omega_S t_p + \phi_{Spoiler}) e^{i(\Delta\omega_I t_1 + \phi_{CG})} \\ &\quad \times e^{i\Delta\omega_S t_2} e^{-i\frac{2}{3}\gamma\mu_0 M_0^I \Delta_s t_2 \cos(\Delta\omega_I t_p + \phi_{Spoiler}) \cos(\Delta\omega_I t_1 + \phi_{CG})} \\ &\quad + iM_0^I \cos(\Delta\omega_I t_p + \phi_{Spoiler}) \sin(\Delta\omega_I t_1 + \phi_{CG}) \\ &\quad \times e^{i\Delta\omega_I t_2} e^{-i\gamma\mu_0 M_0^I \Delta_s t_2 \cos(\Delta\omega_I t_2 + \phi_{Spoiler}) \cos(\Delta\omega_I t_1 + \phi_{CG})}. \end{aligned} \quad [D.4]$$

Using the identities $\tau_{dl} = (\gamma\mu_0 M_0^I)^{-1}$, $\cos A = (e^{iA} + e^{-iA})/2$, $\sin A = (e^{iA} - e^{-iA})/2i$ and $\cos A \cos B = [\cos(A+B) + \cos(A-B)]/2$, the expression in Eq. [D.4] can be transformed into

$$\begin{aligned} M^+(t_2) &= M_0^S \frac{e^{i(\Delta\omega_S t_p + \phi_{Spoiler})} + e^{-i(\Delta\omega_S t_p + \phi_{Spoiler})}}{2} e^{i(\Delta\omega_S t_1 + \phi_{CG})} e^{i\Delta\omega_S t_2} \\ &\quad \times e^{-i\frac{2}{3}\frac{\Delta_s t_2}{\tau_{dl}} \cos\left[\frac{(\Delta\omega_I t_p + \phi_{Spoiler}) + (\Delta\omega_I t_1 + \phi_{CG})}{2}\right]} e^{-i\frac{2}{3}\frac{\Delta_s t_2}{\tau_{dl}} \cos\left[\frac{(\Delta\omega_I t_p + \phi_{Spoiler}) - (\Delta\omega_I t_1 + \phi_{CG})}{2}\right]} \end{aligned}$$

$$\begin{aligned}
& +iM_0^1 \frac{e^{i(\Delta\omega_1 t_p + \phi_{\text{Spoiler}})} + e^{-i(\Delta\omega_1 t_p + \phi_{\text{Spoiler}})}}{2} \frac{e^{i(\Delta\omega_1 t_1 + \phi_{\text{CG}})} - e^{-i(\Delta\omega_1 t_1 + \phi_{\text{CG}})}}{2i} e^{i\Delta\omega_1 t_2} \\
& \times e^{-i \frac{\Delta_s t_2}{\tau_{\text{dl}}} \cos\left[\frac{(\Delta\omega_1 t_p + \phi_{\text{Spoiler}}) + (\Delta\omega_1 t_1 + \phi_{\text{CG}})}{2}\right]} e^{-i \frac{\Delta_s t_2}{\tau_{\text{dl}}} \cos\left[\frac{(\Delta\omega_1 t_p + \phi_{\text{Spoiler}}) - (\Delta\omega_1 t_1 + \phi_{\text{CG}})}{2}\right]}.
\end{aligned} \tag{D.5}$$

Using the Jacobi-Anger expansion, $e^{i\xi \cos \phi} = \sum_{l=-\infty}^{\infty} i^l J_l(\xi) e^{il\phi}$, gives

$$\begin{aligned}
M^+(t_2) &= \frac{M_0^S}{2} \left[e^{i(\Delta\omega_s t_p + \phi_{\text{Spoiler}})} + e^{-i(\Delta\omega_s t_p + \phi_{\text{Spoiler}})} \right] e^{i(\Delta\omega_s t_1 + \phi_{\text{CG}})} e^{i\Delta\omega_s t_2} \\
&\times \sum_{m=-\infty}^{\infty} i^m J_m \left(-\frac{\Delta_s t_2}{3\tau_{\text{dl}}} \right) e^{im[(\Delta\omega_1 t_p + \phi_{\text{Spoiler}}) + (\Delta\omega_1 t_1 + \phi_{\text{CG}})]} \\
&\times \sum_{l=-\infty}^{\infty} i^l J_l \left(-\frac{\Delta_s t_2}{3\tau_{\text{dl}}} \right) e^{il[(\Delta\omega_1 t_p + \phi_{\text{Spoiler}}) - (\Delta\omega_1 t_1 + \phi_{\text{CG}})]} \\
&+ \frac{M_0^I}{4} \left[e^{i(\Delta\omega_s t_p + \phi_{\text{Spoiler}})} + e^{-i(\Delta\omega_s t_p + \phi_{\text{Spoiler}})} \right] \left[e^{i(\Delta\omega_1 t_1 + \phi_{\text{CG}})} - e^{-i(\Delta\omega_1 t_1 + \phi_{\text{CG}})} \right] e^{i\Delta\omega_1 t_2} \\
&\times \sum_{k=-\infty}^{\infty} i^k J_k \left(-\frac{\Delta_s t_2}{2\tau_{\text{dl}}} \right) e^{ik[(\Delta\omega_1 t_p + \phi_{\text{Spoiler}}) + (\Delta\omega_1 t_1 + \phi_{\text{CG}})]} \\
&\times \sum_{p=-\infty}^{\infty} i^p J_p \left(-\frac{\Delta_s t_2}{2\tau_{\text{dl}}} \right) e^{ip[(\Delta\omega_1 t_p + \phi_{\text{Spoiler}}) - (\Delta\omega_1 t_1 + \phi_{\text{CG}})]}.
\end{aligned} \tag{D.6}$$

The second term in Eq. [D.6] gives rise to signals at solvent frequency ($\Delta\omega_1$) along the directly detected dimension and will be observed as residual water signal. The first term in Eq. [D.6] gives rise to solute peaks that may overlap signal from the selected voxel. The position-dependent terms in the function modulating the transverse magnetization of the I spins can be regrouped as

$$\begin{aligned}
& (e^{i\phi_{\text{Spoiler}}} + e^{-i\phi_{\text{Spoiler}}}) e^{i\phi_{\text{CG}}} \times \sum_m e^{im(\phi_{\text{Spoiler}} + \phi_{\text{CG}})} \sum_l e^{il(\phi_{\text{Spoiler}} - \phi_{\text{CG}})} = \\
& \left\{ \sum_m e^{i(m+1)(\phi_{\text{Spoiler}} + \phi_{\text{CG}})} + \sum_m e^{i[(m-1)\phi_{\text{Spoiler}} + (m+1)\phi_{\text{CG}}]} \right\} \times \sum_l e^{il(\phi_{\text{Spoiler}} - \phi_{\text{CG}})} = \\
& \sum_m \sum_l e^{i[(m+1+l)\phi_{\text{Spoiler}} + (m-l+1)\phi_{\text{CG}}]} + \sum_m \sum_l e^{i[(m+1-l)\phi_{\text{Spoiler}} + (m-l+1)\phi_{\text{CG}}]}
\end{aligned} \tag{D.7}$$

In order to survive spatial averaging, one of the sums in Eq. [4.15] must have a total coefficient of zero, which is the case for $(m, l) \in \{(-1, 0); (0, 1)\}$. Thus outside the selected voxel, the part of M_0^S that is refocused by the DDF is given by

$$\begin{aligned}
M^+(t_2) = & i \frac{M_0^S}{2} e^{i(\Delta\omega_S - \Delta\omega_I)(t_P + t_1)} e^{i\Delta\omega_S t_2} J_1\left(-\frac{\Delta_s t_2}{3\tau_{dl}}\right) J_0\left(-\frac{\Delta_s t_2}{3\tau_{dl}}\right) \\
& + i \frac{M_0^S}{2} e^{i(\Delta\omega_I - \Delta\omega_S)(t_P - t_1)} e^{i\Delta\omega_S t_2} J_1\left(-\frac{\Delta_s t_2}{3\tau_{dl}}\right) J_0\left(-\frac{\Delta_s t_2}{3\tau_{dl}}\right).
\end{aligned} \tag{D.8}$$

Curriculum vitae

Personal information

Dávid Zsolt Balla

Born on the 26th of April 1979 in Oradea, Romania

Nationality: Hungarian

Married

Research scientist at the Max Planck Institute for Biological Cybernetics, Tübingen

Education

10/2003 – 03/2007	PhD-Student in Würzburg
11/2002 – 09/2003	Research assistant in Würzburg
10/2002	Physics “Diplom” in Würzburg
06/2001	Medical-physics “Diplomă” in Cluj
11/2000 – 10/2002	Physics student at the Julius-Maximilians University in Würzburg
10/1997 – 11/2000	Medical-physics student at the Babeş-Bolyai University in Cluj, Romania

Würzburg, 2nd of November 2009

(David Balla)

Publication record

Scientific articles

D. Z. Balla, C. Faber: Intermolecular zero-quantum coherence NMR spectroscopy in the presence of local dipole fields, *Journal of Chemical Physics* 128:154522 (2008)

D. Z. Balla, C. Faber: Localized intermolecular zero-quantum coherence spectroscopy in vivo, *Concepts in Magnetic Resonance A* 32A:117-133 (2008)

D. Z. Balla, C. Faber: In vivo intermolecular zero-quantum coherence MR spectroscopy in the rat spinal cord at 17.6T: a feasibility study, *Magnetic Resonance Materials in Physics Biology and Medicine (MAGMA)* 20:183-191 (2007)

D. Z. Balla, G. Melkus, C. Faber: Spatially localized intermolecular zero-quantum coherence spectroscopy for in vivo applications, *Magnetic Resonance in Medicine* 56(4):745-753 (2006)

C. Faber, C. Heil, B. Zahneisen, D. Z. Balla, and R. Bowtell: Sensitivity to local dipole fields in the CRAZED Experiment: An approach to bright spot MRI, *Journal of Magnetic Resonance* 182:315-324 (2006)

D. Balla, C. Faber: Solvent suppression in liquid state NMR with selective intermolecular zero-quantum coherences, *Chemical Physics Letters* 393:464-469 (2004)

Conference abstracts

D. Z. Balla, H. M. Wiesner, G. Shajan, and R. Pohmann: Functional MRI in the rat brain with single-shot gradient echo EPI at 16.4 T, ISMRM 2009, Honolulu

D. Z. Balla, H. M. Wiesner, G. Shajan, C. Faber and R. Pohmann: TurboCRAZED BOLD imaging detects specific activation in the rat brain after somatosensory stimulation at 16.4 Tesla, ISMRM 2009, Honolulu

H. M. Wiesner, D. Z. Balla, R. Pohmann, W. Chen, K. Ugurbil, and K. Uludag: 17O T1/T2* tissue-relaxation rates with anatomical contrast in the rat brain at 16.4 T, ISMRM 2009, Honolulu

D. Z. Balla, C. Faber, J. Schneider, G. Shajan, R. Pohmann: Strong BOLD-effect with TurboCRAZED MRI following hyperoxia in the rat brain at 16.4 T, ESMRMB 2008, Valencia

Shajan, G., D. Z. Balla, J. Hoffmann and R. Pohmann: A Microstrip Resonator for Animal MRI at 16.4 T, ESMRMB 2008, Valencia

D. Z. Balla, S.-T. Hong, G. Shajan, R. Pohmann and K. Ugurbil: Single voxel MR spectroscopy with echo times below 2 ms at 16.4 T in the rat brain: first in vivo results, ISMRM 2008, Toronto

D. Z. Balla, C. Faber: Prospects of resolution and sensitivity enhancement using in vivo iZQC MR spectroscopy, ISMRM – ESMRMB 2007, Berlin

C. Faber, B. Zahneisen, C. Heil, D. Z. Balla, R. Bowtell: A new approach to bright spot MRI: visualizing local dipolar fields with the CRAZED sequence, ISMRM 2006, Seattle

D. Balla, C. Faber: SNR gain with localized iZQC spectroscopy in tumors in vivo, International Symposium on Biomedical Magnetic Resonance Imaging and Spectroscopy at Very High Fields 2006, Würzburg

D. Balla, C. Faber: Localized Intermolecular Zero-Quantum Coherence Spectroscopy in vivo, ENC 2005, Rhode Island

D. Balla, C. Faber: 2D iZQC in vivo spectroscopy with optimized pulse sequences: water suppression and localization, ISMRM 2004, Kyoto

C. Faber, D. Balla: Water suppression in 2D iZQC spectroscopy for in vivo application, ENC 2004, Asilomar

Acknowledgement

This PhD thesis is the result of four years of experimental work in Würzburg and the following instructive collaboration with my supervisors during data analysis and the preparation of the dissertation.

I am grateful for the uninterrupted and active support of Prof. Conny Faber. His impulses and influence rectified the way I elaborate scientific studies, and were the main reason for I could develop and prosper during my time as a PhD-student. I am also indebted to Prof. Peter Jakob, who gave me the opportunity to work and learn in his department, travel to conferences and have a great time on those notorious Ski-Seminars.

Since the results presented in this dissertation were often not been possible to produce without assistance, I would like to thank my colleagues who gave me a helping hand. I treasure the lovely memory of Lissi Höfer. Hers and Sebastian Außenhofer's professional technical assistance in the experimental setup was essential for the success of the measurements. Many thanks go to Dr. Volker Behr for the best service on computer networks and MR-hardware. I appreciate the kind favor of Gerd Melkus and Philipp Mörchel for giving me the chance to attach my measurements to theirs and collect great data. Further on, I would like to thank Dr. Armin Porea, Sabine Voll, Dr. Thomas Neuberger and Dr. Ed Pracht for their contribution around the experiments.

Many people helped during the preparation of my publications. I am indebted to Dr. Rolf Pohmann for his support in finalizing this thesis and proofreading some of the research articles. Thanks to Dr. Nicole Seiberlich for the correction of all those papers and abstracts with a lot of genglish. Dr. Robin Heidemann, Prof. Mark Griswold, Dr. Felix Breuer and Dr. Xavier Helluy spent a lot of time discussing with me about MR topics. I am grateful for that.

My special thanks to Prof. Axel Haase and to Prof. Hans Fraas. They made it easy for me to gain ground and start my career in a foreign land. And greetings to every member of the Department of Experimental Physics 5 in Würzburg for the great atmosphere at work.

Finally, I want to thank my wife, Kinga, for that unscientific part of my life, which affords me to enjoy the scientific part.

EHRENWÖRTLICHE ERKLÄRUNG

gemäß §5 Abs. 2 Ziff. 2 und 5
der Promotionsordnung der
Fakultät für Physik und Astronomie der
Universität Würzburg

Hiermit erkläre ich ehrenwörtlich, dass ich die Dissertation selbstständig und ohne Hilfe eines Promotionsberaters angefertigt und keine anderen als die angegebenen Quellen und Hilfsmittel benutzt habe.

Die Dissertation wurde bisher weder vollständig noch teilweise einer anderen Hochschule mit dem Ziel einen akademischen Grad zu erwerben vorgelegt.

Würzburg, 2. November 2009

(David Balla)